

UC Riverside

UC Riverside Electronic Theses and Dissertations

Title

Characterizing and Communicating Earth Structure Through Seismology and Pedagogy

Permalink

<https://escholarship.org/uc/item/9151h4z2>

Author

Goldhagen, Gillian Blake

Publication Date

2022

Peer reviewed|Thesis/dissertation

UNIVERSITY OF CALIFORNIA
RIVERSIDE

Characterizing and Communicating Earth Structure Through Seismology and Pedagogy

A Dissertation submitted in partial satisfaction
of the requirements for the degree of

Doctor of Philosophy

in

Earth and Planetary Sciences

by

Gillian Blake Goldhagen

December 2022

Dissertation Committee:

Dr. Heather A. Ford Chairperson

Dr. Kinnari Atit

Dr. Maryjo Brounce

Copyright by
Gillian Blake Goldhagen
2022

The Dissertation of Gillian Blake Goldhagen is approved:

Committee Chairperson

University of California, Riverside

ABSTRACT OF THE DISSERTATION

Characterizing and Communicating Earth Structure Through Seismology and Pedagogy

by

Gillian Blake Goldhagen

Doctor of Philosophy, Graduate Program in Earth and Planetary Sciences
University of California, Riverside, December 2022
Dr. Heather A. Ford, Chairperson

Chapter 1 is a seismic study of the mantle structure of the passive margin of northeastern North America. This region experienced multiple episodes of rifting and orogenesis in the past, and the study aims to understand how the Wilson Cycle impacts the geometry of the upper mantle seismic structure beneath southern New England using S_p receiver functions. Our findings indicate that structures related to the formation and breakup of Pangea may still be preserved at depth despite more recent magmatic and tectonic influences. Chapter 2 presents an analysis of P-wave attenuation for East Africa, focusing on the Afar, the Eastern Branch, and the Western Branch regions to analyze the extent to which volatiles may explain the presence of the regions' slow seismic velocities. Our modeled results indicate that a low Q_p melt layer, similar to those observed beneath mid-ocean ridges, is sufficient to reconcile previous geochemical and geophysical results. Chapter 3 describes a quasi-experimental education study that tests the relationship between pedagogical methods and students' spatial skills in an introductory earth science general education course. In our study, we found no difference in the efficacy of the teaching methods or environments tested. We did observe a difference in male and female performance in domain-general spatial skills, with females scoring lower, suggesting that a focus on improving disparities between genders be considered in courses where spatial learning is required.

Table of Contents

Introduction	1
References	10
Chapter 1	
Abstract	15
Introduction	16
Data and Methods	17
Results	18
Discussion	19
Acknowledgments	24
Figures	25
References	29
Chapter 2	
Abstract	33
Introduction	35
Data and Methods	38
Results	42
Discussion	44
Conclusion	53
Figures	55
References	63

Chapter 3	
Abstract	70
Overview & Objectives	71
Background	73
Method	83
Procedure	85
Instructional Materials	86
Results	89
Discussion	92
Conclusion	97
Figures and Tables	98
References	109
Conclusion	119
Appendix A	120
Figures and Tables	126
References	135
Appendix B	137

List of Figures

Chapter 1

Figure 1.1: Tectonics of South New England	25
Figure 1.2: Cross-sections through Sp CCP stacked RFs	26
Figure 1.3: Maps of selected negative phase	27
Figure 1.4: Cross-sections of RF picks	28

Chapter 2

Figure 2.1: Labeled topographic map of East Africa	55
Figure 2.2: Waveform matching results for single event	56
Figure 2.3: Probability density functions of East Africa	57
Figure 2.4: Probability density functions of central East Africa	58
Figure 2.5: Δt^* model of East Africa	59
Figure 2.6: Δt^* model of central East Africa	60
Figure 2.7: Q_p and dV_p models	61
Figure 2.8: Temperature anomaly models	62

Chapter 3

Figure 3.1: Study schedule	98
Figure 3.2: Example of Guay's Visualization of Views test	99
Figure 3.3: Topography demonstration examples	100
Figure 3.4: Volcano in-person model example	101
Figure 3.5: Fault type model example	102

Figure 3.6: Pre and Post visualization averages per treatment	103
---	-----

Appendix A

Figure A.1: Original Cross-sections with sampling density and std	130
---	-----

Figure A.2: Map of sampling density	131
-------------------------------------	-----

Figure A.3: Map of individual points withing RF model	132
---	-----

Figure A.4: Histograms of data	133
--------------------------------	-----

Figure A.5: Plot of negative phase picks grouped by terrane	134
---	-----

List of Tables

Chapter 3

Table 3.1: Descriptive of Data	104
Table 3.2: Correlation Table	105
Table 3.3: Linear regression models between variables, pre and post-test scores	106
Table 3.4: Linear regression models between variables, midterm scores	107
Table 3.5: Gender T-tests	108

Appendix A

Table A.1: Station Data	126
-------------------------	-----

INTRODUCTION

My research within this dissertation examines rifted margins, both young and old, through distinct seismic imaging methods and the relationship between students' spatial skills and how we communicate our science in the classroom. Each chapter is unique from the chapter before it and follows my evolving research interests throughout my Ph.D. First, we start at an older rifted margin in Southern New England in order to study how past tectonics influenced the architecture of the tectonic plates we see today (Chapter 1). This project encompasses the work I started at the beginning of my Ph.D. program and allowed me to study seismic structures close to my native New York. Second, we improve our understanding of the rifting process beneath the East African Rift, focusing on bridging the gap between geophysical and petrological data through better constraints on attenuation (Chapter 2). This project focused on an area of active tectonics and represents the start of the Wilson Cycle, which serves as a link to the region previously studied in Chapter 1. Finally, through my teaching service, I realized that my students were not just struggling to learn geologic concepts; they couldn't accurately conceptualize the concepts in three dimensions. This inspired me to add elements of education to my work, to test ways to facilitate students' spatial skills in the beginner-level geoscience classroom (Chapter 3). Overall, my work within this dissertation may seem disconnected, but all follow the thread of my intellectual journey. To introduce these topics, we will start by covering background and key concepts.

The lithosphere and asthenosphere

Earth's interior is composed of layers, defined according to variations in their chemical and/or mechanical properties. The outermost solid layer is composed of tectonic plates, which continually move relative to one another, being pulled apart, pushed together, or “scraping” past each other as they shift on top of a convecting layer called the asthenosphere. The tectonic plates comprise the lithosphere, which encompasses the chemically distinctive crust and the uppermost mantle. The lithosphere is commonly described as a relatively dry, rigid layer that sits on top of the asthenosphere (e.g., Sleep, 2005; Anderson & Sammis, 1970; Fischer et al., 2010). From seismic tomography methods, the lithosphere is observed to be a 50-200 km thick layer of high seismic wave speeds. In contrast, the underlying asthenosphere is observed to be seismically slow (e.g., Schaeffer & Lebedev, 2013, Fischer et al., 2010). The region where the lithosphere transitions to the asthenosphere is referred to as the lithosphere-asthenosphere boundary (LAB), or occasionally the lithosphere-asthenosphere transition (LAT) (i.e., Yoshizawa & Kennett 2015).

The difference in mechanical properties between the lithosphere and asthenosphere is principally due to an increase in temperature (e.g., Faul & Jackson 2005; Priestley & McKenzie, 2006; Stixrude & Lithgow-Bertelloni 2005). However, the presence of melt and/or water may also play a role (Fischer et al., 2010; Hirth et al., 2000; Lee et al., 2005; Sleep, 2005). Seismic velocity changes result from associated changes in temperature, pressure, composition, melt, and/or hydration. When these physical properties decrease

rigidity, velocity also decreases. Changes in seismic wave speed alone cannot discriminate between these many factors; however, seismic attenuation can provide additional constraints. Seismic attenuation is a result of elastic and intrinsic properties which are affected by temperature, grain size (Faul & Jackson, 2005), melt (Abers et al., 2014), and potentially mantle fO_2 (Cline et al., 2018) or water (Karato, 2003). Changes in velocity and attenuation can be characterized using a host of seismic imaging methods. Chapter 1 uses S_p receiver function analysis to image a change in wave speed associated with the LAB. Chapter 2 uses a P-wave time domain attenuation analysis to image variations in attenuation.

Evolution of rifted margins

For this dissertation, I focus on imaging the seismic structure beneath two separate rifted margins- one mature and one nascent, in order to better understand the tectonic evolution of rifted environments. Rifted margins form when the lithosphere is thinned and pulled apart, a process included in the Wilson Cycle. After rifting is established, an ocean basin can form, and new lithosphere is created within the space between the plates as they move apart. In some regions, such as in eastern North America, geologic evidence exists to support multiple rifting episodes along the margin. In east Africa, a new rift is slowly pulling apart the African continent. There, the key question is why the strong and rigid lithosphere is able to thin, weaken and rift. In Chapter 1, I explore the seismic architecture of the eastern North American margin as it relates to the evolution of the plate boundary in order to understand the effects of multiple Wilson Cycles on the

structure of the lithosphere. I focus on southern New England, where the deployment of a dense seismic array allows for careful examination of changes across distinct terrane boundaries. In Chapter 2, I utilize attenuation analysis to model mantle conditions beneath the newly forming East African Rift in order to ascertain whether the presence of volatiles is necessary to explain the anomalously slow velocities in the region. This, in turn, will be used to explore the mantle conditions needed to promote new rifts in continental regions.

East African Rift

The continent of Africa was primarily assembled by the mid-to-late Proterozoic. Presently, the oldest continental lithosphere in our study area is the Tanzanian and Kaapvaal cratons. The present-day region of rifting in east Africa is most commonly referred to as the East African Rift (EAR), which was initiated during the late Paleogene. Rifting motion within the EAR is partitioned into three sections, the Main Ethiopian Rift, the Eastern Branch, and the youngest Western Branch. The Main Ethiopian Rift starts at the Afar triangle to the north and then terminates south at Lake Turkana. The Afar triangle is a low elevation triple junction between the African, Arabian, and Somalian plates and is the site of initial rifting within the East African Rift system. The Eastern Branch starts at the top of the Main Ethiopian Rift or, in some maps, can start at Lake Turkana and ends in the basin of the North-Tanzanian divergence farther south. The Western Branch originates north from lake Albert in a north-northeast direction which

turns northwest to southeast and eventually north to south, striking where it terminates at Lake Malawi.

The EAR's initiation appears to be a result of the Afar mantle plume impinging on the lithosphere ~ 30 Ma (Hofmann et al., 1997; Schilling et al., 1992). Plume activity took place west of the Afar triangle and migrated southward, potentially with the northward drift of Africa (Chorowicz, 2005). Rifting within EAR took place as open fractures in the Afar and Ethiopian Plateaus (Mège & Korme, 2004). This led to rifting in the Gulf of Aden from 29.9-28.7 Ma and the southern Red Sea from 27.5-23 Ma (Hughes et al., 1991). The Afar depression formed during the Miocene, and the first volcanic activity in the region took place 20 Mya. Cenozoic volcanoes are widespread in the north within the eastern branch and sparser in the south (Chorowicz, 2005); however, the date of the most recent eruption is still unknown for most of the volcanoes within the East African Rift (Biggs et al., 2021). The Main Ethiopian Rift, the present-day position of the Afar Plume (Bastow et al., 2008; Hansen et al., 2012), formed after 11 Ma (Wolfenden et al., 2004) and continues to propagate south along the eastern and western branches as well as mature seafloor spreading along the Gulf of Aden and the Red Sea. The rift itself is still forming, and the Afar triangle will eventually be mature enough to create ocean crust similar to what we see in the Red Sea and the Gulf of Aden today.

New England

The current geologic architecture of New England is the result of two complete Wilson Cycles. The first Wilson Cycle started approximately 1 billion years ago when Laurentia,

the core of North America, was stabilized after the accretion of the Grenville orogen during the assembly of Rodinia. The eventual breakup of Rodinia and the opening of the Iapetus Ocean around 530 Ma left behind the continent of Laurentia, with the Grenville orogen making up the northeastern coastline (Li et al., 2018; Musacchio et al., 1997; Thomas, 2006). The second Wilson Cycle involved the closing of the Iapetus Ocean in the formation, and eventual breakup, of Pangea. Pangea's breakup is associated with CAMP magmatism and is responsible for the formation of the Hartford basin in Connecticut and the eventual formation of the Atlantic Ocean.

Our study focuses on the geophysical characteristics of the Laurentian (Grenville) and Appalachian terranes. Some support exists for a geophysical transition between the Grenville orogen and the Appalachian province at depth (Li et al., 2003; Musacchio et al., 1997). Musacchio et al. (1997) used active source and seismic refraction data to find differences in crustal thickness between the Grenville and the Appalachian. The Grenville province has a crustal thickness of approximately 45 km and P-wave velocities of 6.3, 6.7, to 7 from the upper, middle, to lower crust. The Appalachian province had a crustal thickness from 36 km in the east to 40 km farther west with a lower P-wave velocity. These differences resulted from crustal processes that modified the Grenville lower crust during the mid-Proterozoic period. These crustal differences were confirmed by Li et al. (2018) using the TA array to study the structural variations that extended to the base of the Moho. The individual orogens that make up the Appalachian province may differ similarly at depth. Globally, lithospheric thickness is often related to age (Fisher et al., 2010), suggesting that each orogen initially had a different characteristic depth imageable

with receiver function analysis. However, some theories suggested that after the Pangea rifting, the orogens' original lithospheric segments may have been scraped off as the tectonic plates shifted to their current positions. New lithosphere would have formed over time as the eastern coast became a stable passive margin (Levin et al., 2000; Li et al., 2018; Menke et al., 2016). In this dissertation, I use comparable passive source technology to interrogate these rifting processes in East Africa and New England to illuminate how the structure of the upper mantle is affected at different stages of rifting.

Rifted margins in education

Intellectually, my first two chapters of this dissertation are trying to further understand the rifting process, which is one of the fundamental pieces of plate tectonics. To teach concepts such as tectonics in the classroom, courses often rely on static or two-dimensional imagery to showcase complex dynamic movement. For novices, three-dimensional visualization skills are needed to comprehend dynamic information represented in these static diagrams (Kastens et al., 2016; Ormand et al., 2014). However, creating more dynamic visualizations within the classroom may not be sufficient in facilitating student learning. If students have insufficient spatial skills, they may struggle to learn through more complex 3D visuals that try to improve upon static or 2D visuals (Huk, 2006). Studies have shown that certain demographics, most notably gender, may disproportionately struggle with completing spatial tasks involving 3D Visualization (Miller and Halpern, 2013). The geoscience discipline is traditionally one of the least diverse STEM fields in the United States (Stokes et al., 2015), and it is possible that

disparities in spatial skills have contributed to the lack of diversity in the classroom. A review of the research on spatial skills and STEM learning indicates that domain-general spatial skills, such as domain-general 3D visualization skills, are fundamental for introductory STEM learning and perhaps serve as a gatekeeper to pursuing STEM coursework (Uttal & Cohen, 2012). Despite the importance of 3D spatial skills to STEM and geoscience, it is rarely accounted for in the educational curriculum. In my final chapter, I look to improve geoscience pedagogy by furthering our understanding of individual students' spatial skills. Research has shown that teaching geology can increase students' spatial skills (Ormand et al., 2014); if we study specific pedagogy to best facilitate these skills, we can better communicate geospatial concepts like rifted margins within the classroom.

The importance of spatial skills in introductory science courses

Geoscience has educational attributes that set it apart from other STEM. In King's (2008) overview of geoscience education, it was found that geoscience was unique in its being '...an interpretive and historical science' (Frodeman, 1995, p. 960) involving a range of methodologies that require retrodictive thinking, large-scale thinking, and integrating large often incomplete data sets. King also stated that geoscience played a crucial role in developing students' holistic systems thinking and high-level spatial thinking. Geoscience study often leads to student exposure to history, knowledge of complex systems, conceptualizing phenomena through time and across space, visual representation, integration, and retrospective thinking (Orion & Ault 2007). Geoscience learning helps

develop a wide range of cognitive skills that, like other skills garnered from STEM, can lead to success within the workforce. A 2012 congressional research service report for congress stated that: “Today the economic and social benefits of scientific thinking and STEM education are widely believed to have broad application for workers in both STEM and non-STEM occupations. As such, many contemporary policymakers consider widespread STEM literacy and specific STEM expertise to be critical human capital competencies for a 21st-century economy (Gonzalez & Kuenzi, 2012, p 3-4). STEM can equip workers with beneficial transferable skills, and geoscience is an integral part of that due to the unique aspects of the field.

Not only is geoscience important on a cognitive level, but the subject matter also has important implications for students. For many, geoscience classes are students’ only exposure to natural hazard mitigation which can and has saved students' lives. In 2004 during the tsunami triggered in the Indian Ocean, a ten-year-old girl from the UK was vacationing with her family on Maikhao beach in Phuket, Thailand. She recognized the signs of a tsunami from her geology class earlier in the year and is credited with saving around 100 lives, including her family (Torres, 2005, p. 7-12). Students living in areas like California are surrounded by the risk of natural hazards almost all year long with earthquakes, floods, mudslides, wildfires, and beach erosion. Geoscience classes can help keep students not only informed that they are near such hazards but can also learn about how to keep themselves safe from hazards.

REFERENCES

- Abers, G. A., Fischer, K. M., Hirth, G., Wiens, D. A., Plank, T., Holtzman, B. K., ... & Gazel, E. (2014). Reconciling mantle attenuation-temperature relationships from seismology, petrology, and laboratory measurements. *Geochemistry, Geophysics, Geosystems*, 15(9), 3521-3542.
- Anderson, D. L., & Sammis, C. (1970). Partial melting in the upper mantle. *Physics of the Earth and Planetary Interiors*, 3, 41-50.
- Bastow, I. D., Nyblade, A. A., Stuart, G. W., Rooney, T. O., & Benoit, M. H. (2008). Upper mantle seismic structure beneath the Ethiopian hot spot: Rifting at the edge of the African low-velocity anomaly. *Geochemistry, Geophysics, Geosystems*, 9(12).
- Chorowicz, J. (2005). The East African rift system. *Journal of African Earth Sciences*, 43(1-3), 379-410.
- Cline Ii, C. J., Faul, U. H., David, E. C., Berry, A. J., & Jackson, I. (2018). Redox-influenced seismic properties of upper-mantle olivine. *Nature*, 555(7696), 355-358.
- Dorais, M. J., Wintsch, R. P., Kunk, M. J., Aleinikoff, J., Burton, W., Underdown, C., & Kerwin, C. M. (2012). PTt conditions, Nd and Pb isotopic compositions and detrital zircon geochronology of the Massabesic Gneiss Complex, New Hampshire: Isotopic and metamorphic evidence for the identification of Gander basement, central New England. *American Journal of Science*, 312(10), 1049-1097.
- Faul, U. H., & Jackson, I. (2005). The seismological signature of temperature and grain size variations in the upper mantle. *Earth and Planetary Science Letters*, 234(1-2), 119-134.
- Fischer, K. M., Ford, H. A., Abt, D. L., & Rychert, C. A. (2010). The lithosphere-asthenosphere boundary. *Annual Review of Earth and Planetary Sciences*, 38, 551-575.
- Frodeman, R. (1995). Geological reasoning: Geology as an interpretive and historical science. *Geological Society of America Bulletin*, 107(8), 960-968.
- George, R., Rogers, N., & Kelley, S. (1998). Earliest magmatism in Ethiopia: evidence for two mantle plumes in one flood basalt province. *Geology*, 26(10), 923-926.

- Gonzalez, H. B., & Kuenzi, J. J. (2012, August). Science, technology, engineering, and mathematics (STEM) education: A primer. Washington, DC: Congressional Research Service, Library of Congress.
- Hansen, S. E., Nyblade, A. A., & Benoit, M. H. (2012). Mantle structure beneath Africa and Arabia from adaptively parameterized P-wave tomography: Implications for the origin of Cenozoic Afro-Arabian tectonism. *Earth and Planetary Science Letters*, 319, 23-34.
- Hibbard, J. P., Van Staal, C. R., Rankin, D. W., & Williams, H. (2006). Lithotectonic map of the Appalachian orogen, Canada–United States of America. Geological Survey of Canada, Map A, 2096(2).
- Hirth, G., Evans, R. L., & Chave, A. D. (2000). Comparison of continental and oceanic mantle electrical conductivity: Is the Archean lithosphere dry?. *Geochemistry, Geophysics, Geosystems*, 1(12).
- Hofmann, C., Courtillot, V., Feraud, G., Rochette, P., Yirgu, G., Ketefo, E., & Pik, R. (1997). Timing of the Ethiopian flood basalt event and implications for plume birth and global change. *Nature*, 389(6653), 838-841.
- Hughes, G. W., Varol, O., & Beydoun, Z. R. (1991). Evidence for Middle Oligocene rifting of the Gulf of Aden and for Late Oligocene rifting of the southern Red Sea. *Marine and petroleum Geology*, 8(3), 354-358.
- Huk, T. (2006). Who benefits from learning with 3D models? The case of spatial ability. *Journal of computer assisted learning*, 22(6), 392-404.
- Karato, S. I., & Eiler, J. (2003). Mapping water content in upper mantle. *Geophysical Monograph-American Geophysical Union*, 138, 135-152.
- Kastens, K. A., Shipley, T. F., Boone, A. P., & Straccia, F. (2016). What Geoscience Experts and Novices Look At, and What They See, When Viewing Data Visualizations. *Journal of Astronomy & Earth Sciences Education*, 3(1), 27-58.
- King, C. (2008). Geoscience education: an overview. *Studies in Science Education*, 44(2), 187-222.
- Lee, C. T. A. (2005). Trace element evidence for hydrous metasomatism at the base of the North American lithosphere and possible association with Laramide low-angle subduction. *The Journal of Geology*, 113(6), 673-685
- Levin, V., Park, J., Brandon, M. T., & Menke, W. (2000). Thinning of the upper mantle during late Paleozoic Appalachian orogenesis. *Geology*, 28(3), 239-242.

- Li, A., Forsyth, D. W., & Fischer, K. M. (2003). Shear velocity structure and azimuthal anisotropy beneath eastern North America from Rayleigh wave inversion. *Journal of Geophysical Research: Solid Earth*, 108(B8).
- Li, C., Gao, H., Williams, M. L., & Levin, V. (2018). Crustal thickness variation in the northern Appalachian Mountains: Implications for the geometry of 3-D tectonic boundaries within the crust. *Geophysical Research Letters*, 45(12), 6061-6070.
- Mège, D., & Korme, T. (2004). Dyke swarm emplacement in the Ethiopian Large Igneous Province: not only a matter of stress. *Journal of Volcanology and Geothermal Research*, 132(4), 283-310.
- Menke, W., Skryzalin, P., Levin, V., Harper, T., Darbyshire, F., & Dong, T. (2016). The Northern Appalachian anomaly: A modern asthenospheric upwelling. *Geophysical Research Letters*, 43(19), 10-173.
- Miller, D. I., & Halpern, D. F. (2013). Can spatial training improve long-term outcomes for gifted STEM undergraduates?. *Learning and individual differences*, 26, 141-152.
- Musacchio, G., Mooney, W. D., Luetgert, J. H., & Christensen, N. I. (1997). Composition of the crust in the Grenville and Appalachian Provinces of North America inferred from Vp/Vs ratios. *Journal of Geophysical Research: Solid Earth*, 102(B7), 15225-15241.
- Orion, N., & Ault, C. R. (2007). Learning earth sciences. In S. A. Abell & N. G. Lederman (Eds.), *Handbook of research on science teaching and learning* (pp. 653–687). Mahwah, NJ: Lawrence Erlbaum.
- Ormand, C. J., Manduca, C., Shipley, T. F., Tikoff, B., Harwood, C. L., Atit, K., & Boone, A. P. (2014). Evaluating geoscience students' spatial thinking skills in a multi-institutional classroom study. *Journal of Geoscience Education*, 62(1), 146-154.
- Priestley, K., & McKenzie, D. (2006). The thermal structure of the lithosphere from shear wave velocities. *Earth and Planetary Science Letters*, 244(1-2), 285-301.
- Schaeffer, A. J., & Lebedev, S. (2013). Global shear speed structure of the upper mantle and transition zone. *Geophysical Journal International*, 194(1), 417-449.
- Schilling, J. G., Kingsley, R. H., Hanan, B. B., & McCully, B. L. (1992). Nd-Sr-Pb isotopic variations along the Gulf of Aden: Evidence for Afar mantle plume-continental lithosphere interaction. *Journal of Geophysical Research: Solid Earth*, 97(B7), 10927-10966.

- Sleep, N. H. (2005). Evolution of the continental lithosphere. *Annual Review of Earth and Planetary Sciences*, 33(1), 369-393.
- Stixrude, L., & Lithgow-Bertelloni, C. (2005). Mineralogy and elasticity of the oceanic upper mantle: Origin of the low-velocity zone. *Journal of Geophysical Research: Solid Earth*, 110(B3).
- Stokes, P. J., Levine, R., & Flessa, K. W. (2015). Choosing the geoscience major: Important factors, race/ethnicity, and gender. *Journal of Geoscience Education*, 63(3), 250-263.
- Taylor, S. R., & TOKSÖZ, M. N. (1982). Crust and upper-mantle velocity structure in the Appalachian orogenic belt: Implications for tectonic evolution. *Geological Society of America Bulletin*, 93(4), 315-329.
- Torres, J. A. (2005). *Disaster in the Indian Ocean: Tsunami 2004*. Mitchell Lane Publishers, Inc..
- Thomas, W. A. (2006). Tectonic inheritance at a continental margin. *GSA today*, 16(2), 4-11.
- Uttal, D. H., & Cohen, C. A. (2012). Spatial thinking and STEM education: When, why, and how?. In *Psychology of learning and motivation* (Vol. 57, pp. 147-181). Academic Press.
- Wintsch, R. P., Yi, K., & Dorais, M. J. (2014). Crustal thickening by tectonic wedging of the Ganderian rocks, southern New England, USA: evidence from cataclastic zircon microstructures and U–Pb ages. *Journal of Structural Geology*, 69, 428-448.
- Wolfenden, E., Ebinger, C., Yirgu, G., Deino, A., & Ayalew, D. (2004). Evolution of the northern Main Ethiopian rift: birth of a triple junction. *Earth and Planetary Science Letters*, 224(1-2), 213-228.
- Yoshizawa, K., & Kennett, B. L. N. (2015). The lithosphere-asthenosphere transition and radial anisotropy beneath the Australian continent. *Geophysical research letters*, 42(10), 3839-3846.

**Evidence for a lithospheric step and pervasive lithospheric thinning
beneath southern New England**

Gillian Goldhagen^{1,*}, Heather A. Ford¹ and Maureen D. Long²

¹Dept. of Earth and Planetary Sciences, University of California – Riverside, Riverside,
CA, USA.

²Dept. of Earth and Planetary Sciences, Yale University, New Haven, CT, USA.

*corresponding author

ABSTRACT

In this study we use data from the SEISConn seismic experiment to calculate Sp receiver functions in order to characterize the geometry of upper mantle structure beneath southern New England. We image robust negative velocity gradient discontinuities beneath southern New England that we interpret as corresponding to the lithosphere-asthenosphere boundary (LAB) and identify a well-defined step of 15 km in LAB depth at a longitude of 73°W, which we interpret to be the boundary between Laurentian and Appalachian lithosphere, although the offset may be larger if the putative LAB phase is reinterpreted to be a mid-lithospheric discontinuity. We infer that the lithosphere throughout the region is substantially thinner than elsewhere in the continental interior, but consistent with regional tomographic studies and previously published Sp receiver function results. The presence of thinned lithosphere suggests that the low velocity Northern Appalachian Anomaly (NAA) in the upper mantle may extend as far south as coastal Connecticut. The presence of regionally thinned lithosphere and a step in lithospheric thickness suggests that inherited structure may be preserved in present day lithosphere, even in the presence of more recent dynamic processes associated with the presence of the NAA.

INTRODUCTION

Southern New England's geologic structure is the result of two Wilson cycles starting approximately one billion years ago (Hatcher 2010). The results of repeated rifting, accretion, and subduction on the (mantle) lithospheric structure of the continental margin are not well constrained. Global tomography finds some correlation between crustal age and inferred lithospheric thickness (e.g., Steinberger and Becker, 2018) although at shorter length scales this relationship can break down (Simons and Van der Hilst, 2002). Structural deviations from this relationship may result from relatively recent tectonic processes, although it is unclear how long perturbations to lithospheric mantle structure can persist after the last thermotectonic event (Porter et al., 2019). A key question, then, is to what extent (if any) the repeated episodes of accretion and rifting in the northeastern U.S. have been preserved in the lithospheric mantle?

Estimates of lithosphere-asthenosphere boundary (LAB) depth based on receiver function (RF) analysis range from 50 to 115 km beneath the northeastern U.S. (Hopper and Fischer, 2018), while estimates based on seismic tomography range from 50-85 km (Yang and Gao 2018) to 60-150 km (Porter et al., 2016). Tomographic studies have also imaged a region of low upper mantle velocities beneath the northeastern U.S., commonly referred to as the Northern Appalachian Anomaly (NAA). Due to the relatively sparse spacing of available seismic stations in eastern North America, it has proven difficult to observe definitive changes in mantle structure that can be directly linked to inherited structure associated with continental collision or rifting. The recently completed

SEISConn seismic experiment (Long and Aragon, 2020) was designed to image crust and mantle structure at a finer scale, cross-cutting key tectonic features and geologic terranes in southern New England. These terranes include the Proterozoic-aged Grenville orogen to the west and terranes that were accreted during the Appalachian Orogeny to the east, including the Ganderia and Avalonia terranes. In this paper we compare observations of mantle structure generated using Sp RF analysis to these tectonic boundaries in order to better understand to what extent present-day seismic structure is related to past plate boundary processes.

DATA AND METHODS

The SEISConn deployment consisted of an east-west linear array spanning northern Connecticut and crosscutting several passive margin terrane boundaries and the centrally located Hartford rift basin (Long and Aragon, 2020). We used seismic data from the SEISConn experiment and from 76 additional broadband stations (Figure 1.1). Our highest spatial density data is in Northern Connecticut, with good coverage extending into Massachusetts and New York (see Appendix A Figures A.1 and A.2). We calculated more than 2,000 individual Sp RFs (filtered to 2-100s) and stacked them according to their common conversion point (CCP; e.g., Lekic et al., 2011). RF traces were migrated using a 3D mantle velocity model (Schmandt and Lin 2014, Schmandt et al., 2015) and a global crustal model (Laske et al., 2013). RF uncertainties were calculated using a bootstrapping technique (Hopper and Fischer 2018). See the Appendix A for a description of the methodology.

RESULTS

Our results (Figure 1.2) reveal a clear positive velocity gradient, corresponding to the Moho, as well as multiple negative velocity gradients within the mantle. A laterally continuous negative phase is observed west of 73°W at depths of roughly 60-100 km. A similar, lower amplitude, negative phase is observed at depths of 50-70 km east of 73°W . We also observe large, discontinuous negative phases at depths of 150-200 km centered at $\sim 73\text{-}74^{\circ}\text{W}$. These negative phases are adjacent to large amplitude positive phases in a region of poor data coverage (see Appendix A for data density plot), suggesting issues related to limited data. Secondary, laterally discontinuous negative phases are also present at mantle depths, and may reflect the presence of real structure, however we choose to focus our discussion on the largest amplitude phases. We mark only the largest negative phase at < 150 km depth (Hopper and Fischer, 2018), with the caveat that the phase must exceed error bars defined by 2 standard deviations and have a resolvable positive phase (Moho) between 25 and 50 km. Multiple negative phases with similar amplitudes are occasionally observed in a zone of negative energy (e.g., 60 to 90 km depth at -74 to -73°W). Our later discussion is largely unaffected by the decision to only pick the largest amplitude phase in these cases.

We observe a change in the amplitude and depth of the selected negative phases occurring at a longitude of approximately 73°W (Figure 1.3). Along northern profiles (Figure 1.2) the negative phase is observed at 70-80 km depth west of 73°W , gradually transitioning to shallower depths (60-70 km) east of 73°W . At C-C' (Figure 1.2) the

negative phase depth increases beneath the western half of the study area, reaching a maximum depth of 90-100 km and average depths of approximately 75-85 km, and abruptly transitions to a weaker, shallower (55-60 km) negative phase east of 73°W. 73°W is roughly coincident with the boundary between the Taconic belt and Ganderia terrane, which corresponds to the eastern boundary of Laurentia. At D-D' (Figure 1.2), the stepover at 73°W remains pronounced, although the step begins to diverge from the surface terrane boundary in southern Connecticut (Figure 1.3). In order to better assess whether this correlation is meaningful, we employed kmeans clustering, based only on amplitude and depth, and compare the clusters to results divided on the basis of the Laurentian boundary. We observe that the kmeans clustering generates groupings similar to those dictated by terrane, indicating that a relationship between depth, amplitude and terrane boundary may exist (see Appendix A). Averaging depth values east and west of the Taconic belt-Ganderia terrane yields an average depth offset across the terrane boundary of roughly 15 km.

DISCUSSION

While the depth and amplitude of the prominent negative phase can be clearly identified in our CCP images, its origin is less evident. We considered whether contrasts in seismic anisotropy within the upper mantle may contribute to our observations. However, given the complex nature of lithospheric anisotropy beneath our study region (e.g., Li et al., 2021; Lopes et al., 2020), it is likely that the negative phases we image reflect largely isotropic velocity decreases with depth. Numerous studies of continental lithosphere

have found evidence for mid-lithospheric discontinuities (MLDS) (e.g., Fischer et al., 2010; Wirth and Long, 2014; Abt et al., 2010) at depths of ~80-150 km. We compare our negative phases to the regional S-wave velocity model of Yang and Gao (2018) and find that our negative phases predominantly fall within the depth range suggested by a tomographically inferred potential LAB depth range, which we define as the depth of the first maximum in velocity downwards to the first minimum in velocity (Birkey et al., 2021) (Figure 1.4) (see Appendix A). Our results are also consistent with observations of lithospheric thinning (78 to 67 km) from west (75°W) to east (71°W) using USArray data (Hopper and Fischer, 2018), but we infer slightly thinner lithosphere than studies using Ps receiver functions (Rychert et al., 2005) and heat flow data (Artemieva, 2006). If the negative phase does in fact correspond to the LAB, this suggests that LAB depths in our study area are comparable to those of the tectonically active western U.S. and that an abrupt change in LAB properties is closely aligned with the eastern edge of pre-Appalachian Laurentia, over much of the study area, with the exception of southern Connecticut.

Lithospheric thickness estimates typically show a pronounced contrast between the western and eastern U.S., which may be attributed to differences in thermotectonic age (e.g., Porter et al., 2019). Regional tomography models show clear evidence for an upper mantle low velocity anomaly (the NAA) located beneath central New England, with depth extent estimated at 60-140 km (Li et al., 2003) to 60–300 km (Schmandt and Lin, 2014). These values overlap with the depth of our inferred LAB, providing independent evidence that the lithosphere may be thinned throughout southern New England. Our

inference is also consistent with recent evidence from shear wave splitting suggesting that the NAA may extend south to the latitude of the SEISConn array (Levin et al., 2018; Lopes et al., 2020), at least in eastern New England. The origin of the NAA is debated; it has been attributed to the Great Meteor hotspot (Eaton and Frederiksen, 2007) or to edge driven, small-scale convection (Menke et al., 2016). In any case, our results and others (Lopes et al., 2020; Luo et al., 2021) suggest that the NAA may be associated with lithospheric thinning as far south as southern New England.

While the regionally shallow LAB suggests a relationship to ongoing dynamic mantle processes, the change in depth and amplitude (a function of velocity gradient across the LAB) across the western edge of the accreted Appalachian terranes suggests that some lithospheric properties may be tectonically inherited. In the Ps RF imaging by Luo et al. (2021), a similar abrupt change in negative phase energy at mantle depths across the western edge of Laurentia was observed; however, the negative phase west of 73°W was interpreted to be an MLD, not the LAB. This alternative interpretation is possible, as the presence of MLDs in the Grenville province is well documented (Wirth and Long, 2014; Abt et al., 2010). If true, then the lithospheric step would be even more pronounced than the roughly 15 km vertical offset we propose here. If a lithospheric thickness of 100-150 km for Grenville-aged lithosphere (Porter and Reid, 2021) is assumed, this would imply an inferred LAB step of ~35-85 km. We also cannot exclude the possibility that the negative phase east of 73°W may represent an MLD. Regardless of whether the phase is MLD or LAB, we are left with the same observation, which is that the properties of the mantle lithosphere change at the boundary between Laurentia and the accreted

Appalachian terranes to the east. Li et al. (2018) and Luo et al. (2021) also documented a sharp “step” in crustal thickness across the same boundary beneath the SEISConn line; this is also broadly consistent with heat flow data which indicates that western Connecticut is cooler than central and eastern Connecticut (Artemieva, 2006). Taken together, the co-located changes in crustal and mantle lithospheric structure has important implications for isostatic compensation and density structure that will be explored quantitatively in future work.

Our observations provide evidence that lithospheric structure can be inherited and maintained over long-time scales. Complementary observations from elsewhere in eastern North America provide a similar argument; Wagner et al. (2018) argued for a role for inherited structures, including cratonic edges and suture zones, beneath the southeastern U.S. based on seismic tomography. Our inference of lithospheric thinning beneath eastern New England associated with the NAA also provides a basis for comparison with other structures in eastern North America, notably the Central Appalachian Anomaly (CAA), a region with thin lithosphere and slow upper mantle velocities (e.g., Evans et al., 2019; Byrnes et al., 2019). While it is plausible that a different set of processes has operated beneath the CAA and NAA to produce thinned lithosphere, detailed comparisons between the regions are instructive (e.g., Long et al., 2021), particularly in light of our new constraints on lithospheric structure beneath New England.

One potential explanation for the presence of both the vertical step and thinner-than-predicted lithosphere is that the processes associated with the NAA may have thermally eroded the base of the lithosphere beneath terranes east and west of the Grenville front. If so, fundamental differences in the rheology between Grenville-aged lithosphere and the Appalachian accreted terranes may have resulted in lateral contrasts in LAB depth and velocity gradient. Subduction and the introduction of water are one proposed mechanism to weaken cratonic lithosphere (e.g., Bedle et al., 2021). A potential consequence of the addition of water could be a reduction in wave speeds in the lithosphere, and a corresponding reduction in velocity gradient between the lithosphere and asthenosphere, resulting in diminished LAB amplitudes in receiver functions; we speculate that this mechanism may explain some of the amplitude observations in our study, although debate exists over the extent to which water affects wave speeds (e.g., Cline et al., 2018). Several westward dipping structures have been observed in the uppermost mantle beneath the eastern half of the SEISConn array using high-frequency Ps RF analysis; these structures generally terminate along the Grenville front (Luo et al., 2021). These structures have been interpreted as either relic slabs or shear zones associated with past subduction, suggesting the possibility that the step in lithospheric thickness that we observe results from the eastern half of southern New England being more significantly impacted by metasomatism, and thus more susceptible to later lithospheric loss associated with NAA-related asthenospheric upwelling. Importantly, this model is plausible regardless of whether the phase imaged west of the Laurentian boundary is the LAB or an

MLD, as in either case a stronger and thicker lithosphere likely exists west of the boundary.

ACKNOWLEDGEMENTS

The SEISConn project has been funded by Yale University and NSF via grants EAR-1150722 and EAR-1800923. We are grateful to all landowners and volunteers who made the SEISConn deployment possible. Data was obtained from the IRIS DMC. The facilities of the IRIS Consortium are supported by NSF Seismological Facilities for the Advancement of Geoscience (SAGE) Award, Cooperative Support Agreement EAR-1851048. We thank collaborators on the SEISConn project for useful discussions and several anonymous reviewers for comments that improved the paper.

The text of this dissertation, in full, is a reprint of the material as it appears in *Geology* on June 21st, 2022. The co-author, Heather A. Ford, listed in that publication, directed and supervised the research, which forms the basis for this dissertation. The co-author, Maureen D. Long, listed in that publication, provided the use of data and assisted in the publication, which forms the basis for this dissertation.

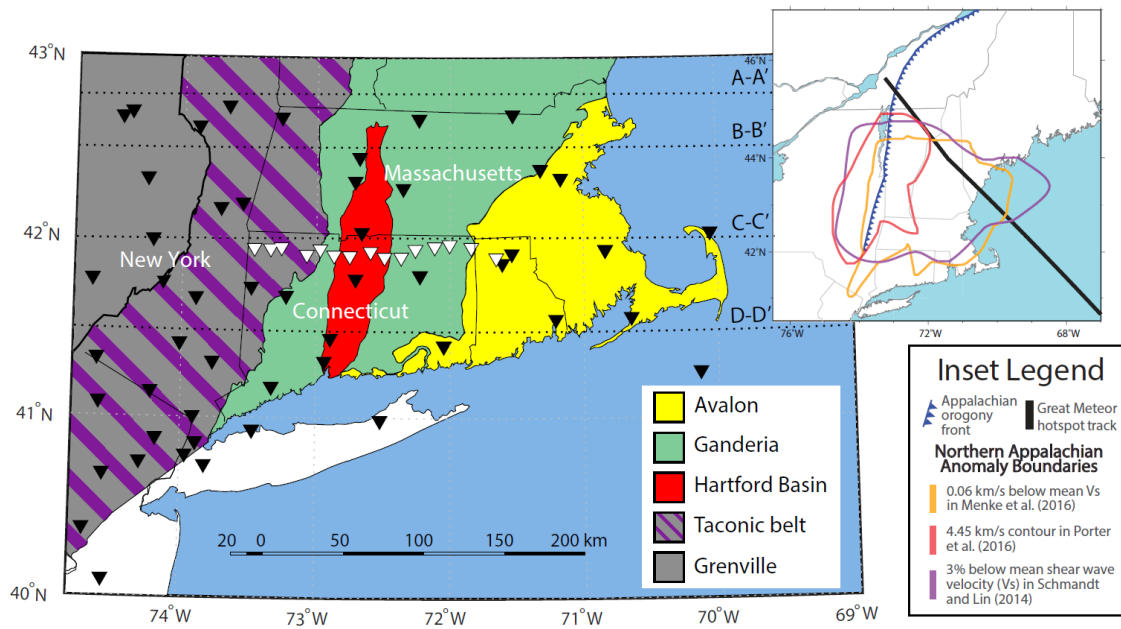


Figure 1.1 Tectonic setting of southern New England, after Hibbard et al. (2006), delineating major terranes (Grenville, Ganderia, and Avalon) as well as the Taconic belt, a zone of deformation during the Taconic Orogeny that makes up the western edge of Laurentia. We include the Moretown terrane, which accreted onto Laurentia during the Taconic orogeny, as part of Ganderia. White triangles correspond to SEISConn stations (network XP), black correspond to all other seismic stations (LD, N4, NE, TA, US, XA, XO) used. Dashed black lines correspond to cross sections in Figure 1.2. The inset (modified from Levin et al., 2017) outlines possible Northern Appalachian Anomaly boundaries based on seismic tomography models and the path of the Great Meteor Hot Spot.

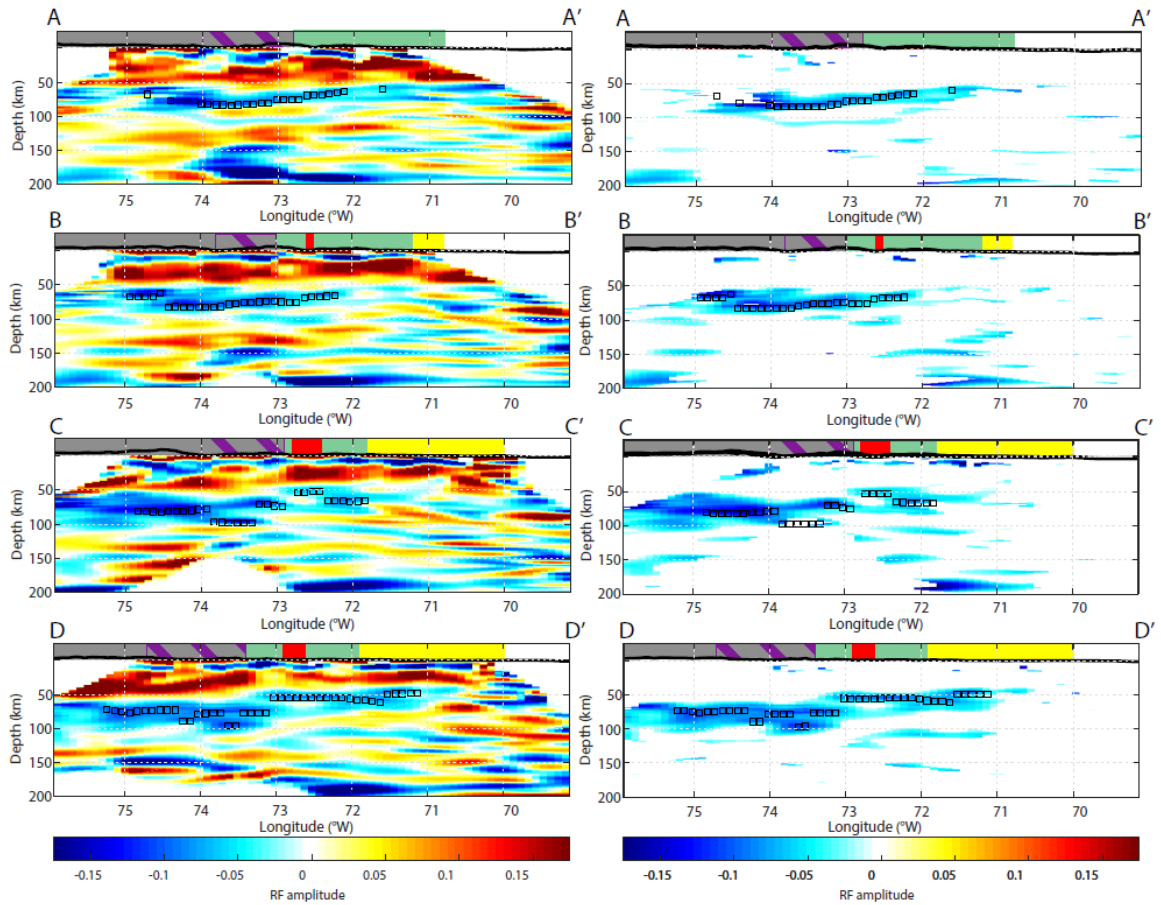


Figure 1.2 (left) Vertical cross sections through Sp CCP stacked RFs. Negative phases (blue) indicate the presence of a negative velocity gradient. Positive phases are shown in red. Open black squares show location of selected negative phases, likely corresponding to the LAB, picked using criteria discussed in the text. Colored boxes mark the extent of tectonic terranes (Figure 1.1). Note the pronounced change in depth of the LAB phase at $\sim 73^\circ\text{W}$ in cross sections C-C' and D-D'. (right) Masked Sp CCP stacked RF results where only negative amplitude phases with uncertainties of 0.08 or less are shown.

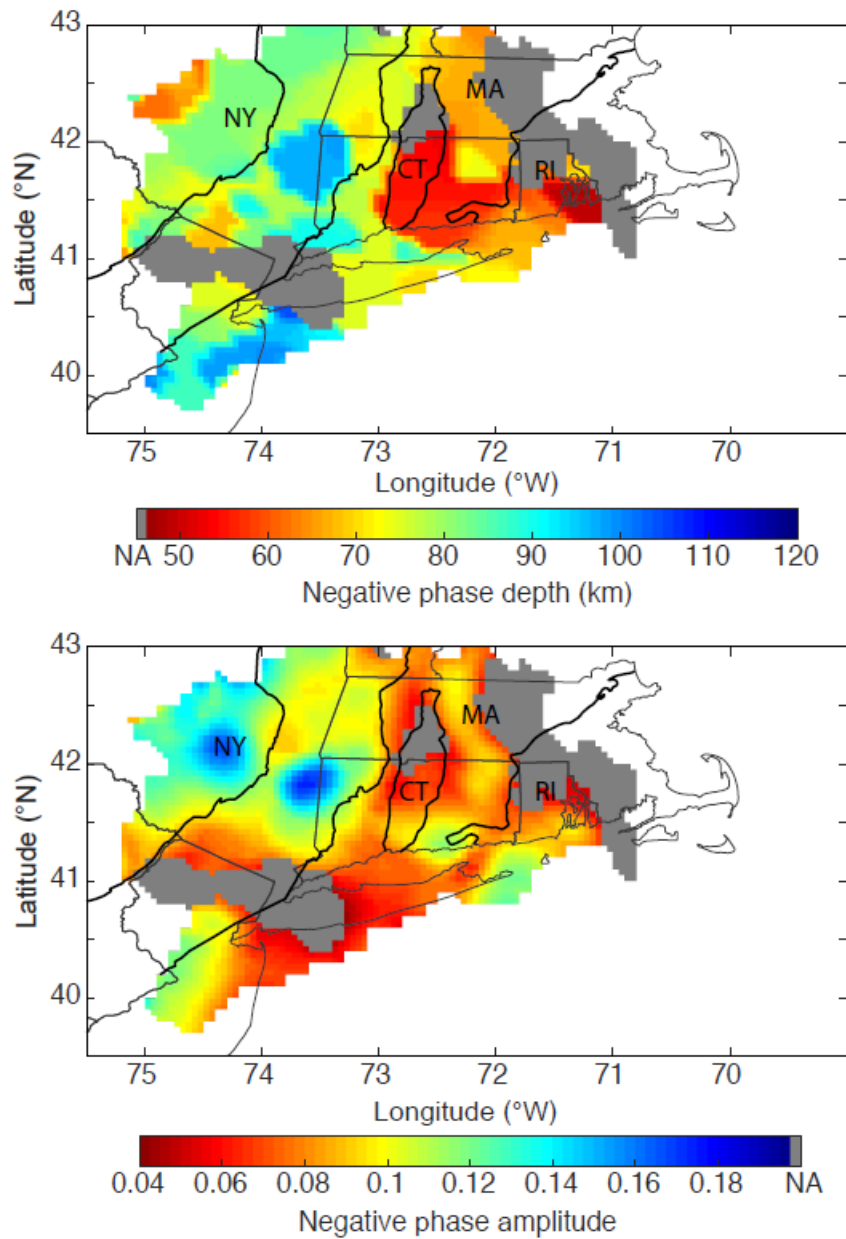


Figure 1.3 Maps of depth (top) and amplitude (bottom) of the selected negative phase interpreted as the LAB. Regions of the CCP image for which phases were not selected are marked in grey. Black lines mark the edges of terrane boundaries. A pronounced change in LAB depth (top) and amplitude (bottom) is approximately coincident with the Taconic belt-Ganderia terrane boundary.

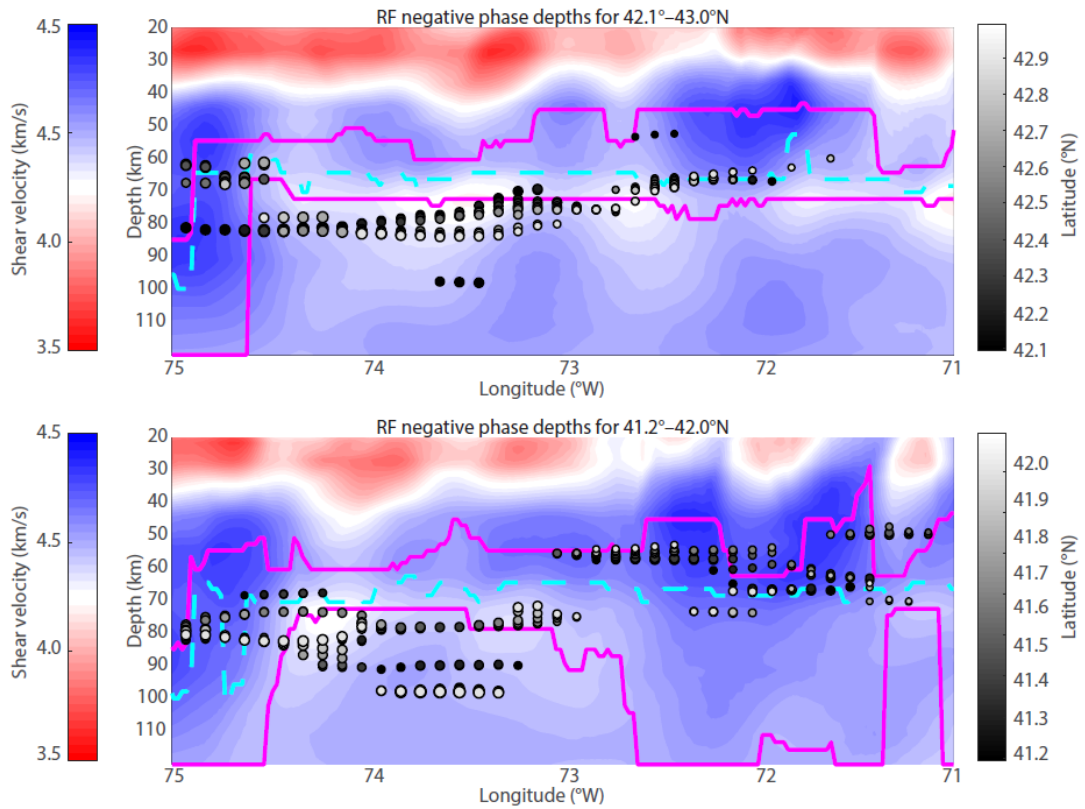


Figure 1.4 Cross sections of RF picks (solid circles with greyscale indicating latitude) from Figure 1.2 superimposed on averages of a Vs tomography model for the same latitudes (Yang and Gao, 2018) (IRIS EMC). At latitudes of 42.1-43°N (top), lateral changes in negative phase depth are more gradual, while from 41.2-42°N lateral changes in negative depth are more abrupt (bottom). The dashed cyan line (top and bottom) marks the depth of the maximum negative velocity gradient of the averaged tomography model, and solid magenta lines (top and bottom) mark the potential LAB depth range as defined in Birkey et al. (2021). In most regions, the selected phases fall within or below the potential LAB depth range.

REFERENCES

- Abt, D. L., Fischer, K. M., French, S. W., Ford, H. A., Yuan, H., & Romanowicz, B. (2010). North American lithospheric discontinuity structure imaged by Ps and Sp receiver functions. *Journal of Geophysical Research: Solid Earth*, *115*(B9).
- Artemieva, I. M. (2006). Global 1×1 thermal model TC1 for the continental lithosphere: implications for lithosphere secular evolution. *Tectonophysics*, *416*(1-4), 245-277.
- Bedle, H., Lou, X., & van der Lee, S. (2021). High-resolution imaging of continental tectonics in the mantle beneath the United States, through the combination of USArray data sets.
- Birkey, A., Ford, H. A., Dabney, P., & Goldhagen, G. (2021). The lithospheric architecture of Australia from seismic receiver functions. *Journal of Geophysical Research: Solid Earth*, *126*(4), e2020JB020999.
- Cline Ii, C. J., Faul, U. H., David, E. C., Berry, A. J., & Jackson, I. (2018). Redox-influenced seismic properties of upper-mantle olivine. *Nature*, *555*(7696), 355-358.
- Eaton, D. W., & Frederiksen, A. (2007). Seismic evidence for convection-driven motion of the North American plate. *Nature*, *446*(7134), 428-431.
- Evans, R. L., Benoit, M. H., Long, M. D., Elsenbeck, J., Ford, H. A., Zhu, J., & Garcia, X. (2019). Thin lithosphere beneath the central Appalachian Mountains: A combined seismic and magnetotelluric study. *Earth and Planetary Science Letters*, *519*, 308-316.
- Fischer, K. M., Ford, H. A., Abt, D. L., & Rychert, C. A. (2010). The lithosphere-asthenosphere boundary. *Annual Review of Earth and Planetary Sciences*, *38*, 551-575.
- Hatcher, R. D., Tollo, R. P., Bartholomew, M. J., Hibbard, J. P., & Karabinos, P. M. (2010). The Appalachian orogen: A brief summary. *From Rodinia to Pangea: The Lithotectonic Record of the Appalachian Region: Geological Society of America Memoir*, *206*, 1-19.
- Hibbard, J. P., Van Staal, C. R., Rankin, D. W., & Williams, H. (2006). Lithotectonic map of the Appalachian orogen, Canada–United States of America. *Geological Survey of Canada, Map A*, 2096(2).
- Hopper, E., & Fischer, K. M. (2018). The changing face of the lithosphere-asthenosphere boundary: Imaging continental scale patterns in upper mantle structure across the

contiguous US with Sp converted waves. *Geochemistry, Geophysics, Geosystems*, 19(8), 2593-2614.

IRIS DMC (2011), Data Services Products: EMC, A repository of Earth models, <https://doi.org/10.17611/DP/EMC.1>.

Laske, G., Masters, G., Ma, Z., & Pasyanos, M. (2013, April). Update on CRUST1. 0—A 1-degree global model of Earth's crust. In *Geophys. res. abstr* (Vol. 15, p. 2658).

Chen, Y., Randerson, J. T., Morton, D. C., DeFries, R. S., Collatz, G. J., Kasibhatla, P. S., ... & Marlier, M. E. (2011). Forecasting fire season severity in South America using sea surface temperature anomalies. *Science*, 334(6057), 787-791.

Levin, V., Long, M. D., Skryzalin, P., Li, Y., & López, I. (2018). Seismic evidence for a recently formed mantle upwelling beneath New England. *Geology*, 46(1), 87-90.

Li, C., Gao, H., Williams, M.L. & Levin, V., 2018, Crustal thickness variation in the northern Appalachian Mountains: Implications for the geometry of 3-D tectonic boundaries within the crust: *Geophysical Research Letters*, 45(12), p.6061-6070.

Li, Y., Levin, V., Nikulin, A., & Chen, X. (2021). Systematic Mapping of Upper Mantle Seismic Discontinuities Beneath Northeastern North America. *Geochemistry, Geophysics, Geosystems*, 22(7), e2021GC009710.

Long, M. D., & Aragon, J. C. (2020). Probing the structure of the crust and mantle lithosphere beneath the southern New England Appalachians via the SEISConn deployment. *Seismological Society of America*, 91(5), 2976-2986.

Long, M. D., Wagner, L. S., King, S. D., Evans, R. L., Mazza, S. E., Byrnes, J. S., ... & Liu, S. (2021). Evaluating models for lithospheric loss and intraplate volcanism beneath the Central Appalachian Mountains. *Journal of Geophysical Research: Solid Earth*, 126(10), e2021JB022571.

Lopes, E., Long, M. D., Karabinos, P., & Aragon, J. C. (2020). SKS splitting and upper mantle anisotropy beneath the southern New England Appalachians: Constraints from the dense SEISConn array. *Geochemistry, Geophysics, Geosystems*, 21(12), e2020GC009401.

Luo, Y., Long, M. D., Karabinos, P., Kuiper, Y. D., Rondenay, S., Aragon, J. C., ... & Makus, P. (2021). High-Resolution Ps Receiver Function Imaging of the Crust and Mantle Lithosphere Beneath Southern New England and Tectonic Implications. *Journal of Geophysical Research: Solid Earth*, 126(7), e2021JB022170.

- Menke, W., Skryzalin, P., Levin, V., Harper, T., Darbyshire, F., & Dong, T. (2016). The Northern Appalachian anomaly: A modern asthenospheric upwelling. *Geophysical Research Letters*, *43*(19), 10-173.
- Porter, R., & Reid, M. (2021). Mapping the Thermal Lithosphere and Melting across the Continental US. *Geophysical Research Letters*, *48*(7), e2020GL092197.
- Porter, R., Liu, Y., & Holt, W. E. (2016). Lithospheric records of orogeny within the continental US. *Geophysical Research Letters*, *43*(1), 144-153.
- Porter, R. C., van der Lee, S., & Whitmeyer, S. J. (2019). Synthesizing EarthScope data to constrain the thermal evolution of the continental US lithosphere. *Geosphere*, *15*(6), 1722-1737.
- Rychert, C. A., Fischer, K. M., & Rondenay, S. (2005). A sharp lithosphere–asthenosphere boundary imaged beneath eastern North America. *Nature*, *436*(7050), 542-545.
- Schmandt, B., & Lin, F. C. (2014). P and S wave tomography of the mantle beneath the United States. *Geophysical Research Letters*, *41*(18), 6342-6349.
- Schmandt, B., Lin, F. C., & Karlstrom, K. E. (2015). Distinct crustal isostasy trends east and west of the Rocky Mountain Front. *Geophysical Research Letters*, *42*(23), 10-290.
- Simons, F. J., Van Der Hilst, R. D., Montagner, J. P., & Zielhuis, A. (2002). Multimode Rayleigh wave inversion for heterogeneity and azimuthal anisotropy of the Australian upper mantle. *Geophysical Journal International*, *151*(3), 738-754.
- Steinberger, B., & Becker, T. W. (2018). A comparison of lithospheric thickness models. *Tectonophysics*, *746*, 325-338.
- Wagner, L. S., Fischer, K. M., Hawman, R., Hopper, E., & Howell, D. (2018). The relative roles of inheritance and long-term passive margin lithospheric evolution on the modern structure and tectonic activity in the southeastern United States. *Geosphere*, *14*(4), 1385-1410.
- Wirth, E. A., & Long, M. D. (2014). A contrast in anisotropy across mid-lithospheric discontinuities beneath the central United States—A relic of craton formation. *Geology*, *42*(10), 851-854.
- Yang, X., & Gao, H. (2018). Full-wave seismic tomography in the northeastern United States: New insights into the uplift mechanism of the Adirondack Mountains. *Geophysical Research Letters*, *45*(12), 5992-6000.

New measurements of seismic attenuation across the East African Rift

Gillian Goldhagen¹, Heather A. Ford^{1,*}, Joseph S. Byrnes², and Maryjo N. Brounce¹

¹Dept. of Earth and Planetary Sciences, University of California – Riverside, Riverside, CA, USA.

²School of Earth and Sustainability, Northern Arizona University, Flagstaff, AZ, USA.

*corresponding author

ABSTRACT

The East African Rift system formed because of rifting from extension potentially caused by the impingement of one or more mantle plumes on the lithosphere. The asthenosphere under the rift records slow seismic wave velocities, partly attributed to elevated mantle temperatures. However, petrologically constrained estimates of mantle temperatures at the depth of mantle melting suggest that mantle temperatures alone are not sufficiently high to account for the total decrease in seismic P-wave velocities in this region. We performed an attenuation analysis of teleseismic P-wave phases recorded at broadband stations throughout the region to constrain the physical mechanisms responsible for producing the observed slow wave speeds. This study incorporates data from 312 previously deployed stations and utilizes P-wave arrivals from 63 deep focus (>200 km depth) teleseismic events. Our results include a range of Δt^* values, from a maximum observed value of 0.19 s beneath the southwestern Afar region to a minimum value of -0.15 s beneath the Kaapvaal Craton. We compare the Eastern Branch, Western Branch, and Afar region to the Kaapvaal Craton, finding Δt^* differences relative to the Craton. The Eastern Branch has a Δt^* difference of 0.1889 ± 0.19 , the Western Branch a Δt^* difference of 0.2120 ± 0.02 , and Afar a Δt^* difference of 0.3311 ± 0.044 . We first test a two-layer comparative block model for the Eastern Branch, Western Branch, and the Afar region relative to the Kaapvaal Craton, assuming that high attenuation is uniformly spread out through an asthenospheric-like layer, to generate estimates of asthenospheric Q_P (inverse of attenuation), V_p , and T . The two-layer model calculated insufficient Q_P values to explain known melt. We additionally generated a three-layer comparative block

model for the Afar region using a similar model as previously proposed for mid-ocean ridges. We designed this model to represent a layer in which a low Q region is embedded within the asthenosphere., similar to previously proposed models for mid-ocean ridges. In this suite of models, we find that previously observed values of V_p can be explained by a petrologically determined thermal anomaly together with a low Q layer that is 40-110 km thick. These estimates agree well with previous constraints on rifting in the region and do not invoke the presence of unknown volatiles.

INTRODUCTION

The East African Rift (EAR) system is a region of intra-continental rifting and extension within the African continent, thought to be related to the one or more mantle plumes impinging on the overriding plate (e.g., Boyce et al., 2021; Civiero et al., 2016). The African continent was primarily assembled in the mid-to-late Proterozoic and comprised of several cratons, including the Kaapvaal, Zimbabwe, Tanzania, Congo, and West African Cratons. The rift initiated during the late Paleogene with the eruption of the African-Arabian continental flood basalt province, likely caused by the Afar plume impinging on the continental lithosphere at approximately 30 Ma (Hofmann et al., 1997; Schilling et al., 1992). The Main Ethiopian Rift marks the present-day position of the Afar plume (Bastow et al., 2008; Hansen et al., 2012). This rift formed after 11 Ma (Wolfenden et al., 2004) and extends south to the Eastern Branch and Western Branch (Figure 2.1), surrounding the Tanzanian Craton. The Eastern Branch begins at the southern terminus of the Main Ethiopian Rift in the north and terminates in the basin of the North-Tanzanian divergence in the south. The Eastern Branch and Western Branch intersect at the southern edge of the Tanzanian Craton between Lake Tanganyika and Lake Malawi, where the Eastern Branch ends, and the Western Branch intersects. The Western Branch originates at the northern boundary of Lake Albert to the north, wraps around the western edge of the Tanzanian Craton, and terminates at the southern banks of Lake Malawi.

Seismic tomography models (Adams et al., 2012; Boyce et al., 2021; Emry et al., 2019; O'Donnell et al., 2013; Weeraratne et al., 2003) along the EAR typically find thinner

lithosphere (5075 km) beneath the rifted structure near the lake regions of the Western Branch and the Eastern Branch, with thicker lithosphere (100-200 km) on either side of the rifts. The lithosphere beneath the Tanzanian Craton varies in thickness, with thicker lithosphere beneath the western half of the craton and thinner lithosphere to the east. Overall cratonic values range from 90-175 km, depending on the study (Adams et al., 2012; Boyce et al., 2021; Emry et al., 2019; O'Donnell et al., 2013; Weeraratne et al., 2003). Tomographic models show pronounced low seismic wave speeds in the mantle beneath the Main Ethiopian Rift (MER) (Bastow et al., 2008; Hansen et al., 2012), with the slowest wave speeds typically observed along the northwestern edge of the MER (Emry et al., 2019). Currently, there is a debate on the size, number, and scope of the plumes beneath East Africa (Boyce et al., 2021; Emry et al., 2019). Tomographic models reveal a low-velocity anomaly, the African Superplume, extending to the core-mantle boundary below South Africa (Hansen et al., 2012; Ritsema et al., 1999; Simmons et al., 2010, 2012). Several studies (Chang et al., 2015; Ritsema et al., 2011) argue for multiple narrower plumes in the upper mantle, possibly tapping into a heterogeneous lower mantle. Geochemistry potentially supports the argument for multiple plumes, where isotopic data on mafic lavas displayed evidence of being derived from two distinct regions of mantle upwelling (Nelson et al., 2012).

Slow seismic wave speeds are commonly attributed to elevated mantle temperatures (e.g., Faul & Jackson, 2005), but they can also be impacted by the presence of melt (Hammond & Humphreys, 2000; Kawakatsu et al., 2009; Takei, 2002; Takei & Holtzman, 2009), variations in mantle composition (Lee, 2003), grain size (Faul & Jackson, 2005), water

content (Aizawa et al., 2008; Rychert et al., 2007) and possibly mantle oxygen fugacity (fO_2) (Cline et al., 2018). Results summarized in Emry et al. (2019) indicate that beneath Afar, an average low shear wave speed among relevant models is 4.03 km/s, while the lowest documented shear velocity value is estimated as low as 3.7 km/s (Dugda et al., 2007; Emry et al., 2019); beneath the MER, the average low shear velocity among relevant models is 4.12 km/s, and the lowest documented shear velocity value is 3.8 km/s (Emry et al., 2019; Gallacher et al., 2016). Comparing these average low values to PREM (Dziewonski & Anderson, 1981), these averages correspond to a V_s decrease of roughly 9.5% beneath Afar and approximately 7.5% beneath the MER. Prior constraints from the MER lavas estimated the thermal anomaly associated with the plume to be approximately 140 °C, accounting for roughly ~2% decrease in δV_p (Ferguson et al., 2013; Rooney et al., 2012), assuming a quality factor of 80 (Venkataraman et al., 2014). Emry et al. (2019) calculated temperature as a function of seismic velocity perturbation and varying seismic attenuation, estimating 500-1000°C of excess temperature. The estimated temperature difference between geophysical and petrological results has been used to suggest the presence of volatile-rich partial melting beneath the East African Rift over a purely temperature-dependent model (Rooney et al., 2012).

To discriminate among the potential mechanisms responsible for reduced seismic wave speeds in the East African Rift, this study measures the attenuation of teleseismic P phases recorded at broadband stations in the vicinity of the rift zone. While uncertainty remains in both the measurement of attenuation due to processes including seismic wave scattering (Cafferky & Schmandt, 2015) and scaling of experimental measurements of Q_p

(the inverse of attenuation) to mantle conditions (Holtzman 2016), attenuation analysis may help in understanding the extent to which temperature alone can explain contrasts in velocity (e.g., Byrnes et al., 2020; Eilon & Abers, 2017; Takei, 2017; Yamauchi & Takei, 2016). Attenuation can also highlight to what extent we need to consider other mechanisms, such as grain size (Faul & Jackson 2005), melt (Abers et al., 2014; Byrnes et al., 2020; Eilon & Abers, 2017; Faul et al., 2004), water (Abers et al., 2014; Karato & Eiler, 2003), or mantle oxygen fugacity (Cline et al., 2018). Earlier attenuation work by Venkataraman et al. (2004) estimated the temperature beneath the East African Rift to be 140-280 K higher than surrounding mantle temperatures from the base of the lithosphere to the mantle transition zone; however, their analysis was limited to the Tanzanian Craton and the directly adjacent rifts. To better constrain the physical properties responsible for the remarkable reduction in seismic velocities beneath the East African Rift, we present an analysis of P-wave attenuation from the Afar region in the north down to the start of the Kaapvaal Craton in the south. We rely on a time-domain measurement of Δt^* (Bezada, 2017) and construct a smoothed map of Δt^* with a Bayesian inverse method adapted from Malinverno and Briggs (2004). We then model our results to derive a range of reasonable attenuation values to determine to what extent temperature alone can explain variations in seismic velocity in the region.

DATA AND METHODS

Our attenuation measurements used data from 312 previously deployed stations, including temporary broadband seismic arrays and permanent broadband stations (Figure 2.1). We used P-wave arrivals of 63 deep focus (>200 km depth) teleseismic events from

30 to 90 degrees epicentral distance and magnitudes >5.5 Mw. Deep focus events were used to ensure the ray paths only passed through the highly attenuating asthenosphere on the receiver side. This study relied on regional data collected over different intervals in time, predominantly from short-term (1-3 year) deployments. We used long-running stations to calculate event statics to compensate for limited temporal overlap among the array deployments (Cafferky & Schmandt, 2015; Eilon & Abers, 2017). The quantity we measured that describes the attenuation of a phase, t^* with units of seconds, is defined by:

$$t^* = \int \frac{dt}{(Q(t))} = \int \frac{dr}{V(r) * Q(r)} \quad \text{Eq (1)}$$

Where t is the travel time, $Q(t)$ is the quality factor encountered by the P-wave at a given time during propagation, r is the distance along a ray path, $V(r)$ is velocity along that path, and $Q(r)$ is the quality factor along that path. This study calculated Δt^* , the relative changes to the integrated effect of attenuation over the ray path, by measuring the relative attenuation of the P-waves on an event-by-event basis. The absolute degree of attenuation included the effect of structures outside our study area. We measured Δt^* with a time-domain method that is more robust to confounding factors such as pre-signal noise and scattering compared to the traditional spectral-slope approach (Bezada et al., 2019; Byrnes et al., 2019).

To use the time-domain approach, we selected and stacked the seismic traces with the most impulsive first arrivals and the strongest high-frequency energy for a given event. This estimates the least-attenuated waveform for the given set of recorded P-waves. The

measurement of t^* is relative since the absolute degree of attenuation reflected by this estimated waveform was unknown. After we manually identified the sharpest waveforms, thin waveforms with the most singular point-like energy, we generated different versions of the waveform given different degrees of attenuation by applying the attenuation operator A of Azimi (1968) to the least-attenuated waveform. A is defined by:

$$A(\omega) = \exp \left\{ -\omega \Delta t^* \cdot \left[\frac{l}{2} + \frac{i}{\pi} \ln \ln \left(\frac{\omega}{\omega_0} \right) \right] \right\} \quad \text{Eq (2)}$$

Where ω is the angular frequency, ω_0 is a reference frequency that does not impact the results for relative measurements, and Δt^* is the degree of attenuation. We found the best-fitting value of Δt^* for a particular waveform with a grid search over Δt^* that minimizes the misfit between the synthetic source trace and the observed waveform in a selected window (Figure 2.2). The results were manually reviewed, and poor fits were culled through visual inspection.

After generating individual measurements of Δt^* , we used a Bayesian method adapted from Malinverno & Briggs (2004) to find a smoothed map of Δt^* for our region of interest. The first reason for using an inversion to process the results is that the mean value for each event is unknown. We overcome this unknown by solving for an "event static" that used recordings at common stations to level the events together so that there is only one unknown mean value for the entire dataset. Once the dataset is leveled, the values can be analyzed by looking at the averaged values at each station (Eilon & Abers, 2017; Venkataraman et al., 2004) or by constructing smoothed maps that combine data from

adjacent stations. The number of events recorded by individual stations in our datasets varies significantly, so a smoothed map of Δt^* better represents our results; however, the results are sensitive to the chosen smoothing length. We used a 30 km node on our main inversion, which generates a separate Δt^* estimate every 30 km before it is smoothed. An additional "station static" term may be necessary to account for anomalous values at stations that disagree with nearby results (see Bezada, 2017 for a discussion), which for measurements of attenuation can reflect the installation conditions of the station (Bezada et al., 2019). The weight given to the station statics introduces additional bias to the final result. We used the formalism of Malinverno & Briggs (2004) to construct a smoothed map of Δt^* that accounted for *a priori* uncertainty in the parameters that govern the generation of the smoothed map: the uncertainty of the measurements, the smoothing lengths, and the weight given to station terms. This formalism allowed the results to represent the complete *a priori* uncertainty and made the posterior uncertainty of the earth-model parameters independent from more questionable assumed values of the hyperparameters, such as the ideal smoothing length. The distribution of the realized hyperparameters (model covariance, smoothing length, station term covariance, and data error) are shown in Figure 2.3 for the overall data region and Figure 2.4 for a smaller Tanzania Craton subset region. The subsequent models and errors shown in Figures 2.5 and 2.6 are the mean and standard deviation of the realized instances of the mapped values.

RESULTS

Figure 2.5 shows the Δt^* map from the Bayesian inversion for the complete set of Δt^* values across eastern Africa, along with the associated standard deviation. Our results show a range of Δt^* , from a maximum observed value of 0.19 s to a minimum value of -0.15 s. In general, Δt^* values decrease from north to south, with the highest Δt^* values located along the southwestern edge of the Afar Depression. The Arabian Peninsula has a range of Δt^* values from 0.01 s to 0.07 s, and associated uncertainties range from 0.01 s to 0.025 s farther to the north. Values within the Afar region, including the northern half of the Main Ethiopian Rift (MER), range from 0.10 s to 0.19 s. Uncertainties in this region are generally low, with typical standard deviations of 0.015 s. However, uncertainties are larger along the southwestern edge of the region and approach a maximum uncertainty of 0.033 s. Southward along the Eastern Branch, Δt^* values steadily decrease from a maximum of roughly 0.13 s near the MER to values of approximately 0.06 s directly east of the northern shore of Lake Victoria and decrease further still to values of -0.02 s further south along the eastern edge of the Tanzanian Craton. Within the Tanzanian Craton, Δt^* values range from 0.05 s to -0.05 s, with the most significant values observed to the north and lowest to the east near the Western Branch. In this region, uncertainties are low and range from 0.008 s to 0.02 s. Along the Western Branch, Δt^* values begin moderately high, around 0.08 s, north of Lake Victoria and decrease to the south. We observe a localized low Δt^* (around -0.06 s) from a latitude of 2 °S to 6 °S before increasing slightly to the south. Values of Δt^* then steadily decrease along Lake Malawi. Our analysis extends to the Kaapvaal Craton, where we

observe a minimum Δt^* of -0.15 s: however, the standard deviation increases (~ 0.02 s to 0.03 s). In general, changes in standard deviation (uncertainty) are attributable to the density of station coverage: more stations in a region typically result in lower uncertainties.

While Δt^* appears to vary with latitude, our results suggest smaller scale lateral variations. Figure 2.6 focuses on the Tanzanian Craton from slightly north of Lake Victoria to the southernmost part of Lake Malawi. We use a different smoothing length (Figure 2.4) in this subset than within our overall Δt^* map. While intriguing, the relatively significant uncertainties in this inversion make it challenging to constrain these small-scale variations robustly. Uncertainties in this subset region are higher than in our larger study area; the increase in uncertainties correlates with an increase in the overall amplitudes of Δt^* . These higher uncertainties are likely due to us using only a subset of the t^* measurements and the limitations of our method on resolving small-scale structures. In this region, we observe a maximum in Δt^* (0.07-0.15s) northwest and southeast of Lake Victoria. Δt^* decreases (-0.03 s to -0.10 s) as we follow the Western Branch to the northern end of Lake Tanganyika. Venkataraman et al. (2004) found their highest values of Δt^* at ~ 0.4 , south of Lake Victoria, which decrease further east to around -0.4, only to rise again as they continue east. We see similar results but with different values. Our Δt^* values increase slightly north of Lake Malawi before reaching another minimum West of the southern end of Lake Malawi (-0.03 s to -0.10 s). Venkataraman et al. (2004) suggests a similar Δt^* increase north of Lake Malawi; however, their study region cuts off within the northern area of the Lake. Compared to

Venkataraman et al. (2004), our results follow similar trends with amplitude results above zero south of Lake Victoria and below zero to the East of Lake Victoria. Still, our maximum value (0.15 s) is smaller by 0.25 s. Our minimum value (-0.10) is larger by 0.3 s, potentially due to our increased number of events and their use of Tanzania network (XD) stations, which we did not include in our data. The XD network was a temporary short-term deployment in place from 1994 to 1995; we only collected data from stations deployed from 2000 to 2019.

In addition, to changes in Q_P in the asthenosphere, changes in lithospheric thickness can also play an important role in determining Δt^* and ultimately modeling Q_P (Zhu et al., 2021). Given the wide range of lithospheric thickness estimates for the region, careful consideration of this variability should be considered when constructing attenuation estimates. In the discussion, we focus on the long-wavelength variations in attenuation associated with the change in latitude, as observed in Figure 2.5. However, future work should constrain attenuation variations in the Tanzanian Craton-Malawi region more accurately.

DISCUSSION

Modeling estimates of attenuation

To generate estimates of asthenospheric Q_P beneath the East African Rift (EAR), we calculate two-layer comparative block models for the Eastern Branch, Western Branch, and the Afar region relative to the Kaapvaal Craton. Kaapvaal Craton has our study's minimum Δt^* values (Figure 2.7). We assume a lithospheric thickness of 100 km

beneath the Eastern Branch (Δt^* difference of 0.1889 ± 0.19 relative to the Kaapvaal Craton) and a lithospheric V_p of 8.2 km/s and asthenospheric V_p of 7.6 km/s. In the Western Branch (Δt^* difference of 0.2120 ± 0.02 relative to the Kaapvaal Craton), we assume a lithospheric thickness of 105 km, lithospheric V_p of 8.4 km/s, and asthenospheric V_p of 7.9 km/s. Within the Afar region (Δt^* difference of 0.3311 ± 0.04 relative to the Kaapvaal Craton), we assume a lithospheric thickness of 66 km, lithospheric V_p of 7.9 km/s, and asthenospheric V_p of 7.2 km/s. For the Kaapvaal Craton, we used a lithospheric thickness of 155 km (although a case for 200 km is also shown in Figure 2.7 and discussed later), a lithospheric V_p of 8.4 km/s, and an asthenospheric V_p of 7.9 km/s.

We determined the V_p values for each region by taking each region's average maximum and minimum shear velocities from Emry et al. (2019) and assuming a V_p/V_s ratio of 1.8. To determine lithospheric thickness for each location, we compared the average range of depths of the maximum and minimum velocities from Emry et al. (2019) to previously published receiver function studies. Sp receiver function analysis in Southern, Central, and Eastern Africa (Hansen et al., 2009) found thicker lithosphere under the Precambrian Kaapvaal Craton and Namaqua-Natal Belt (155 km, 140 km) and thinner lithosphere under the edge of the Ethiopian Rift and Afar Depression (80 km, 34 km). Sp receiver functions focusing on the northern region of the EAR provided constraints of an average lithosphere-asthenosphere boundary (LAB) depth of 67 ± 3 km under the Ethiopian Plateau (Lavayssiere et al., 2018). Liu et al. (2020) proposed LAB depths of 50-132 km with a mean of 77 ± 15 km in the southern portion of the EAR and cratonic centers

(Tanzania, Kaapvaal, and the Arabian platform) with a LAB of 100-130 km. Hopper et al. (2020) found LAB depths of 100 km to the west of the southern portion of the Western Branch, 55 km on the rift itself, and 125 km to the east. Receiver function analyses of the Kaapvaal cratonic lithosphere provide evidence for negative velocity contrasts ranging from 130 km to 300 km (Hansen et al., 2019; Liu et al., 2020; Wittlinger & Farra, 2007). Prior studies debate whether these phases represent the LAB or other structures internal to the lithosphere (Fishwick, 2010). Meanwhile, estimates of lithospheric thickness from tomography models range from 180 km (Fishwick, 2010) to 300 km (Fouch et al., 2004). In our model, we assume that the lithosphere beneath Kaapvaal extends to 155 km depth. We also test a case where the lithosphere is 200 km thick. For the Western Branch, we assume a lithospheric thickness of 105 km and an Eastern Branch lithospheric thickness of 100 km. We assume a lithospheric thickness of 66 km for Afar for our two-layer model and 50 km for the three-layer model.

In all our models, we assume a lithospheric Q_P of 1300, following PREM (Dziewonski & Anderson, 1981), and an asthenospheric Q_P beneath the Kaapvaal Craton of 180, the globally averaged asthenospheric value (Byrnes & Bezada, 2020). With these assumptions, we calculate the best fitting asthenospheric Q_P for Afar, and the Western and Eastern Branches, given the differential Δt^* values listed above and shown in Figure 2.5. We calculated each asthenospheric Q_P value by varying the depth to the bottom of the low Q_P (asthenospheric) layer from 200 to 400 km (Figure 2.7). A depth of 200 km is the bound for our thinnest potential asthenospheric layer based on the depth extent of the globally averaged high attenuation region (220 km) determined by PREM (Dziewonski &

Anderson, 1981). Venkataraman et al. (2004) modeled their results assuming a thick low Q_P layer extending down to the mantle transition zone, which we approximate with our lower bound of 400 km. As we increase the depth to the base of the assumed low Q_P layer, we observe an increase in Q_P or a reduction in attenuation (attenuation is equal to the inverse of Q_P). The reason for this increase is that as the path length of the waveform through the low Q_P layer (dr in Equation 1) increases, and as a result, an increase in Q_P maintains constant t^* . If we assume that the asthenosphere terminates at 200 km depth, values of Q_P are 58 ± 5 beneath the Eastern Branch, 48 ± 5 beneath the Western Branch, and 50 ± 6 beneath the Afar region. These values suggest that attenuation is greater beneath the Western Branch rather than the Afar region, where the lowest seismic velocities are (Bastow et al., 2008; Emry et al., 2019), and the presumed center of the Afar mantle plume is located (Boyce et al., 2021). The difference in assumed lithospheric thicknesses beneath both regions is the likely explanation for the lower Q_P value beneath the Western Branch versus the Afar region. The low Q_P layer is at a constant base depth, leading to a thinner asthenospheric layer (100 km thick) relative to Afar's asthenospheric layer (134 km), accommodating the relatively high Δt^* of the Western Branch. The Q_P of the Afar region, at a 250 km terminating asthenospheric depth, becomes smaller in magnitude relative to the Western Branch and is the most attenuating of the three regions (Afar $Q_P = 63 \pm 7$, Western Branch $Q_P = 65 \pm 6$, and Eastern Branch $Q_P = 76 \pm 6$). At 400 km asthenospheric depth, Q_P beneath Afar is the lowest (91 ± 7 , compared to 96 ± 7 beneath the Western Branch and 108 ± 6 beneath the Eastern Branch). The previously modeled rift Q_P of ~ 80 (Venkataraman et al., 2004) beneath the Eastern and Western

Branches is lower than our values calculated with a comparable 400 km terminating asthenosphere. We approach equivalent values if we assume the low Q_P layer extends to depths between 250 and 300 km for the Eastern Branch and between 300 and 350 km for the Western Branch. In the remainder of our discussion, we favor models where the low Q_P region (high attenuation) base extends to depths of 200 or 250 km. We prioritize these models because of estimates of the extent of high attenuation in PREM (220 km; Dziewonski & Anderson, 1981) and from more recent work, which has shown that the changes in t^* from our methodology are most sensitive to changes in attenuation at depths of ≤ 220 km (Castaneda et al., 2021; Liu et al., 2021; Zhu et al., 2021).

In our analysis, we generate a second set of models focusing on the Afar region (Figure 2.7), which contains the largest Δt^* values and the slowest velocities (Emry et al., 2019) in our study area. We calculate how Q_P would vary in the Afar region using a three-layer model to test the plausibility of a melt-rich layer embedded within the asthenosphere. The three-layer model consists of an assumed melt-free lithosphere overlying a low Q_P layer (in which we vary the thickness), which itself overlies a third layer of average asthenosphere (Q_P of 180) that extends to a depth of 250 km. Our suite of models is conceptually similar to models of mid-ocean ridge systems, which contain a melt-rich, low Q_P layer bounded by the mantle lithosphere above and an asthenospheric layer with less concentrated melt below (Eilon & Abers, 2017). A similar melt layer has been proposed beneath the Salton Trough (Byrnes & Bezada, 2020) and under Afar (Rychert et al., 2012). In this suite of models, we assume that Afar has a lithospheric thickness of 50 km, whereas in our initial modeling of Afar in the two-layer cases, we assumed a

lithospheric thickness of 66 km. We determined this value (66 km) based on the averaged values from Emry et al. (2019) combined with receiver function estimates; such estimates vary significantly, with some estimates putting the lithospheric thickness beneath Afar as thin as 25 km (Rychert et al., 2012). Decreasing the estimated thickness from 66 km to 50 km generates a larger Q_P for the calculated low Q_P layer, reducing the associated attenuation estimate. Similar to our two-layer models, as we increase the thickness of our low Q_P layer, the Q_P increases (attenuation decreases) within that layer. For our three-layer model with the thinnest low Q_P layer (20 km), we observe a modeled Q_P of 9 ± 2 (155 km thick craton) and 10 ± 2 (200 km thick craton). At a thickness of 200 km, the values of Q_P are 61 ± 6 and 66 ± 7 .

In addition to assessing how changes to the Afar lithospheric thickness impacted our results, we also tested how variations in the thickness of the Kaapvaal lithosphere could impact our analysis. Hansen et al. (2009) estimated the base of the Kaapvaal Craton to be 155 km. However, the base of the lithosphere in older cratonic regions is often harder to detect with receiver functions (e.g., Fischer et al., 2010) because of gradual transitions from the lithosphere to the asthenosphere (Liu et al., 2020). We tested two different thicknesses to determine the impact of the Kaapvaal Craton thickness on our results. We observe that changing the thickness from 155 km to 200 km does not significantly impact our results in the case of our three-layer models for the Afar region (Figure 2.7).

Comparison of modeled attenuation to other studies

How then, do our modeled Q_P values compare to studies of Q elsewhere, and what might our values of Q_P indicate about the state of the mantle beneath the EAR? Global 1D model PREM constrains a Q_P of 180 for the asthenosphere, which extends to a depth of 220 km (Dziewonski & Anderson, 1981). The two-layer modeled Q_P falls well below the globally averaged asthenospheric Q_P whether we assume that the base of the asthenosphere extends to 200 km or 400 km. For our preferred 200 and 250 km two-layer models, Q_P is roughly 50 to 75. Q_P values within the two-layer model are primarily inconsistent with Q in melt-producing regions elsewhere ($Q_P < 50$; Abers et al., 2014). Our Q_P values suggest that the two-layer model may not be physically realistic given petrological (Rooney et al., 2012) and volcanic (Albino & Biggs, 2021) evidence of melt within the East African Rift. Eilon and Abers (2017) constrained Q_S of ≤ 25 or $Q_P \leq 56.25$ (assuming a Q_P/Q_S of 2.25; Karato & Spetzler, 1990) beneath the Juan de Fuca and Gorda Ridges. In their model, they assume no lithosphere, and that the melt fraction, at a depth of approximately 60 km, is most concentrated above the dry melting, although melt continues to a depth of 150 km. If we assume that the Q_P for our three-layer model is 56.25 (Eilon & Abers, 2017), our low Q_P layer would need to be approximately 190 km thick. In the Salton Trough, another region of continental rifting, Q_P has been estimated at 33 to 100 (Byrnes & Bezada, 2020), consistent with our calculated Afar Q_P from the two- and three-layer (attenuating layer of > 70 km) models. If we assume that the three-layer models where the highly attenuating layer is thin (< 50 km) are correct, the inferred Q_P would make Afar among the most attenuating regions on Earth (Byrnes & Bezada, 2020).

Calculating velocity anomalies from modeled attenuation

Using values for Q_P from both our two-layer and three-layer models, we calculate a range of P-wave velocity perturbations and thermal anomalies for various cases using the relationship below (Karato 1993):

$$\frac{\partial \ln V}{\partial T} = \frac{\partial \ln V_0}{\partial T} - F(\alpha) \left(\frac{Q^{-1}(\omega, T)}{\pi} \right) \left(\frac{H^*}{RT^2} \right) \quad \text{Eq (3)}$$

For all of the following calculations, we assume $\partial \ln V_0 / \partial T = -5 \times 10^{-5} \text{ K}^{-1}$, an activation enthalpy of $H^* = 500 \text{ kJ/mol}$, $T = 1600 \text{ K}$, and $F(\alpha) = 1$ for a constant Q_P (Karato, 1993).

We calculate the potential velocity anomaly (%Vp) using a 140 K temperature differential (∂T), determined through petrological analysis using PRIMELT-2 software (Herzberg & Asimow, 2008), of primitive (younger than 10 Ma) magmas within the Main Ethiopian Rift (Rooney et al., 2012). We calculate the P-wave velocity anomaly (expressed in percent) using the Q_P previously determined through modeling (Figure 2.7). We observe a range of velocity anomalies from -2.9% to -1.7% within the two-layer system. For the case where our asthenosphere terminates at 200 km, the largest values of velocity anomaly are observed under the Western Branch ($-2.9\% \pm .2\%$), followed closely by Afar ($-2.8 \pm .2\%$) and the Eastern Branch ($-2.5 \pm .2\%$). The percent velocity anomaly decreases as we increase the terminating depth of the asthenosphere within our model. At 250 km, the velocity anomaly is largest under Afar ($-2.4 \pm .2\%$) rather than the Western Branch ($-2.3 \pm .1\%$) and the smallest beneath the Eastern Branch ($-2.1 \pm .1\%$). The range of values we find within our two-layer model roughly agrees with the 2%

anomaly calculated by Rooney et al. (2012). This 2% anomaly underestimates the 6% velocity anomaly previously determined for the Afar region (Bastow et al., 2008). The largest velocity anomaly calculated within our two-layer model (2.9%) is approximately half the imaged 6%. In contrast, our three-layer model generates a range of velocity anomalies from -12% to -2% when simulating an enhanced low Q_P layer within the asthenosphere. A low Q_P layer of approximately 40-50 km can account for the 6% velocity anomaly within the Afar region (Figure 7), layers thinner than 40 km overestimate the velocity anomaly, and layers thicker than 50 km underestimate the velocity anomaly.

To calculate a range of potential temperature differentials, we input previously determined percent velocity anomalies from Bastow et al. (2018) (6% within the Afar region) and Ritsema et al. (1998) (4% within the Eastern and Western Branches) into equation 3 in place of the P-wave velocity perturbations ($\delta \ln V$), given the calculated Q_P (Figure 2.8). While we report the results of the calculated potential temperature differentials using the 4% and 6% velocity anomaly estimates for all three regions, we note that the results of Bastow et al. (2008) are most applicable to the Main Ethiopian Rift. The results of Ritsema et al. (1998) are most applicable to the Eastern and Western Branches, although past studies have found a 4% anomaly within the Afar region (Boyce et al., 2021). The calculated temperature anomaly for Afar with a 4% velocity anomaly is 237 ± 17 K for a 250 km terminating asthenosphere. The temperature anomaly for Afar with a 6% velocity anomaly is 356 ± 25 K at the same terminating depth. The calculated temperature anomaly with a 4% velocity anomaly (at 250 km terminating asthenosphere)

is 269 ± 14 K for the Eastern Branch and 242 ± 16 K for the Western Branch. If we increase the terminating depth to 400 km, the temperature anomaly for the Eastern Branch (312 ± 13 K) and Western Branch (335 ± 11 K) increases.

CONCLUSION

This study constrains differential attenuation (Δt^*) for the East Africa Rift system and nearby regions starting north of Afar and extending to the Kaapvaal Craton in the south. We find high Δt^* values (maximum of 0.19 s) just southwest of the Afar region and low Δt^* values (minimum of -0.15 s) beneath the Kaapvaal Craton. We find a general trend of high Δt^* values beneath the northern sections of the Western and Eastern Branches, which decreases further south. Assuming a variety of two- and three-layer model geometries, we utilize values of Δt^* in order to determine Q_P . The two-layer model is thought to represent a plume-like end member, while the three-layer model is thought to represent a low Q layer embedded within the asthenosphere. The two-layer model Q_P results are larger (Q_P from 50-91 for Afar) than typical for a melt-producing region ($<50 Q_P$; Abers et al., 2014), inconsistent with the melt produced within the East African Rift. Ignoring this inconsistency, the associated calculated velocity anomalies are 2-3% less than values found in previous geophysical studies (Bastow et al., 2008; Ritsema et al., 1998).

Our three-layer model models a low Q layer similar to values observed at mid-ocean ridges (Eilon & Abers, 2017). Using the three-layer model results, we find that a low Q_P layer (18-41 Q_P), 40-110 km thick, is sufficient to explain the 140 K temperature

anomaly and the 6% to 4% velocity anomaly previously reported in petrological (Rooney et al., 2012) and geophysical studies (Bastow et al., 2008; Ritsema et al., 1998). A Q_p of 18-41 is consistent with the presence of melt. Independent seismic evidence supports a 75 km thick melt layer beneath Afar (Rychert et al., 2012) and follows previous models for rift mechanics (Eilon & Abers, 2017). In conclusion, our work supports a model in which a melt-rich layer is embedded within the mantle asthenosphere. Such a model can account for previous petrological and geophysical constraints without invoking the requirement of additional thermal perturbations above what has been constrained previously.

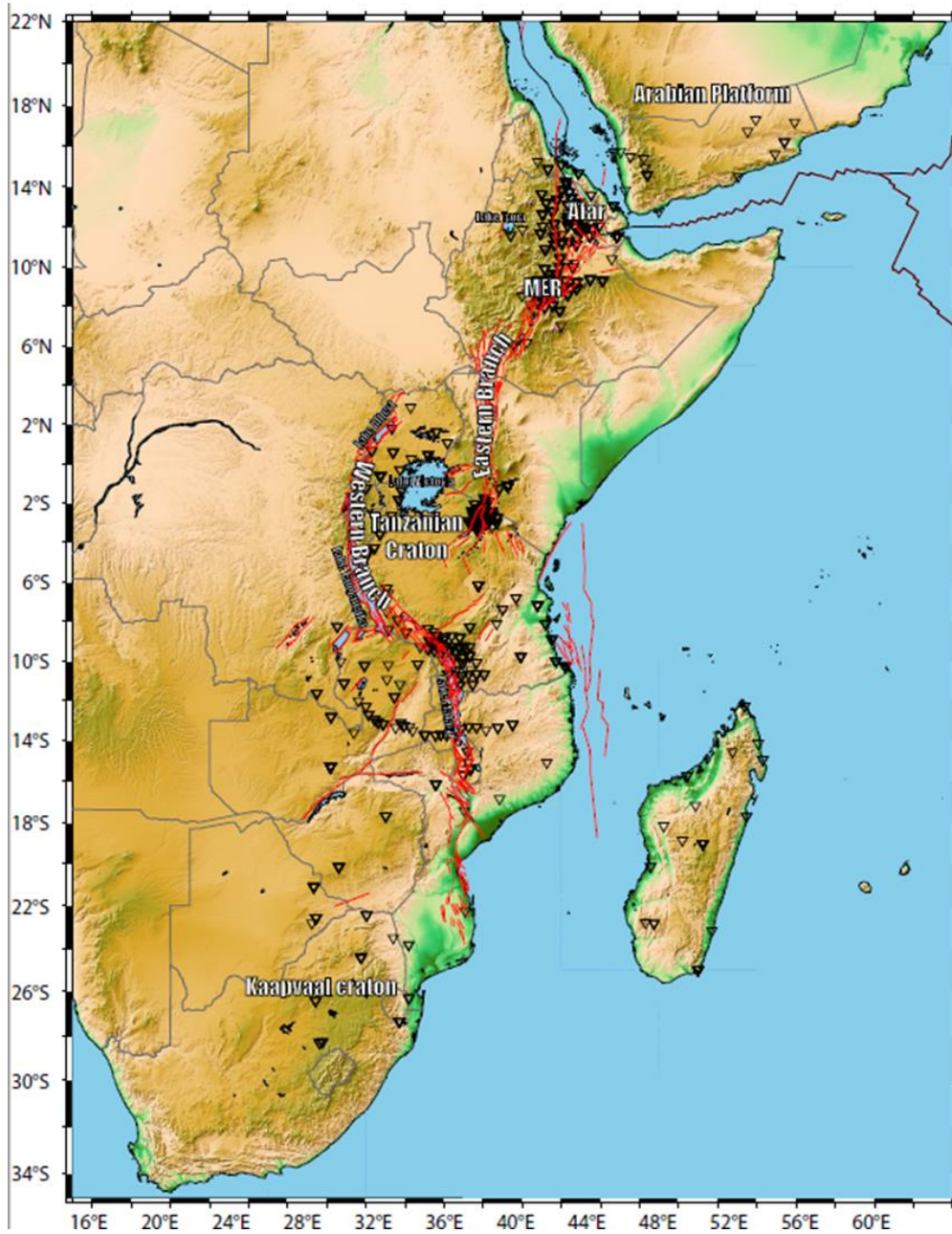


Figure 2.1 Map of our study area. Inverted black triangles show the locations of the 312 stations used. Red lines denote fault locations (Meghraoui, et al., 2016). Rift sections and lakes referred to in the text are labeled accordingly.

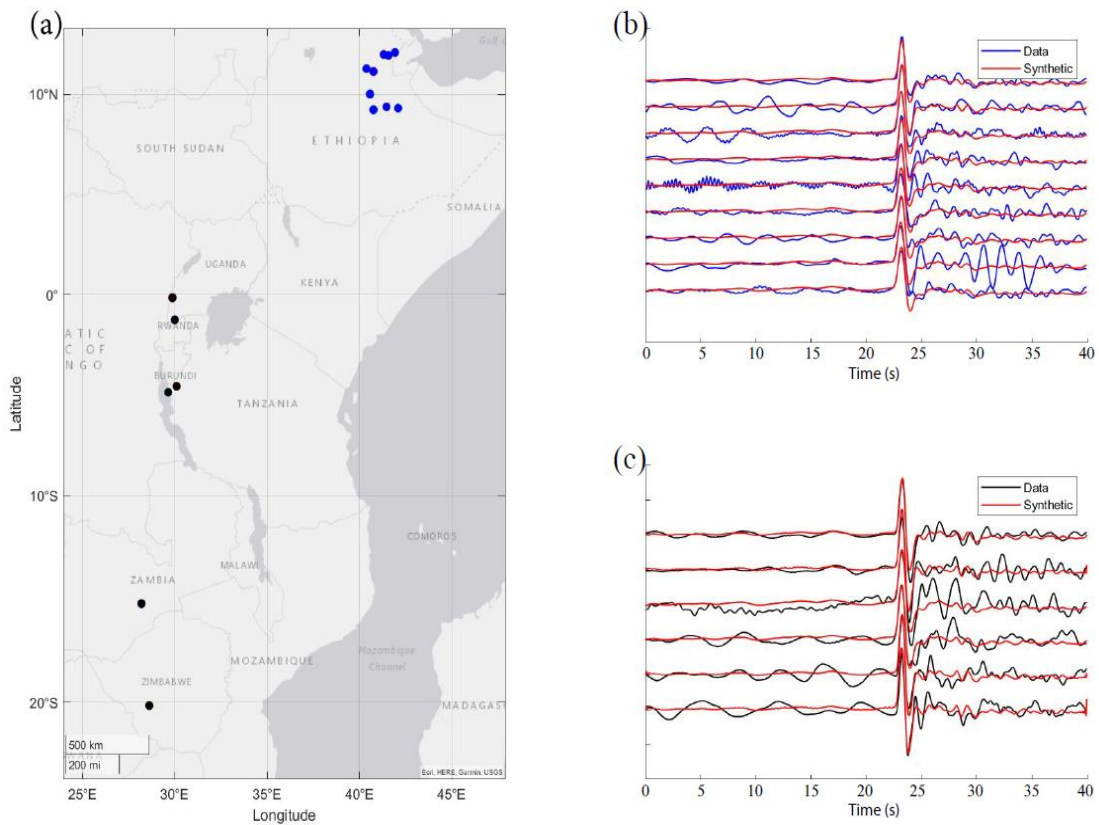


Figure 2.2 Example of waveform matching results for a single event (lat: -7.6795, long: 116.866, time: 2008-02-07 20:58:19, magnitude: 5.7, Depth: 323.5 km). (a) The locations of the stations used in this example are marked as blue and black points. (b) Data and synthetics from stations within the Afar region (blue points). The y-axis is individual stations ordered by latitude from the northernmost location down to the southernmost location. The x-axis shows time in seconds. Red lines represent synthetic data attenuated from the prototype source trace, while blue lines represent observed data. (c) Data and synthetics from the Lake Malawi and Kaapvaal Craton regions. The y-axis is individual stations ordered by latitude from the northernmost location down to the southernmost location. The x-axis shows time in seconds. The red lines represent synthetic data attenuated from the prototype source traces, and the black lines represent the observed data.

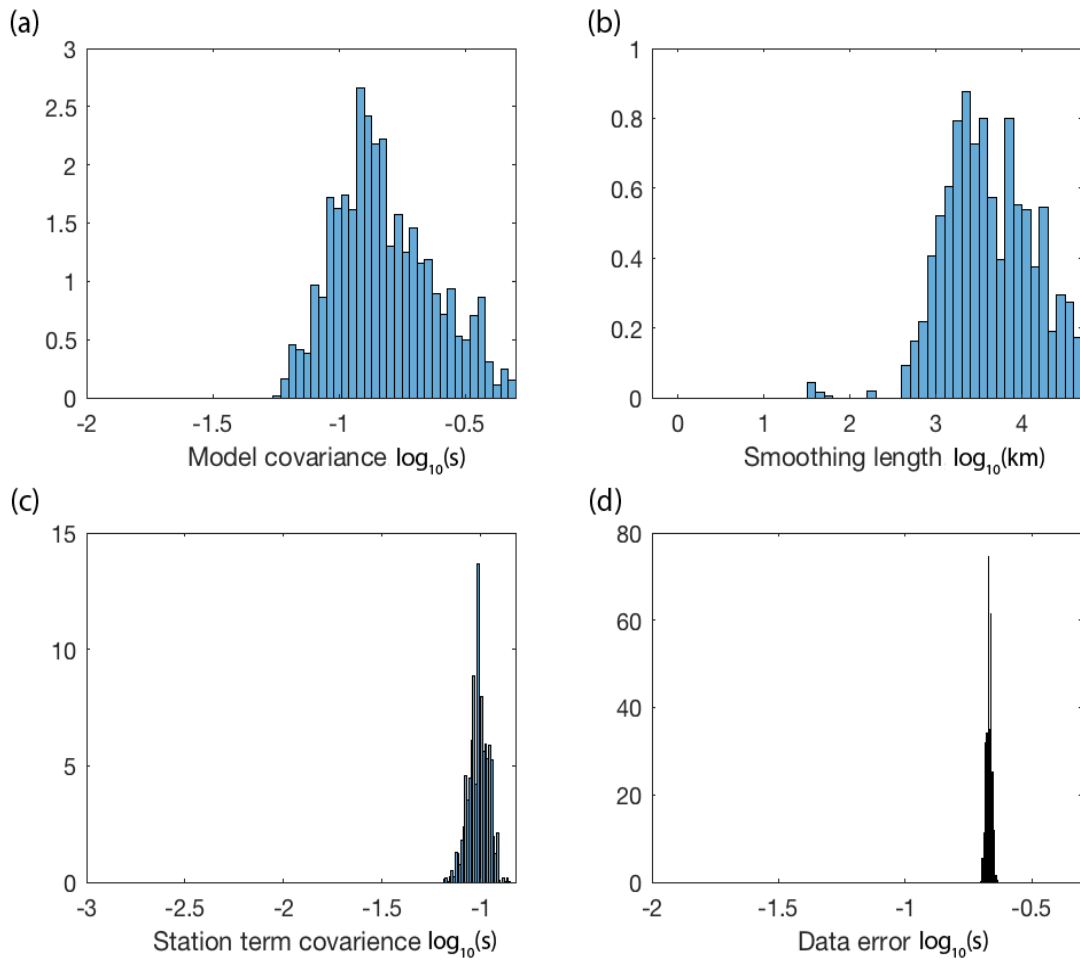


Figure 2.3. Distribution of the realized hyperparameters for the overall Δt^* inversion (Figure 2.5). (a) Model covariance used in our overall Δt^* inversion (Figure 2.5). The y-axis is a measure of confidence. The x-axis shows that our model favored a posterior estimate of $-\log_{10}(0.93)$ to $-\log_{10}(0.9)$ seconds for our model covariance. (b) Smoothing length used in our overall Δt^* inversion (Figure 2.5). The y-axis is a measure of confidence; the x-axis shows that our model favored a posterior estimate of $\log_{10}(3.3)$ to $\log_{10}(3.4)$ km. (c) Station term covariance used in our overall Δt^* inversion (Figure 2.5). The y-axis is a measure of confidence; the x-axis shows that our model favored a posterior estimate of $-\log_{10}(1.2)$ to $-\log_{10}(0.9)$ seconds. (d) Data error in our overall Δt^* inversion (Figure 2.5) The y-axis is a measure of confidence, and the x-axis shows that our data error is within a range from $-\log_{10}(0.65)$ to $-\log_{10}(0.6)$ seconds.

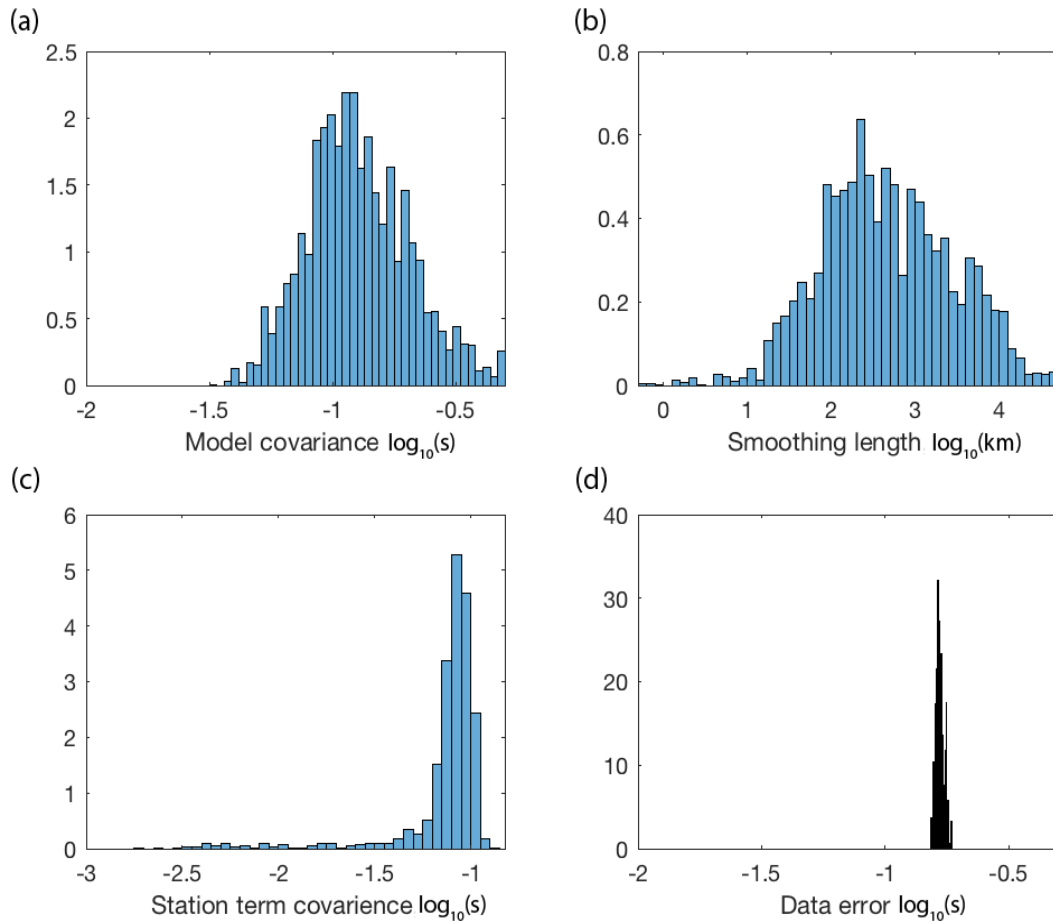


Figure 2.4 Distribution of the realized hyperparameters for the lower Western and Eastern Branch segments of Δt^* inversion (Figure 6). (a) Model covariance used in our subset Δt^* inversion (Figure 2.6). The y-axis is a measure of confidence. The x-axis shows that our model favored a posterior estimate of $-\log_{10}(1.2)$ to $-\log_{10}(0.9)$ seconds for our model covariance. (b) Smoothing length used in our subset Δt^* inversion (Figure 2.6). The y-axis is a measure of confidence; the x-axis shows that our model favored a posterior estimate of $\log_{10}(2)$ to $\log_{10}(3)$ km. (c) Station term covariance used in our subset Δt^* inversion (Figure 2.6). The y-axis is a measure of confidence; the x-axis shows that our model favored a posterior estimate of $-\log_{10}(1.7)$ to $-\log_{10}(1)$ seconds. (d) Data error in our subset Δt^* inversion (Figure 6). The y-axis is a measure of confidence, and the x-axis shows that our data error is within a range from $-\log_{10}(0.75)$ to $-\log_{10}(0.65)$ seconds.

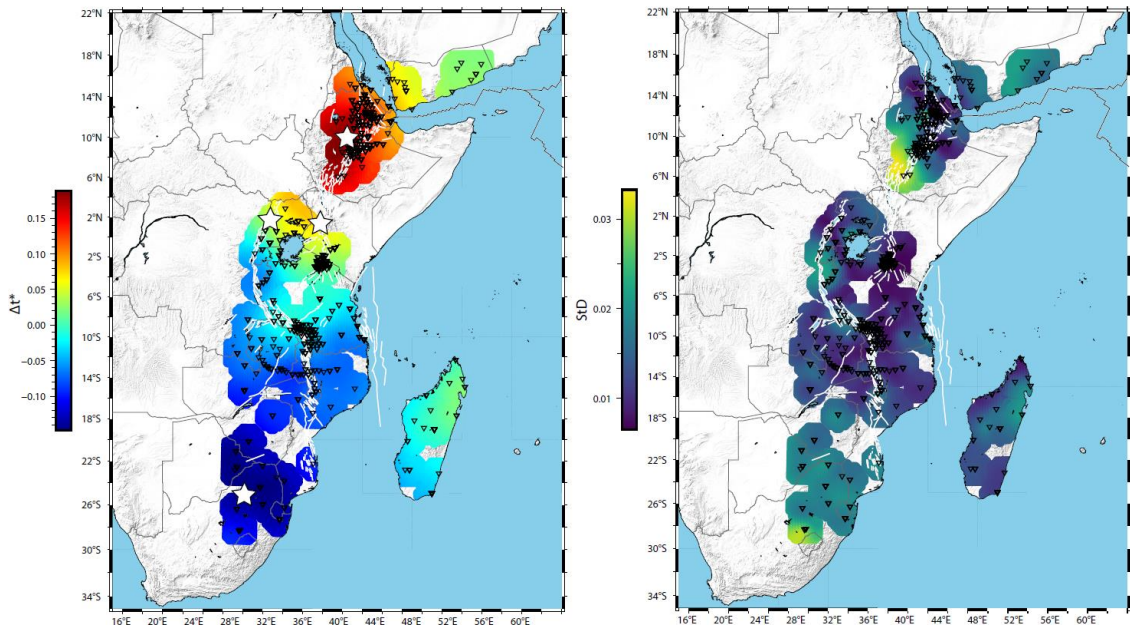


Figure 2.5 (Left) Model of P-wave Δt^* inversion; stars indicate the approximate location of our modeled regions. (Right) one standard deviation of Δt^* . White lines for both maps denote fault lines.

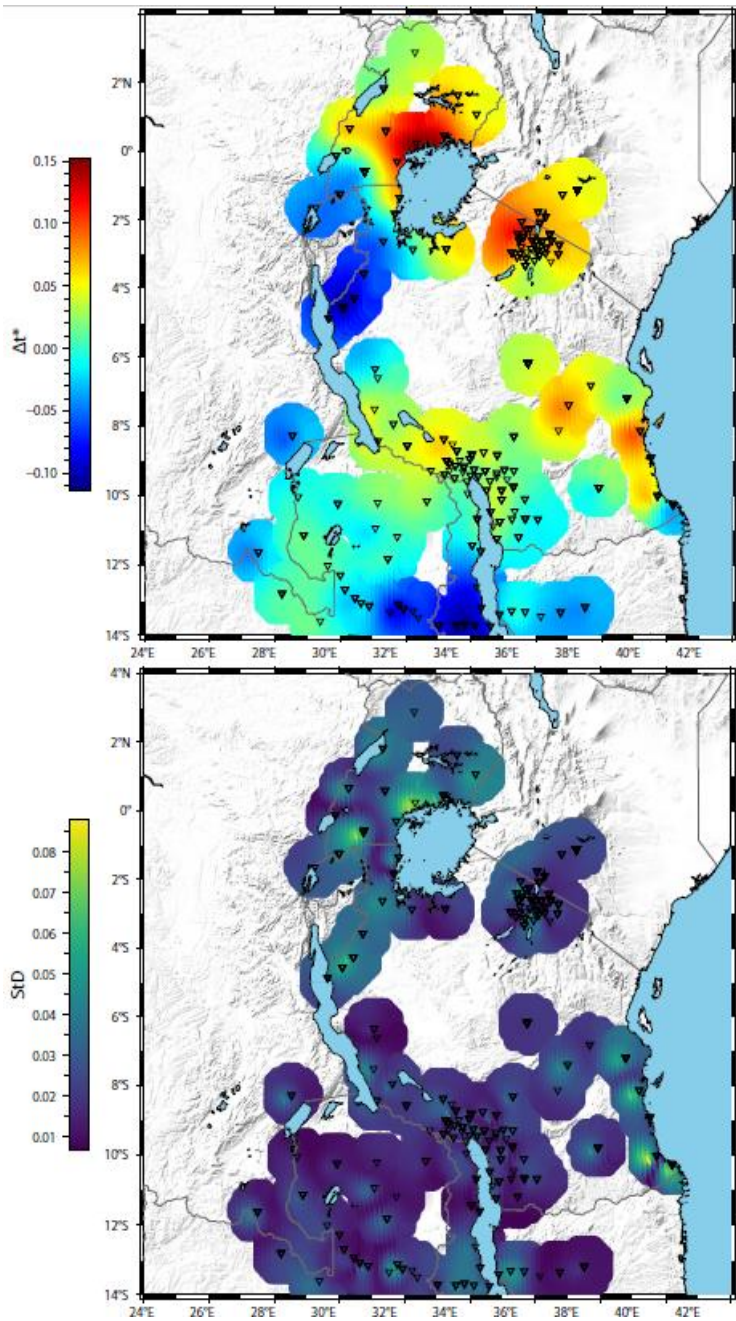


Figure 2.6 (Top) Model of P-wave Δt^* inversion calculated using a subset region of our overall study area, consisting of the lower Western and Eastern Branch segments. (Bottom) one standard deviation of Δt^* . White lines for both maps denote fault lines

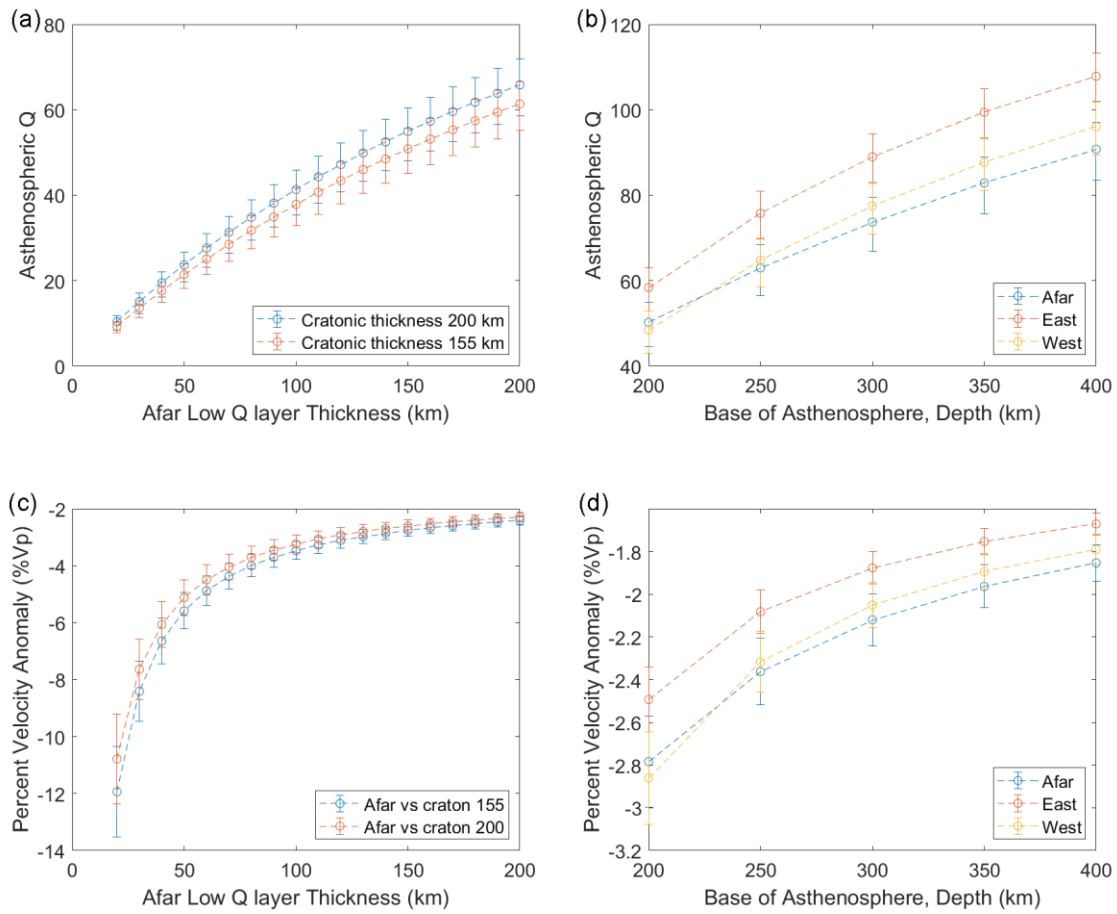


Figure 2.7 The left column of this figure (a,c) shows a three-layer model of Afar where the middle layer of the asthenosphere varies in thickness and the third layer terminates at a depth of 250 km. We compare Afar (50 km thick lithosphere) with Kaapvaal Craton (155 km and 200 km thick). The right column of this figure (b,d) shows a two-layer model where the lithosphere overlies a single layer of asthenosphere that terminates at varying depths from 200 to 400 km. We display data for three regions (Afar - 66 km thick lithosphere, Eastern Branch- 100 km thick lithosphere, Western Branch- 105 km thick lithosphere) compared to Kaapvaal - 155 km thick lithosphere. (a) Three-layer model showing potential Q_p values for Afar for the associated thickness of a low Q_p mid-asthenosphere layer (b) Two-layer model showing potential Q_p values for Afar, Eastern Branch, and Western Branch for associated terminating depths of the asthenosphere. (c) Three-layer model showing potential velocity derivatives for Afar assuming a 140 °C (Rooney et al., 2012) temperature anomaly and estimated Q_p from (a). (d) Two-layer model showing potential velocity derivatives for Afar, Eastern Branch, and Western Branch assuming a 140 °C (Rooney et al., 2012) temperature anomaly and estimated Q_p from (b).

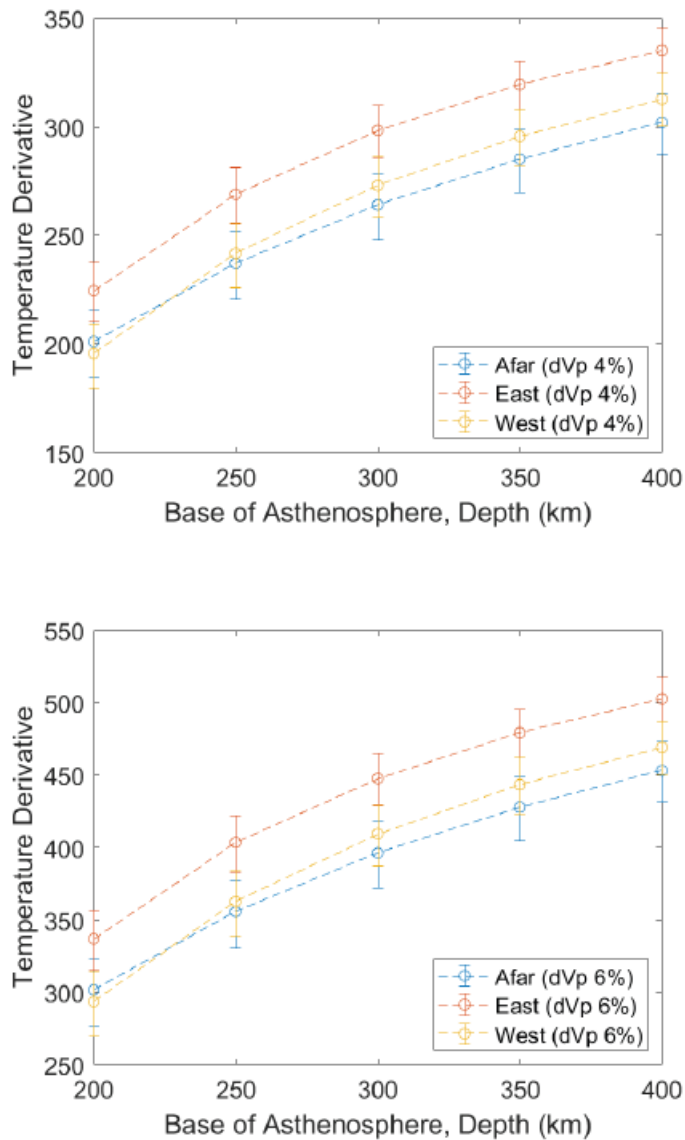


Figure 2.8 (Top) two-layer model showing potential temperature anomaly for Afar, Eastern Branch, and Western Branch assuming a 4% velocity anomaly from Ritsema et al. (1998) and estimated Q_P (Figure 2.7). (Bottom) Two-layer model showing potential temperature anomaly for Afar, Eastern Branch, and Western Branch assuming a 6% velocity anomaly from Bastow et al. 2008 and estimated Q_P (figure 2.7).

REFERENCES

- Abers, G. A., Fischer, K. M., Hirth, G., Wiens, D. A., Plank, T., Holtzman, B. K., ... & Gazel, E. (2014). Reconciling mantle attenuation-temperature relationships from seismology, petrology, and laboratory measurements. *Geochemistry, Geophysics, Geosystems*, 15(9), 3521-3542.
- Adams, A., Miller, J., & Accardo, N. (2018). Relationships between lithospheric structures and rifting in the East African Rift System: A Rayleigh wave tomography study. *Geochemistry, Geophysics, Geosystems*, 19(10), 3793-3810.
- Aizawa, Y., Barnhoorn, A., Faul, U. H., Fitz Gerald, J. D., Jackson, I., & Kovács, I. (2008). Seismic properties of Anita Bay dunite: an exploratory study of the influence of water. *Journal of Petrology*, 49(4), 841-855.
- Albino, F., & Biggs, J. (2021). Magmatic processes in the East African Rift system: insights from a 2015–2020 Sentinel-1 InSAR survey. *Geochemistry, Geophysics, Geosystems*, 22(3), e2020GC009488.
- Azimi, S. A. (1968). Impulse and transient characteristics of media with linear and quadratic absorption laws, *Izvestiya. Phys. of the Solid Earth*, 88-93.
- Bastow, I. D., Nyblade, A. A., Stuart, G. W., Rooney, T. O., & Benoit, M. H. (2008). Upper mantle seismic structure beneath the Ethiopian hot spot: Rifting at the edge of the African low-velocity anomaly. *Geochemistry, Geophysics, Geosystems*, 9(12).
- Bastow, I. D., Stuart, G. W., Kendall, J. M., & Ebinger, C. J. (2005). Upper-mantle seismic structure in a region of incipient continental breakup: northern Ethiopian rift. *Geophysical Journal International*, 162(2), 479-493.
- Benoit, M. H., Nyblade, A. A., & VanDecar, J. C. (2006). Upper mantle P-wave speed variations beneath Ethiopia and the origin of the Afar hotspot. *Geology*, 34(5), 329-332.
- Bezada, M. J. (2017). Insights into the lithospheric architecture of Iberia and Morocco from teleseismic body-wave attenuation. *Earth and Planetary Science Letters*, 478, 14-26.
- Bezada, M. J., Byrnes, J., & Eilon, Z. (2019). On the robustness of attenuation measurements on teleseismic P waves: insights from micro-array analysis of the 2017 North Korean nuclear test. *Geophysical Journal International*, 218(1), 573-585.
- Boyce, A., Bastow, I. D., Cottaar, S., Kounoudis, R., Guilloud De Courbeville, J., Caunt, E., & Desai, S. (2021). AFRP20: New P-wavespeed model for the African mantle reveals two whole-mantle plumes below East Africa and neoproterozoic

- modification of the Tanzania Craton. *Geochemistry, Geophysics, Geosystems*, 22(3), e2020GC009302.
- Byrnes, J. S., & Bezada, M. (2020). Dynamic upwelling beneath the Salton Trough imaged with teleseismic attenuation tomography. *Journal of Geophysical Research: Solid Earth*, 125(11), e2020JB020347.
- Byrnes, J. S., Bezada, M., Long, M. D., & Benoit, M. H. (2019). Thin lithosphere beneath the central Appalachian Mountains: Constraints from seismic attenuation beneath the MAGIC array. *Earth and Planetary Science Letters*, 519, 297-307.
- Cafferky, S., & Schmandt, B. (2015). Teleseismic P wave spectra from USArray and implications for upper mantle attenuation and scattering. *Geochemistry, Geophysics, Geosystems*, 16(10), 3343-3361.
- Chang, S. J., Kendall, E., Davaille, A., & Ferreira, A. M. (2020). The evolution of mantle plumes in East Africa. *Journal of Geophysical Research: Solid Earth*, 125(12), e2020JB019929.
- Civiero, C., Goes, S., Hammond, J. O., Fishwick, S., Ahmed, A., Ayele, A., ... & Stuart, G. W. (2016). Small-scale thermal upwellings under the northern East African Rift from S travel time tomography. *Journal of Geophysical Research: Solid Earth*, 121(10), 7395-7408.
- Cline Ii, C. J., Faul, U. H., David, E. C., Berry, A. J., & Jackson, I. (2018). Redox-influenced seismic properties of upper-mantle olivine. *Nature*, 555(7696), 355-358.
- Courtier, A. M., Jackson, M. G., Lawrence, J. F., Wang, Z., Lee, C. T. A., Halama, R., ... & Chen, W. P. (2007). Correlation of seismic and petrologic thermometers suggests deep thermal anomalies beneath hotspots. *Earth and Planetary Science Letters*, 264(1-2), 308-316.
- Dugda, M. T., Nyblade, A. A., & Julia, J. (2007). Thin lithosphere beneath the Ethiopian Plateau revealed by a joint inversion of Rayleigh wave group velocities and receiver functions. *Journal of Geophysical Research: Solid Earth*, 112(B8).
- Dziewonski, A. M., & Anderson, D. L. (1981). Preliminary reference Earth model. *Physics of the earth and planetary interiors*, 25(4), 297-356.
- Eilon, Z. C., & Abers, G. A. (2017). High seismic attenuation at a mid-ocean ridge reveals the distribution of deep melt. *Science advances*, 3(5), e1602829.
- Emry, E. L., Shen, Y., Nyblade, A. A., Flinders, A., & Bao, X. (2019). Upper mantle Earth structure in Africa from full-wave ambient noise tomography. *Geochemistry, Geophysics, Geosystems*, 20(1), 120-147.

- Faul, U. H., & Jackson, I. (2005). The seismological signature of temperature and grain size variations in the upper mantle. *Earth and Planetary Science Letters*, 234(1-2), 119-134.
- Faul, U. H., Fitz Gerald, J. D., & Jackson, I. (2004). Shear wave attenuation and dispersion in melt-bearing olivine polycrystals: 2. Microstructural interpretation and seismological implications. *Journal of Geophysical Research: Solid Earth*, 109(B6).
- Ferguson, D. J., MacLennan, J., Bastow, I. D., Pyle, D. M., Jones, S. M., Keir, D., ... & Yirgu, G. (2013). Melting during late-stage rifting in Afar is hot and deep. *Nature*, 499(7456), 70-73.
- Fishwick, S. (2010). Surface wave tomography: imaging of the lithosphere–asthenosphere boundary beneath central and southern Africa?. *Lithos*, 120(1-2), 63-73.
- Fouch, M. J., James, D. E., VanDecar, J. C., Van der Lee, S., & Kaapvaal Seismic Group. (2004). Mantle seismic structure beneath the Kaapvaal and Zimbabwe Cratons. *South African Journal of Geology*, 107(1-2), 33-44.
- Gallacher, R. J., Keir, D., Harmon, N., Stuart, G., Leroy, S., Hammond, J. O., ... & Ahmed, A. (2016). The initiation of segmented buoyancy-driven melting during continental breakup. *Nature Communications*, 7(1), 1-9.
- Hammond, J. O., Kendall, J. M., Stuart, G. W., Ebinger, C. J., Bastow, I. D., Keir, D., ... & Wright, T. J. (2013). Mantle upwelling and initiation of rift segmentation beneath the Afar Depression. *Geology*, 41(6), 635-638.
- Hammond, W. C., & Humphreys, E. D. (2000). Upper mantle seismic wave velocity: Effects of realistic partial melt geometries. *Journal of Geophysical Research: Solid Earth*, 105(B5), 10975-10986.
- Hansen, S. E., Nyblade, A. A., & Benoit, M. H. (2012). Mantle structure beneath Africa and Arabia from adaptively parameterized P-wave tomography: Implications for the origin of Cenozoic Afro-Arabian tectonism. *Earth and Planetary Science Letters*, 319, 23-34.
- Hansen, S. E., Nyblade, A. A., & Julia, J. (2009). Estimates of crustal and lithospheric thickness in Sub-Saharan Africa from S-wave receiver functions. *South African Journal of Geology*, 112(3-4), 229-240.
- Herzberg, C., & Asimow, P. D. (2008). Petrology of some oceanic island basalts: PRIMELT2. XLS software for primary magma calculation. *Geochemistry, Geophysics, Geosystems*, 9(9).
- Herzberg, C., Asimow, P. D., Arndt, N., Niu, Y., Leshner, C. M., Fitton, J. G., ... & Saunders, A. D. (2007). Temperatures in ambient mantle and plumes: Constraints

- from basalts, picrites, and komatiites. *Geochemistry, Geophysics, Geosystems*, 8(2).
- Hofmann, C., Courtillot, V., Feraud, G., Rochette, P., Yirgu, G., Ketefo, E., & Pik, R. (1997). Timing of the Ethiopian flood basalt event and implications for plume birth and global change. *Nature*, 389(6653), 838-841.
- Holtzman, B. K. (2016). Questions on the existence, persistence, and mechanical effects of a very small melt fraction in the asthenosphere. *Geochemistry, Geophysics, Geosystems*, 17(2), 470-484.
- Hopper, E., Gaherty, J. B., Shillington, D. J., Accardo, N. J., Nyblade, A. A., Holtzman, B. K., ... & Mbogoni, G. (2020). Preferential localized thinning of lithospheric mantle in the melt-poor Malawi Rift. *Nature Geoscience*, 13(8), 584-589.
- Jakovlev, A., Rumpker, G., Schmeling, H., Koulakov, I., Lindenfeld, M., & Wallner, H. (2013). Seismic images of magmatic rifting beneath the western branch of the East African rift. *Geochemistry, Geophysics, Geosystems*, 14(11), 4906-4920.
- Karato, S. I. (1993). Importance of anelasticity in the interpretation of seismic tomography. *Geophysical research letters*, 20(15), 1623-1626.
- Karato, S. I., & Eiler, J. (2003). Mapping water content in upper mantle. *Geophysical Monograph-American Geophysical Union*, 138, 135-152.
- Katsura, T., Yoneda, A., Yamazaki, D., Yoshino, T., & Ito, E. (2010). Adiabatic temperature profile in the mantle. *Physics of the Earth and Planetary Interiors*, 183(1-2), 212-218.
- Kawakatsu, H., Kumar, P., Takei, Y., Shinohara, M., Kanazawa, T., Araki, E., & Suyehiro, K. (2009). Seismic evidence for sharp lithosphere-asthenosphere boundaries of oceanic plates. *science*, 324(5926), 499-502.
- Lavayssière, A., Rychert, C., Harmon, N., Keir, D., Hammond, J. O., Kendall, J. M., ... & Leroy, S. (2018). Imaging lithospheric discontinuities beneath the Northern East African Rift using S-to-P receiver functions. *Geochemistry, Geophysics, Geosystems*, 19(10), 4048-4062.
- Lee, C. T. A. (2003). Compositional variation of density and seismic velocities in natural peridotites at STP conditions: Implications for seismic imaging of compositional heterogeneities in the upper mantle. *Journal of Geophysical Research: Solid Earth*, 108(B9).
- Liu, L., Tong, S., Li, S., & Qaysi, S. (2020). Sp Receiver-Function Images of African and Arabian Lithosphere: Survey of Newly Available Broadband Data. *Seismological Research Letters*, 91(3), 1813-1819.

- Malinverno, A., & Briggs, V. A. (2004). Expanded uncertainty quantification in inverse problems: Hierarchical Bayes and empirical Bayes. *Geophysics*, 69(4), 1005-1016.
- Meghraoui, M., & IGCP-601 Working Group. (2016). The seismotectonic map of Africa. *Episodes Journal of International Geoscience*, 39(1), 9-18.
- Mulibo, G. D., & Nyblade, A. A. (2013). The P and S wave velocity structure of the mantle beneath eastern Africa and the African superplume anomaly. *Geochemistry, Geophysics, Geosystems*, 14(8), 2696-2715.
- Nelson, W. R., Furman, T., van Keken, P. E., Shirey, S. B., & Hanan, B. B. (2012). OsHf isotopic insight into mantle plume dynamics beneath the East African Rift System. *Chemical Geology*, 320, 66-79.
- O'Donnell, J. P., Adams, A., Nyblade, A. A., Mulibo, G. D., & Tugume, F. (2013). The uppermost mantle shear wave velocity structure of eastern Africa from Rayleigh wave tomography: Constraints on rift evolution. *Geophysical Journal International*, 194(2), 961-978.
- Ono, S. (2008). Experimental constraints on the temperature profile in the lower mantle. *Physics of the Earth and Planetary Interiors*, 170(3-4), 267-273.
- Reusch, A. M., Nyblade, A. A., Wiens, D. A., Shore, P. J., Ateba, B., Tabod, C. T., & Nnange, J. M. (2010). Upper mantle structure beneath Cameroon from body wave tomography and the origin of the Cameroon Volcanic Line. *Geochemistry, Geophysics, Geosystems*, 11(10).
- Ritsema, J., Deuss, A., Van Heijst, H. J., & Woodhouse, J. H. (2011). S4ORTS: a degree-40 shear-velocity model for the mantle from new Rayleigh wave dispersion, teleseismic traveltimes and normal-mode splitting function measurements. *Geophysical Journal International*, 184(3), 1223-1236.
- Ritsema, J., Heijst, H. J. V., & Woodhouse, J. H. (1999). Complex shear wave velocity structure imaged beneath Africa and Iceland. *Science*, 286(5446), 1925-1928.
- Ritsema, J., Ni, S., Helmberger, D. V., & Crotwell, H. P. (1998). Evidence for strong shear velocity reductions and velocity gradients in the lower mantle beneath Africa. *Geophysical Research Letters*, 25(23), 4245-4248.
- Rooney, T. O., Herzberg, C., & Bastow, I. D. (2012). Elevated mantle temperature beneath East Africa. *Geology*, 40(1), 27-30.
- Rychert, C. A., Rondenay, S., & Fischer, K. M. (2007). P-to-S and S-to-P imaging of a sharp lithosphere-asthenosphere boundary beneath eastern North America. *Journal of Geophysical Research: Solid Earth*, 112(B8).
- Schilling, J. G., Kingsley, R. H., Hanan, B. B., & McCully, B. L. (1992). Nd-Sr-Pb isotopic variations along the Gulf of Aden: Evidence for Afar mantle

- plume-continental lithosphere interaction. *Journal of Geophysical Research: Solid Earth*, 97(B7), 10927-10966.
- Simmons, N. A., Forte, A. M., Boschi, L., & Grand, S. P. (2010). GyPSuM: A joint tomographic model of mantle density and seismic wave speeds. *Journal of Geophysical Research: Solid Earth*, 115(B12).
- Simmons, N. A., Myers, S. C., Johannesson, G., & Matzel, E. (2012). LLNL-G3Dv3: Global P wave tomography model for improved regional and teleseismic travel time prediction. *Journal of Geophysical Research: Solid Earth*, 117(B10).
- Takei, Y. (2002). Effect of pore geometry on VP/VS: From equilibrium geometry to crack. *Journal of Geophysical Research: Solid Earth*, 107(B2), ECV-6.
- Takei, Y. (2017). Effects of partial melting on seismic velocity and attenuation: A new insight from experiments. *Annual Review of Earth and Planetary Sciences*, 45, 447-470.
- Takei, Y., & Holtzman, B. K. (2009). Viscous constitutive relations of solid-liquid composites in terms of grain boundary contiguity: 1. Grain boundary diffusion control model. *Journal of Geophysical Research: Solid Earth*, 114(B6).
- Venkataraman, A., Nyblade, A. A., & Ritsema, J. (2004). Upper mantle Q and thermal structure beneath Tanzania, East Africa from teleseismic P wave spectra. *Geophysical research letters*, 31(15).
- Weeraratne, D. S., Forsyth, D. W., Fischer, K. M., & Nyblade, A. A. (2003). Evidence for an upper mantle plume beneath the Tanzanian craton from Rayleigh wave tomography. *Journal of Geophysical Research: Solid Earth*, 108(B9).
- Wittlinger, G., & Farra, V. (2007). Converted waves reveal a thick and layered tectosphere beneath the Kalahari super-craton. *Earth and Planetary Science Letters*, 254(3-4), 404-415.
- Wolfenden, E., Ebinger, C., Yirgu, G., Deino, A., & Ayalew, D. (2004). Evolution of the northern Main Ethiopian rift: birth of a triple junction. *Earth and Planetary Science Letters*, 224(1-2), 213-228.
- Yamauchi, H., & Takei, Y. (2016). Polycrystal anelasticity at near-solidus temperatures. *Journal of Geophysical Research: Solid Earth*, 121(11), 7790-7820.
- Zhu, Z., Bezada, M. J., Byrnes, J. S., & Ford, H. A. (2021). Evidence for Stress Localization Caused by Lithospheric Heterogeneity From Seismic Attenuation. *Geochemistry, Geophysics, Geosystems*, 22(11), e2021GC009987.

Using Introductory Level Geoscience Instruction to Analyze the Face of Geology through 3D Visualization

Gillian Goldhagen¹, Heather A. Ford¹ and Kinnari Atit²

¹Dept. of Earth and Planetary Sciences, University of California – Riverside, Riverside,
CA, USA.

²Graduate School of Education, University of California – Riverside, Riverside, CA,
USA

ABSTRACT

Three-dimensional (3D) visualization skills are the ability to visualize and mentally manipulate 3D objects, a skill used often within geosciences. Despite the importance of 3D visualization skills to achieving success in beginner-level geoscience courses (Kali & Orion, 1996; Piburn et al., 2002; Titus & Horsman, 2009), large gaps in our understanding of best spatial pedagogy exist. The objective of this study was to explore how variations in application of introductory geoscience pedagogy can foster the development of beginner-level students' 3D visualization skills. We test the following four hypotheses: (1) students' demographics play a role in initial 3D visualization skills; (2) learning environment can influence the development of 3D visualization skills; (3) learning method can influence the development of 3D visualization skills; (4) students' 3D visualization skills will predict their performance on a domain-specific geoscience midterm. To test these hypotheses, we randomly assigned students to an online or in-person classroom where they were taught geoscience concepts via 2D homework review, 3D static models, or 3D dynamic demonstrations. Students had to complete a spatial understanding test before and after 5 weeks of treatment. We found that males outperformed females' scores on the tests of 3D visualization while the rate of improved spatial skills did not statistically differ by gender. Our research found null results for three of our hypotheses which paves the way for future research.

OVERVIEW & OBJECTIVES

Three-dimensional (3D) visualization skills - visualizing and reasoning about three-dimensional (3D) objects are some of the critical factors for success in geosciences (Kali and Orion, 1996; Piburn et al., 2002; Titus and Horsman, 2009). Structural geologists utilize 3D visualization skills when trying to imagine the interior of a 3D object, such as a geologic structure, from what can be seen on its surface – a task called penetrative thinking. Petroleum geologists use 3D visualization skills to pinpoint the location of oil well underground. Similarly, mineralogists use 3D visualization skills when identifying minerals based on their geometric properties. Despite the centrality of this skill, research indicates that novices to the geosciences find completing geologic tasks involving 3D visualization difficult (Alles and Riggs, 2011; Atit et al., 2015; Kali and Orion, 1996). Research from spatial cognition suggests that individuals from specific demographics can disproportionately struggle with completing spatial tasks involving 3D Visualization (Miller and Halpern, 2013). The means of improving these students' 3D visualization skills through geologic instruction are not yet fully understood. Since geosciences have the lowest racial, ethnic, and gender diversity of all STEM domains across all higher education levels (Huntoon et al., 2015), understanding how to bolster students' 3D visualization skills is critical to broadening participation and facilitate student retention in the discipline.

This study aimed to examine how introductory geoscience pedagogy can support the development of novice students' 3D visualization skills. This study tests four central

hypotheses: (1) the students' demographics, (2) the learning environment, (3) the learning method that can influence a students' 3D visualization, and (4) improve 3D visualization and can predict students' grasp of beginner-level domain-specific knowledge. These hypotheses were formulated after observing anecdotal evidence of students struggling to grasp 3D beginner-level geologic concepts such as horizontal and vertical movement on a fault plane. Those students who could better visualize the concepts in a 3D space seemed to grasp these domain concepts better, a theory supported by prior studies on novices in STEM (Alles and Riggs, 2011; Atit et al., 2015; Kali and Orion, 1996). By performing this research, we aimed to investigate the best practices for improving teaching methods so that having inadequate 3D visualization skills does not prevent students from going further into the geoscience field. We can accomplish this by studying the importance of 3D visualization and researching better pedagogy to adequately foster these skills from a domain-specific perspective both within this study and in future studies.

More than a third of all students take at least one online course during their post-secondary education (Ginder et al., 2019). This study compares instructional methods in two learning environments, online and in-classroom. Prior research focuses on the benefit of online learning on 3D visualization skills. As understanding many fundamental introductory geologic concepts relies on extracting dynamic information represented in static formats (Kali and Orion, 1996; Kastens et al., 2016), we compared the effectiveness of static visuals (3D models) versus dynamic visuals (3D demonstrations), on the development of students' 3D visualization skills. No prior studies currently exist that examine causal relationships between these factors. To further understand how to

facilitate the best learning in students underrepresented in the discipline, we investigated whether the effectiveness of the visuals and the learning environment differed depending on student race/ethnicity and gender. Finally, to establish whether domain-general 3D visualization affects students' grasp of the domain-specific 3D concepts given in the course, we tested to see if improvement of 3D visualization can predict comprehension of the geoscience material provided during the midterm. Our working hypothesis was that students with higher 3D visualization gains would perform better in the class.

Our findings aim to find ways to teach students of under-represented demographics better to allow more students to join professional STEM careers. By studying learning environments, we can research the influence of 3D visualization on online classrooms, which make subjects more accessible to students. Our study of learning methods can inform pedagogical practices of the best methods to teach dynamic and static 3D concepts on typically dynamic topics. By analyzing 3D visualization improvement as a predictor of domain-specific knowledge, we can further categorize the importance of 3D visualization in STEM. By identifying pedagogical practices that are more effective for 3D concepts, we can find better ways to teach more students, which can help diversify the STEM field.

BACKGROUND

3D Visualization in the Geosciences

Spatial skills are cognitive skills used to manipulate, organize, reason about, and make sense of spatial relationships in real and imagined spaces (Atit et al., 2020). They are

used in generating, retaining, retrieving, and transforming well-structured visual images (Lohman, 1994). Much of what we know about spatial skills today comes from psychological research conducted to understand 2D transformation and 3D visualization skills (Linn and Petersen, 1985; McGee, 1979). Three-dimensional visualization is an ordinary spatial skill used in geosciences to make sense of 3D information. For example, envisioning the topography represented on a topographic map utilizes 3D visualization skills (Atit et al., 2016; Liben and Titus, 2012).

Additionally, structural geologists use 3D visualization when observing outcrops to determine information about the 3D geometry and geologic history of the geologic structure of interest (Atit et al., 2020). The tasks used in spatial cognition research (Bennett et al., 1947; Guay, 1977) measure isolated spatial skills independent of context and have been suggested to provide the foundation for field-specific spatial thinking required by STEM experts (Uttal and Cohen, 2012). These domain-general spatial skills require no outside subject knowledge (Atit et al., 2020). Alternatively, domain-specific spatial thinking involves the use of external expertise. A structural geologist uses domain-specific spatial thinking when using prior knowledge about the kinds of geologic structures that exist in the environment to deduce the 3D shape of existing structures from surface features.

A review of the research on spatial skills and STEM learning indicates that domain-general spatial skills, such as domain-general 3D visualization skills, are fundamental for introductory STEM learning and perhaps serve as a gatekeeper to pursuing STEM coursework (Uttal and Cohen 2012). Students take introductory geoscience classes. They

often need to use their domain-general 3D visualization skills to understand domain-specific spatial concepts taught in the classroom. Three-dimensional visualization skills significantly predict the knowledge students retain after their geoscience course (Piburn et al. 2002). In addition, 3D visualization and prior knowledge were equally predictive of post-test knowledge scores. However, research has revealed that novices find learning and mastering topics involving 3D visualization difficult (Gagnier and Shipley, 2016; Rapp, 2005). If students enroll in introductory STEM courses with soft domain-general spatial skills, they can inhibit their learning from understanding and reasoning about domain-specific concepts (Uttal and Cohen 2012).

Further research confirms the importance of 3D visualization in learning geosciences and underlines the importance of understanding ways to improve 3D visualization. Constantly improving and practicing domain-general 3D visualization skills can influence students' domain-specific 3D visualization skills (Piburn et al., 2002; Sorby, 2007). Furthermore, studies reveal that learning the geoscience domain has boosted students' 3D visualization skills. Piburn et al. (2002) observed that domain-general 3D visualization could improve through domain-specific spatial instruction and increase geoscience learning in novices. Additionally, Ormand et al. (2017) found that taking geoscience classes and engaging in geoscience tasks boost domain-general 3D visualization skills. Building on prior research demonstrating that learning and engaging in geoscience coursework improves domain-general 3D visualization skills (Ormand et al., 2017; Piburn et al., 2002), this project aims to find specific areas types of pedagogy that support the development of students' domain-general 3D visualization skills.

Pedagogy

Static vs. Dynamic

When geologists study geologic history, they must visualize the dynamic movements of static geologic structures. Correctly understanding this movement requires visualizing how the presently static object moved and transformed into its current form. Expert geologists use 3D visualization skills when interpreting diagrams, outcrops, and topography (all types of static information) to infer the movements to create the current formation. Novices commonly struggle to figure out dynamic movement from stationary data (Atit et al., 2014, 2020; Kastens et al., 2016; Shipley and Tikoff, 2016). Some research on novices suggests that domain-general 3D visualization skills are used to reason about dynamic information represented in static domain-specific diagrams (Kastens et al., 2016; Ormand et al., 2014). With students struggling to see the process behind static visualizations, teaching with dynamic visualizations (e.g., 3D demonstrations) could influence student learning.

Our study will compare the effects of static versus dynamic instruction on the development of novice students' domain-general 3D visualization skills. Static instruction will be provided using 3D models, and dynamic instruction will be provided with 3D demonstrations. Prior research comparing the effects of static versus dynamic instruction on student learning has primarily been focused on students' motivation and acquisition of the content. Barak and Dori (2011) found increased elementary student motivation when using computerized animation in the science classroom compared to students learning through still pictures. Additionally, Höffler and Leutner (2007)

performed a meta-analysis on dynamic versus static teaching methods for various studies on most STEM topics. They found an advantage in non-interactive animations over static pictures. These studies indicate that dynamic methods can improve student performance in their respective disciplines. However, these studies do not examine the effect of instructional type on students' 3D visualization skills.

Research that has considered 3D visualization when comparing the effects of dynamic versus static instruction on student learning has focused on the role of students' pre-instruction (i.e., baseline) 3D visualization spatial skills. Students with more vital baseline 3D visualization skills have been found to benefit more from animations in classrooms than students with weaker baseline 3D visualization skills (Mayer and Sims, 1994; Mayer et al., 1996; Yang et al., 2003). Similar results were found when comparing 3D and 2D static instructional methods. In students with lower baseline 3D visualization skills, the effect of presenting 3D static computer models of cells as 2D images overwhelmed students (Huk, 2006). These studies underline the importance of 3D visualization skills needed to learn from various visual instruction, emphasizing that certain kinds of instruction may require different levels of 3D visualization skills to be effective. With each study observing different types of 3D, 2D, dynamic, and static learning methods, often without regard to the learning environment and varying treatment time, it is hard to draw adequate conclusions from prior work. Thus, the study proposed here will compare the effects of 20-minute instructional sessions that use static 3D models or dynamic 3D demonstrations on the development of students' domain-general 3D visualization skills and their geologic content understanding. To understand the effect

of each instructional type, we will also include a control group that will complete standard written homework problems during their instructional time. The control group will receive no instruction using 3D static or dynamic visualizations.

Online vs. In-Person

Data indicates that approximately a third of all students in post-secondary institutions took at least one online course during 2017. One-tenth of those students were enrolled exclusively in online classes (Ginder et al., 2019). Online class enrollment has increased since 2009 at times, even as regular enrollment has decreased (Allen and Seaman, 2017). Online pedagogy has become more prevalent with the implementation of more online, hybrid, and flipped classrooms (Casselman et al., 2019). This shift towards online curriculum and resources can prove beneficial for online and in-person classroom environments when teaching subject matter that is hard to replicate or quantify appropriately in a classroom setting. Online animations can help to show the passage of geologic time or the particle movement of a waveform. Google Earth can bring mountain ranges and geologic features into the classroom. The prevalence and importance of online pedagogy make it necessary to understand how these resources compare to in-person instruction in influencing student learning.

When comparing the differences between learning environments on student learning, studies have found varying results in classroom performance. For an introductory mineralogy course, Feig et al. (2010) studied the differences between cyberlearning and face-to-face classes. The study found no statistical difference between the students' performance in each category. Klippel et al. (2019) studied virtual field trips and found

increased lab grades from the students using the technology over normal field trips. This disparity in results could be due to the wide range of online technology, where some prove more effective than others. These studies did not study 3D visualization, only classroom performance. To underline the importance of 3D visualization in online classrooms, Keehner et al. (2004) suggest that 3D visualization skills are necessary to comprehend 3D computer visuals.

Furthermore, research has demonstrated that 3D visualization skills can be taught through a computer screen (Güven and Kosa, 2008; Kali et al., 1997). Three-dimensional visualization skills can be influenced by online learning. However, these studies do not compare 3D visualization in online classrooms with the influence of a traditional in-person classroom. Prior work on using online learning tools in an in-person classroom was done by Piburn et al. (2005), who studied the influence of online technology on students' 3D visualization skills during regular in-person class time. They found that while both experimental and control classes improved, the practical class, which used two more computer modules than the control class, resulted in a higher increase in students' 3D visualization skills. However, prior research does not clarify whether improving domain-general 3D visualization skills differs depending on the learning environment (i.e., online vs. in-person). With the increase of online learning at the undergraduate level (Ginder et al., 2019), there is a critical need to fill this lack of prior research. This study aims to compare online and in-person learning environments and understand what classroom environments facilitate the development of students' 3D visualization skills.

Demographics

Geoscience is one of the least diverse STEM fields in the U.S. (Stokes et al., 2015). Literature indicates that 3D visualization skills are essential for geoscience learning (Kali and Orion, 1996; Piburn et al., 2002; Titus and Horsman, 2009). In addition, past research shows that pedagogy can improve students' 3D visualization skills (Ormand et al., 2017; Piburn et al., 2002). Hence, it is essential to consider who the pedagogy is helping broaden participation and increase the diversity in the earth sciences. In this study, students' demographics, in conjunction with their 3D visualization skills, will be examined to understand better the baseline skills they possess and the most effective pedagogy in facilitating their spatial skill development.

Gender

In the STEM fields, there are often more males than females. This discrepancy exists in college STEM majors and STEM jobs (Beede et al., 2011; Hango, 2013). While slight progress has been made in recent years, only 41% of undergraduate geoscience degrees are awarded to women (Holmes and O'Connell, 2003; NRC, 2013). Women in the workforce hold 30% of total geoscience jobs (NRC, 2013) while making up 50% of the population (Ritchie and Roser, 2019). A similar gender discrepancy may exist in 3D visualization skills, although prior research has often yielded conflicting conclusions. Some studies of 3D visualization skills have found gender disparities where males performed better than their female counterparts (Gardner, 2010; Jirout and Newcombe, 2015; Sorby, 2006; Sorby, 2007; Sorby, 2009). Other studies have found no difference between the genders (e.g., Koch, 2006; Kolb and Waishaw, 2014; Titze, 2008). Two

studies found that women showed higher gains in 3D visualization skills than men after spatial training (Cherney et al., 2014, Šafhalter, 2015). These differences have led to a stereotype that men have better 3D visualization skills than women, although this may be a misconception tied to the nature of the cognitive tasks performed (Miller and Halpern, 2014). Mental rotation tasks, a type of task involving 3D visualization skills, have the highest male advantage over women. This difference gets further pronounced when involving 3D objects or time limits (Voyer et al., 1995, Voyer, 2011). This gender gap could exist due to the following: 1) difference in exposure to “female” versus “male” toys (Newcombe et al., 1983; Serbin and Connor, 1979), where playing with traditionally male toys (e.g., blocks) requires the use of more 3D visualization skills; 2) psychosocial conditioning from gender stereotypes (Neuburger et al., 2015), where stereotypes can have psychological effects on performance; 3) or hormones (Constantinescu et al., 2018), where sex hormones affect brain development and function (Lauer et al., 2019). Based on prior findings, we expect to find gender differences in students' 3D visualization skills and their geoscience content understanding for topics requiring 3D visualization skills.

Diversity

About 37% of college students are underrepresented minorities (URM). Of students attending 4-year colleges, around 22% are URM (Ginder et al., 2019). Despite progress, fewer than 7% of undergraduate STEM degrees are awarded to URM (NSF, 2013). This lack of diversity has a ripple effect where without a diverse undergraduate population, you cannot expect various employment (Chan, 2013). Today the STEM workforce is no more varied than ten years ago (Bidwell, 2015). Less than 15% of STEM positions are

held by people from African American and Latino backgrounds (Landivar, 2013). Adding more diversity to the workforce has several benefits, such as alleviating the gap between the number of students pursuing STEM careers and the number of professionals needed to meet future demands. Diversity can also improve creativity, innovation, and STEM product and service quality (Burke and Mattis, 2007). Identifying explanations for this low diversity is the first step in developing a more diverse field. Previous studies have found connections between low diversity levels in geoscience and lack of mentors, subtle biases, discrimination, cultural disconnects, and lack of familial support (Holmes and O'Connell, 2003; Holmes et al., 2008; NRC, 2013; Stokes et al., 2015).

3D visualization skills have mainly been an unexplored factor contributing to the lack of diversity in the geosciences despite the understanding that they can act as a gatekeeper to STEM success and retention (Uttal et al., 2012). Previous research has found connections between socioeconomic status (SES) levels and 3D visualization skills (Jirout and Newcombe, 2015; Levine et al., 2005; 2012), which can be loosely connected to diversity. SES and race are linked in America, with minorities accumulating significantly less wealth than white households (Campbell and Kaufman, 2006; NSB, 2014). Research indicates that an explanation for differences in spatial skill development between genders and students from different SES backgrounds can be tied to experiences engaging in activities utilizing 3D visualization skills such as spatial play involving blocks, puzzles, and video games (Casey et al., 2008; Jirout and Newcombe, 2015; Subrahmanyam and Greenfield, 1994). Because race and SES are often conflated, similar differences in spatial play experiences may exist between races due to cultural influence or the

connection between SES and race in America. Outside of play, which is often dictated by circumstances at home, only a handful of instances during formal learning experiences have systematically focused on developing students' 3D visualization skills (Lowrie et al., 2019; Sorby, 2007). This can lead to university students enrolling in introductory geoscience classes possibly unfamiliar with utilizing 3D visualization skills developed through informal experiences, resulting in students finding it difficult to reason about the complex spatial problems required to comprehend geoscience. Understanding how to help students leverage their 3D visualization skills may help improve URM student outcomes. Due to the critical need to increase diversity in the geosciences, this study will examine the demographic make-up of participating students to explore possible ways to remove 3D visualization skills as a barrier to success.

METHOD

Participants

This study took place in an introductory Natural Hazards and Disasters, undergraduate geoscience class during the winter quarter of 2020. The class consisted of 440 students and is considered a beginner-level geoscience class at a majority-minority institution. The schedule of the class and the study itself is included in figure 3.1.

This study includes all consenting students enrolled in Geo 004 for the winter 2020 quarter. Since this research is dependent on human participants, the methods have been reviewed and approved by the Institutional Review Board at UC Riverside to ensure ethical practice. All enrolled students were selected for this study; results were discarded from students who opted out of the study.

To ensure that our sample size was adequate, we performed an a priori power analysis using G*Power3 (Faul et al., 2007) to estimate the acceptable sample size to conduct a multiple regression with ten predictors and yield a power of .80 at a medium effect size ($F = 0.15$). The power analysis indicated that a sample size of 118 participants would be required for this study. With eight demographic factors and two treatment factors, our sample size is sufficient at 181 students.

Measures

Attendance

We tested four different treatments: online learning with 3D models, online learning with 3D demonstrations, in-person learning with 3D models, and in-person learning with 3D demonstrations. To evaluate and compare the efficacy of each of the treatment type instructions, two control conditions were also included, the online homework review and in-person homework review conditions. Their teaching assistants tracked student attendance to their weekly discussion, and only those students with full attendance were included in the study.

Demographic survey:

The demographic survey asked about age, gender, race/ethnicity, number of science classes taken, first-generation student status, major, cohort, and GPA. The complete demographic survey has been attached in Appendix B.

3D Visualization Test

The 3D visualization test used in the study was Guay's Visualization of Views test (Guay and McDaniels, 1976). For this study, the trial, initially 24-items, was split into two

assessments containing 12 items each. One assessment was administered pre-treatment, and the other assessment was administered post-treatment. Participants had 8 minutes to complete each 12-item assessment. For each question, participants were shown a figure “hovering in the middle” of a cube and then a second image of the exact figure shown from a different perspective, the target figure. For each item, the task was to identify the corner of the cube that would show the figure from the same perspective as the target figure. Figure 3.2 is an image of an example question from the test. The tests were scored by giving 1 point for each correct item subtracting one for each incorrect item divided by six to account for guessing.

Midterm

An additional assessment included in our study was students’ midterm performance. Midterm exams were completed in week 5 of the quarter and had 50 items. The instructor of the course created the midterm. Performance on the test was used to gauge students’ understanding of domain-specific 3D visualization skills. The midterm included questions requiring some 3D visualization skills and domain knowledge. For example, topics involving 3D visualization that will be assessed in the midterm include understanding a topographic map, finding slope, relating explosivity to volcano shape, and fault identification. Students’ midterm scores were the sum of the number of items answered correctly. The overall score on the midterm was recorded.

PROCEDURE

Students were randomly assigned to one of the following six conditions: online classroom with 3D demonstrations, online classroom with 3D models, online classroom with

homework review, in-person classroom with 3D demonstrations, in-person classroom with 3D models, in-person classroom with homework review. Homework review classes reviewed the 2D homework assignments original to the course. Instructional material is reviewed in the following section. Participants in all conditions completed the following measures: Pre-study visualization test, post-study visualization test, the demographic questionnaire, and a subject specific midterm. Students completed the demographic survey and the Visualization of Views pretest in the first week of the quarter. The Visualization of Views and midterm was achieved during the fifth week of the quarter. Though the academic quarter is ten weeks long, the study was concluded after the midterm exam was administered.

INSTRUCTIONAL MATERIALS

Students participating in both learning environments were exposed to homework reviews, 3D demonstrations, or 3D models. All class discussions went over the same concepts to ensure that students learned the same points despite varied instructional materials.

Demonstrations

Students participating in the 3D demonstration treatment were taught either online or in person. Students passively watched as their TA performed a task demonstrating a 3D, dynamic concept. Their TAs performed a topography demonstration, a volcano demonstration, and a fault and plate boundary demonstration for the three treatment classes.

The topography demonstration consisted of a TA making a topographic map of a clay mountain by cutting and tracing individual clay segments. The mountain was segmented

with different topographic lines and cut into sections. The separate layers of clay were each separately traced onto a paper, demonstrating the creation of a topographic map. Students were then tasked with finding the slope on the newly made topographic maps step-by-step. Students participating online watched the TA make a topographic map through a *top trace* on *app.visblegeology.com* and then found the slope on the topographic map generated. Figure 3.3 shows pictures of both dynamic topography lessons.

The volcano demo involved students watching as TAs formed volcanic mountains from materials of different viscosity (e.g., icing and chocolate sauce). They then compare slopes, thickness, and explosivity. Students participating online will observe videos of this demo. The icing has a higher viscosity, forming volcanoes with steeper slopes and more explosive eruptions as the air gets trapped. Chocolate sauce flowed more easily, forming gentle slopes with less violent outbursts.

The fault and plate boundary demo involved the TAs showing a crosscut of a cardboard subduction zone. Students viewed earthquakes forming as a subducting plate was pushed into a convergent boundary. This taught students the geometry of these boundaries and how they result in different depth earthquakes, and the difference between epicenter and hypocenter. The TA then demonstrated a reverse fault forming using sand in a fault deformation machine. The deformation machine is a wood and plexiglass box with one wall pushing into a layer of multi-color sand. This demonstrates a tectonic force contributing to the formation of faults over time. Students in the online condition will see videos of the same demonstrations and engage in similar discussions.

Models

Students being taught through 3D models also had online and in-person counterparts. Students passively observed static 3D models associated with topography, volcanoes, faults, and plate boundaries for the three treatment classes.

Students with in-person conditions observed a topographic map and its associated 3D clay mountain as they found the slope between two points on the hill during the topography class. Students learning with online model conditions observed 3D topographic maps on *app.visiblegeology.com* and found the slope on one of the presets available. Both groups followed a topographic map, the 3D shape of the map depicted, and then went through the steps to find the slope.

The volcano class involved students in the in-person model condition observing a 3D print of the volcano Mt. St. Helens and a 3D print of the island of Hawaii. They were then presented with a to-scale model of the volcano, Moana Loa, on the island of Hawaii to compare to the scaled model of Mt. St. Helen. Figure 3.4 shows both 3D prints side by side for size comparison. Students in the online condition observed both mountains through 3D renderings on Google Earth, where their TAs conducted a series of measurements on both volcanoes.

Students learned about faults and plate boundaries during the faults discussion 3d model class. The in-person model observed the cardboard subduction zone and fault deformation machine shown in the demonstration classes without movement. Students enrolled in the virtual classroom observed earthquakes at depth at the South American subduction zone using 3D imaging from the IRIS earthquake browser, navigated by their

TA. They then viewed a 3D rendering of a blind thrust fault, which the TAs navigated around in real time. The blind thrust fault model for both online and in-person conditions is shown in Figure 3.5.

RESULTS

All analyses were conducted using R version 4.1.1. Before analyzing our data to answer our research questions, preliminary analyses were conducted to identify relationships between variables and any pre-existing distinctions between conditions. Table 3.1 presents descriptive statistics for the pre and post 3D visualization tests, the midterm, and the difference between the post-test scores, labeled as Q. A graph comparing the means on the pre and post-tests for each of the six treatments is shown in Figure 3.6. Pearson's correlations between all measures and demographic variables were conducted (presented in Table 3.2). Following Cohen's conventions, results revealed that performance on the midterm had a strong positive correlation with students' reported GPA ($r = 0.44$, $p < 0.01$). Performance on the pre-test had a strong negative correlation with gender ($r = -0.31$, $p < 0.01$). Similarly, results on the post-test also showed a strong negative correlation with gender ($r = -0.33$, $p < 0.01$). Performance on the post-test was also strongly and positively correlated to pre-test performance ($r = 0.65$, $p < 0.01$). Difference in performance from pre to post-test was positively correlated with students' first-generation status ($r = 0.16$, $p < 0.01$), negatively correlated with their pretest performance ($r = -0.42$, $p < 0.01$), and positively correlated with their posttest performance ($r = 0.42$, $p < 0.01$). These results indicate that performance on the midterm is not correlated to the

students' 3D visualization skills and that gender is correlated to performance on 3D visualization tests.

Do student demographics predict baseline 3D visualization skills?

To find which demographics predict baseline 3D visualization, regression analyses were conducted to see if students' pre-test 3D visualization scores are associated with demographic variables. In this regression, Model 1, we controlled for gender, URM, first-generation status, age, and students reported GPA. Results of model 1, shown in Table 3.3, indicate that only gender is related to baseline 3D visualization scores (visualization pre-test score).

As gender differences are apparent on many visualization skill tests (Miller and Halpern, 2013), and as both pre-test and post-test visualization test score varied by gender in our study, a Welch's two sample *t*-test was conducted to compare the 3D visualization pre-test between males and females. This test was chosen due to the differences in sample sizes, with 58 male participants and 116 female participants, necessitating a non-parametric test (West, 2021).

Results, shown in table 3.5, indicate that there is a significant difference between the two groups on the pre-test, $t(93.5)=3.93$, $p<0.001$, with males ($M=6.65$, $SD= 4.06$) outperforming females ($M=4.25$, $SD=3.20$). This significant difference persists on the posttest with males again performing better ($M=7.12$, $SD= 4.18$) than females ($M=4.57$, $SD=3.14$), $t(90.1) = 4.11$, $p<0.001$. There was no significant difference in Q, which is the difference between the post-test and pre-test for each gender, $t(154.3)=0.35$, $p=0.73$, despite men ($M=0.47$, $SD=2.34$) numerically showing greater improvement than a

woman ($M=0.31$, $SD=3.37$). Thus, while males outperformed females on tests of visualization skills, how much students improved on the assessment did not differ by gender.

Does the learning environment influence the development of students' 3D visualization skills?

Regression analyses were conducted to see if students' assigned learning environment was associated with their post-study 3D visualization skills. To ensure that differences between conditions were not driven by differences in students' visualization skills at pre-test, we controlled for the pre-test score in this analysis. We also controlled gender here, and all subsequent analyses as correlational analyses indicate that students' performance on the Visualization of Views test varies by gender. Results for this regression, model 2, shown in table 3.3, indicate that after controlling for gender, the learning environment was not related to students' post-test scores.

Do Instructional methods influence the development of students' 3D visualization skills?

Regression analyses were conducted to see if students' learning methods are associated with their post-study 3D visualization skills. Like model 2, we controlled for the pre-test and gender in this analysis set. Results for this regression, model 3, shown in table 3.3, indicate that after controlling for gender, the instructional method did not significantly explain the post-test score.

Does Improvement in 3D visualization skills predict comprehension of geoscience midterm material?

Regression analyses were conducted to see if students' 3D visualization skills are linked with their midterm grades in their beginner-level geology course. We controlled for gender and reported GPA in the following regressions due to our correlation analysis indicating that midterm performance is dependent on GPA. We then analyzed if the pre-test, the difference in pre and post-test, or the pre-test when controlling for the environment and method influenced students' midterm scores. Model 4 shows that the reported GPA was the only variable significantly predicted midterm scores when controlling for the pre-test and both demographics. This was held in model 5 when we controlled for the difference between pre-test and post-test with demographics. In models 6, 7, and 8, we controlled for the environmental and method factors.

DISCUSSION

This study compared the 3D visualization skills of students before and after five weeks of an intro level geoscience natural hazards course after undergoing weekly in-person or online lessons utilizing 3D dynamic, 3D static, or 2D instructional pedagogy. The objective of this study was to find which factors acted as predictors of students' increased 3D visualization skills and overall course performance. Our study found that while males did better than females on the baseline 3D visualization skill test, no other demographics correlated with students' initial 3D visualization skills. Our research found null results when examining the influence of learning environment and learning methods about synchronous online or in-person learning and 3D dynamic demonstrations, 3D static

models, or 3D homework review utilized in the classroom. We similarly found no statistical influence related to students' 3D visualization on their comprehension of the geoscience midterm. Overall, our study suggests that outside of students' gender, their background, learning environment, and the learning methods we tested did not statistically influence students' spatial skills. Similarly, we found students' 3D visualization skills did not affect their performance on the domain-specific midterm. Much of the work done in this study was done to fill gaps in current research, so while many of our findings are null results, they are still the first to inform on these research questions and leave room for future work.

Consistent with prior research, our data shows that men outperformed women on 3D spatial skills (Jirout and Newcombe, 2015; Sorby et al., 2006; Sorby, 2007; Sorby, 2009; Cherney et al., 2014). Our study administered a test of perspective-taking, where students had to think about a 3D object from multiple perspectives to answer the spatial questions. Most research examining gender differences has been on mental rotation tests, where students must rotate an object in their head. While these two skills involve thinking about 3D information, prior research indicates that the two skills are distinct (Hegarty and Waller, 2004). Jirout and Newcombe (2015) used a WPPSI-IV test, while Sorby et al. (2006), Sorby (2007), and Sorby (2009) all used the PSVT test or some modified version of it, while Cherney et al., 2014 used the MRT test. The WPPSI-IV test looks at block design performance and does not typically have a gendered difference in performance (Voyer et al., 1995), unlike the PSVT and MRT test, which involves mental rotation. Perspective-taking has been found to have slight gender differences (Zancada-Menendez

et al., 2016; Stumpf, 1993). Titze (2008) found that removing time constraints on the MRT test can mitigate these gender differences.

Prior research has shown that engaging in STEM learning improves students' spatial skills (Piburn et al., 2005). Moreover, engaging with 3D perspectives of complex and straightforward geologic structures, such as those required in undergraduate earth science courses, can also mitigate the gender gap in spatial skills. In our study, student participation in an intro earth science course did not result in closing the gender gap. This could be due to the type of intervention. Piburn et al. (2005) used specific targeted 3D perspective representations within online lessons, while our study used less clear 3D imagery. Piburn et al. (2005) also used a geospatial test to test domain-specific improvement and the Surface Development test, involving folding a 2D shape into a 3D shape, as their 3D visualization test.

Our research found null results when we observed what demographics besides gender might influence baseline 3D visualization skills. This may be because other studies, such as Jirout and Newcombe 2015; Levine et al. 2005; 2012 found that SES levels can be connected to 3D spatial skills. These studies asked families to self-report their SES, and while our research asked students to self-identify race, we did not ask students specifically about their SES. While SES can be linked to diversity in the United States (Campbell and Kaufman, 2006; NSB, 2014), the link may not be strong enough to show results in our study. We found that first-generation students improved more in their spatial skills than multigenerational college students. More research can be done in the future to explore this link further.

Our study found that any increase in 3D visualization was not significantly linked to environmental factors. We know from past studies that online environments are no limitations to learning 3D spatial skills (Güven and Kosa, 2008; Kali et al., 1997). Piburn et al. (2005) found that online technology in the classroom during in-person lessons can increase 3D visualization skills. However, few studies have explored the difference between fully online lessons and entirely in-person lessons on developing 3D spatial skills. Our results show that once a week, an online lesson on the same topic had the same impact on 3D spatial skills as an in-person lesson. More work can be done to explore the effects of the amount of time in online lessons and the full impact of the covid classroom, which took place after this study had concluded.

Past studies have indicated that domain-specific spatial learning can increase spatial skills (Ormand et al., 2017; Piburn et al., 2002). These studies found that learning and engaging in geoscience classrooms can improve 3D spatial skills. Our results indicate that the instructional method, using a 3D dynamic demonstration, a 3D static model, or homework review did not significantly account for students' development of 3D visualization skills. Future research should identify what specific types of curricular activities bolster students' spatial skills.

Past studies have found that students with higher baseline 3D visualization skills benefit more from dynamic imagery used within the classroom (Mayer and Sims, 1994; Mayer et al., 1996; Yang et al., 2003). Huk 2006 found that similarly, only students with higher baseline 3D visualization benefited from the use of 3D static imagery over 2D static imagery. None of these studies observed the effect of different imagery on the

development of 3D visualization or compared 3D dynamic imagery with 3D static imagery and 2D static imagery. Our null result may result from lower initial 3D visualization skills acting as a barrier to Improvement or too little time devoted to each learning method. Future studies may further explore the instructional method's effect on 3D spatial skills since it is understood that specific curricula may require higher levels of 3D visualization skills.

Piburn et al. (2002) found that 3D visualization skills significantly predict the amount of domain-specific geoscience learned in their introductory-level geoscience course. This contradicts our results where we found higher 3D visualization skills did not boost performance on the course geoscience midterm. Piburn et al., 2002 used a geospatial test to gauge geoscience learning, while this study used the existing course midterm. Our results may differ because the midterm is used as an overall measure rather than parceling out the more spatial questions for a deeper comparison of spatial geoscience improvements. Within our study, the only predictor of higher performance in the midterm was reported GPA. Future research should examine the impact of spatial skills on student understanding of spatial vs. non-spatial geoscience concepts.

Limitations of this study include the circumstance of this study being a quasi-experimental design, taking place outside of a lab setting and inside a classroom environment. Due to the classroom environment, certain variables (e.g., self-selection into certain learning conditions and instructor bias) cannot be controlled. Therefore, these variables are acknowledged as a potential source of error in our results. We also had to work within the limitations of the course itself, only dedicating 20 minutes a week to

each treatment for five weeks. Future studies should further examine the effect of treatment time on students' 3D visualization skills. This study similarly had to account for attendance where only those students who attended all the classes were included in the analysis leading to further self-selection bias. It was beyond the scope of this study to account for test anxiety or performance on individual spatial questions within the midterm, instead only having access to overall scores. Future research should be conducted with a geospatial comparison to assess student learning and further analysis on levels of 3D visualization content within specific geoscience beginner-level courses.

CONCLUSION

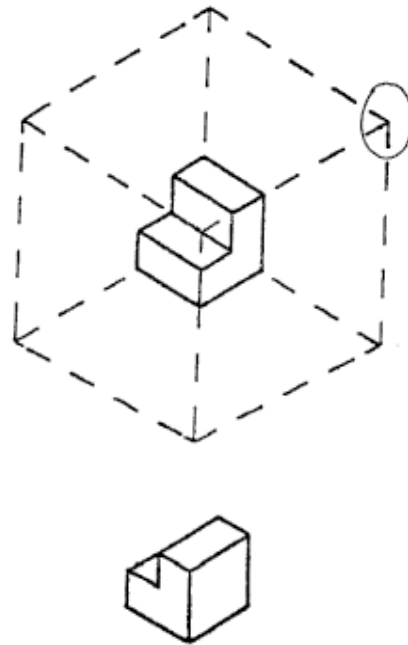
This study showed that gender differences in 3D visualization are a real problem. Engaging in spatial content may not be enough to close the gender gap by the end of a beginner-level college course. While this research set out to fill significant existing research gaps, we highlighted some key questions that still need to be explored. More research needs to be done on delivering content more effectively to students and what kind of content works for different students. This study helped find these research gaps and further highlight the amount we don't know about 3D visualization in the classroom.

Week Number	Tuesday Lecture	Wednesday Discussion	Thursday Lecture	Friday Discussion
1	Introduction	Introduction, pre-3D cognition test and demographic survey	Introduction to maps, topography	Introduction, pre-3D cognition test and demographic survey
2	Plate Tectonics	Topography discussion	Volcanoes part 1	Topography discussion
3	Volcanoes part 2	Volcanic discussion	Earthquakes	Volcanic discussion
4	Earthquakes	Fault and tectonics discussion	Climate and weather	Fault and tectonics discussion
5	Midterm 1	Post-study 3D cognition test and normal discussion resumes	Severe weather	Post-study 3D cognition test and normal discussion resumes
6	Severe weather		Wind and fire	
7	Wind and fire		Midterm 2	
8	floods		Floods and mass movements	
9	Mass movements		Coastal processes	
10	Tsunamis		California hazards and personal preparedness	

Figure 3.1 This is the 10 week curriculum topic schedule for the Geo 004 Natural Hazards Course, Winter 2020. Each week students have two lectures, labeled in white, and one hour of discussion class either Wednesday or Friday, labeled in green. Green discussion classes that are not labeled with a topic are outside of the scope of the study and will return to previous years course curriculum which consists of homework review.

Instruction for Guay's visualization of viewpoints

This test consists of 24 questions designed to see how well you can tell which viewing position a picture of a three-dimensional object was taken from. Shown below is an example of the type of question included in this test.



- The example shows an object HOVERING IN THE MIDDLE of a "glass box." Below it there is a picture of the same object from a new viewing position. You are to
1. look at the picture of the object taken from the new viewing position;
 2. imagine yourself moving around the "glass box" to find the corner from which this picture was taken
 3. circle that corner

What is the correct answer to the example?

The correct answer is the upper right corner. Only from there you would have the view that is depicted. Remember that each question has only one correct answer.

Figure 3.2 This figure is the first page of Guay's Visualization of Views 3D cognition test (Guay and McDaniels, 1976). Students were asked to answer twelve questions in four minutes for both pre- and post- treatment assessment. We followed Hegarty et al.'s (2009) scoring schema where students were given a point for the number of correct items, which was then subtracted by the number of incorrect items and divided by 6 (to account for guessing).

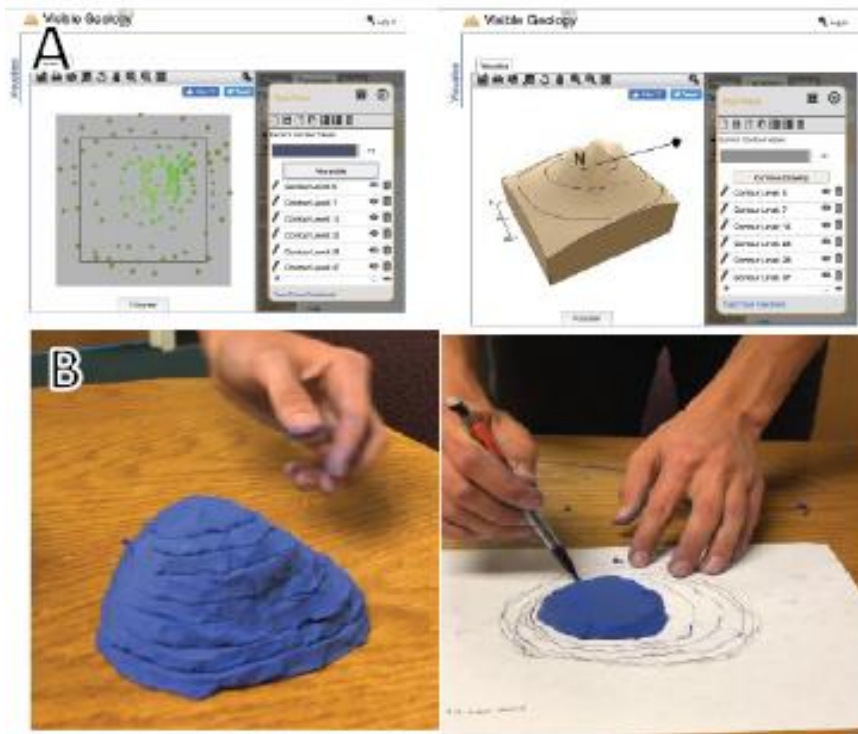


Figure 3.3 The top images A. are snapshots of topotrace on app.visiblegeology.com where TAs made their own 3D topographic maps as students observed during online demonstration based discussion class. The bottom image B. is the online demonstration class version where students watched a TA make a topographic map from a clay mountain.

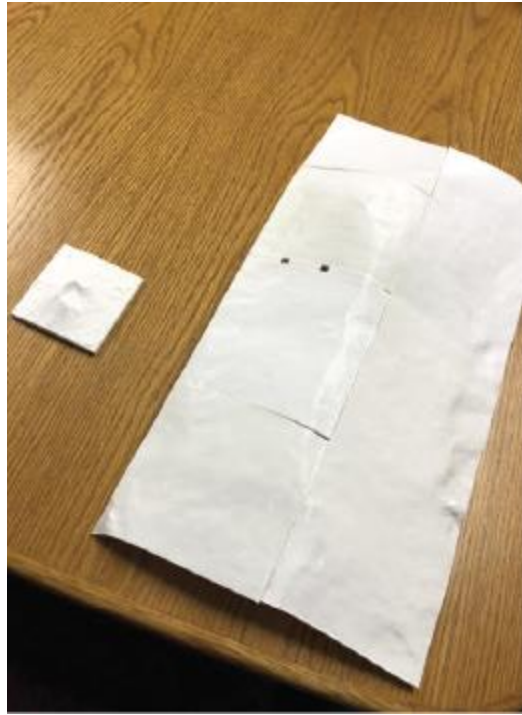


Figure 3.4 3D prints of Mount St. Helens and Mauna Loa (to scale) which were shown to students during in-person 3D model discussion classes. Students compared slope and size with volcano type.

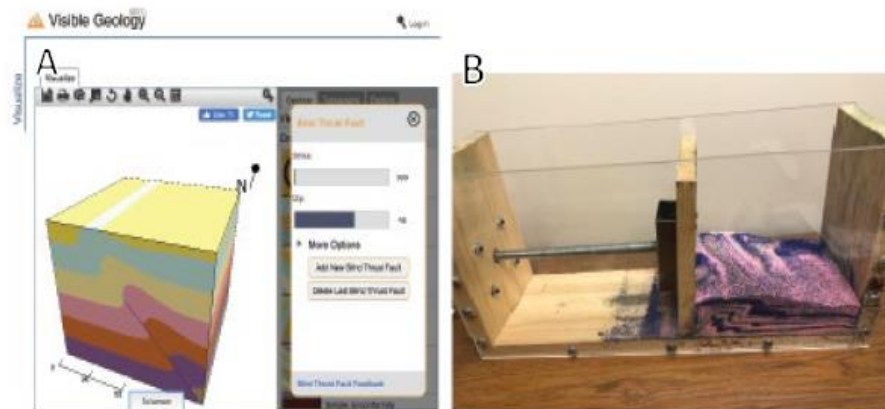


Figure 3.5 Subset A. is an image from app.visiblegeology.com showcasing a 3D model of a thrust fault. This was used during the 3D model online discussion classes. Subset B. Shows the 3D model of a thrust fault displayed for students in the in-person 3D model discussion classes.

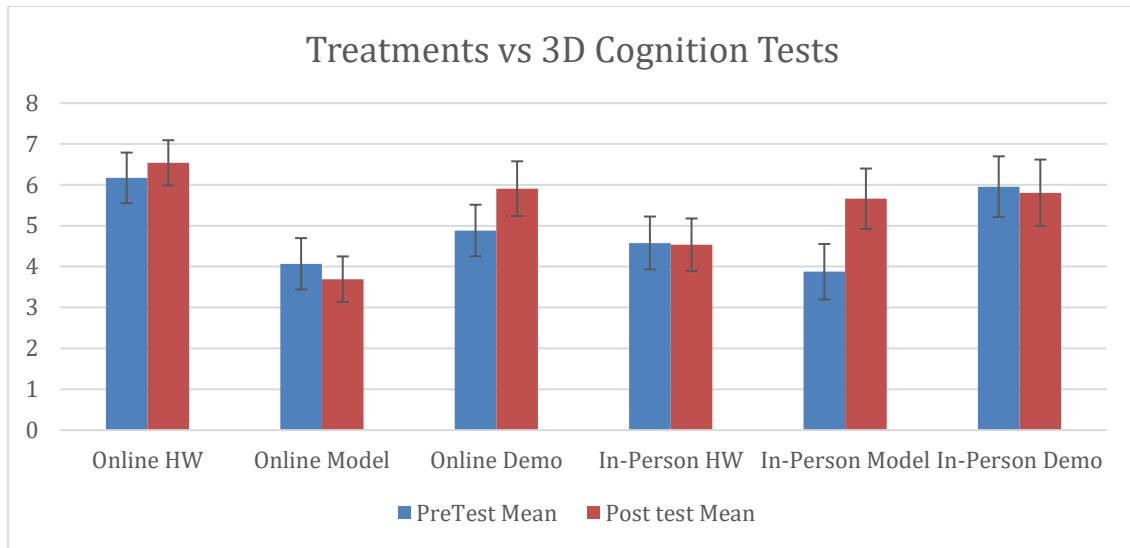


Figure 3.6 Pre and Post Treatment Average for each treatment type, this graph displays differences in pre and post 3D visualization mean scores for each treatment condition. Error bars denote the standard error.

Table 3.1 Descriptive of Data, this table displays the minimum, maximum, skewness, and kurtosis of the four assessments used in our study. Here we see no significant difference between pre and post 3D visualization assessments.

	PreTest	PostTest	Midterm	Q
Min	-2	-2	14	-8.167
Max	12	12	42	9.333
Skewness	0.1617351	0.1434233	-0.76675	0.0890853
Kurtosis	2.036132	2.111301	3.561262	3.40616

Table 3.2 Correlational Table, this table displays Pearson’s correlations between the 7 demographic factors and the 4 assessments. Correlations significant at the $p < 0.05$ level are indicated in bold font.

	1	2	3	4	5	6	7	8	9	10	11
1.First Gen	1										
2.Science Courses	-0.04	1									
3.Gender	0.13	0.14	1								
4.Year	0.08	0.13	-0.10	1							
5.URM	0.39	-0.17	0.12	0.10	1						
6.Reported GPA	-0.16	0.08	<i>0.15</i>	-0.21	-0.26	1					
7.Age	0.08	0.37	-0.05	0.58	0.01	-0.19	1				
8.PreTest	-0.08	0.09	-0.31	0.00	<i>-0.14</i>	-0.11	0.09	1			
9.PostTest	0.05	-0.01	-0.33	0.03	-0.05	-0.10	0.09	0.65	1		
10.Midterm	-0.08	0.10	-0.09	-0.05	-0.12	0.44	0.03	0.09	0.12	1	
11.Q	0.16	-0.13	-0.03	0.03	0.11	0.02	0.01	-0.42	0.42	0.04	1

Table 3.3 Linear regression model examining the relations between variables and pretest scores (model 1) or posttest score (model 2 and model 3), data is displayed showing coefficients, Significant codes: 0 ‘***’ 0.001 ‘**’ 0.01 ‘*’ 0.05 ‘.’ 0.1 ‘ ’ 1, and numbers in parenthesis are standard error.

	Model 1	Model 2	Model 3
Intercept	7.1911 . (3.7806)	2.96519 *** (0.57695)	2.84329 *** (0.59817)
PreTest		0.62065 *** (0.06041)	0.62181 *** (0.06037)
Q			
Environment		0.06211 (0.42281)	
Method			0.15134 (0.25406)
URM	-0.8520 (0.6269)		
Gender	-2.0675 *** (0.6104)	-1.06772 * (0.47007)	-1.05073 * (0.46975)
Reported GPA	-0.7138 (0.6972)		
FirstGen	-0.2349 (0.6287)		
Age	0.1088 (0.1291)		
R ²	0.08431	0.4388	0.4399

Table 3.4 Linear regression model examining the relations between variables and midterm scores, data is displayed showing coefficients, Significant codes: 0 ‘****’ 0.001 ‘***’ 0.01 ‘**’ 0.05 ‘.’ 0.1 ‘ ’ 1, and numbers in parenthesis are standard error

	Model 4	Model 5	Model 6	Model 7	Model 8
Intercept	14.5444 *** (3.0155)	15.636772 *** (2.893601)	14.5358 *** (3.0139)	14.3957 *** (3.0195)	14.3925 *** (3.0186)
PreTest	0.1304 (0.1067)		0.1317 (0.1067)	0.1373 (0.1069)	0.1383 (0.1069)
Q		0.006669 (0.125818)			
Environment			0.8158 (0.7545)		0.7925 (0.7551)
Method				0.4467 (0.4537)	0.4313 (0.4538)
Gender	-1.0756 (0.8337)	-1.350788 . (0.806520)	-1.0947 (0.8335)	-1.0098 (0.8365)	-1.0306 (0.8364)
Reported GPA	5.7322 *** (0.8898)	5.655166 *** (0.891854)	5.6176 *** (0.8956)	5.6343 *** (0.8954)	5.5264 *** (0.9010)
R ²	0.1974	0.1898	0.1983	0.1973	0.1978

Table 3.5 Results of t-tests examining differences between male and female students' 3D visualization skills and Cohen's D.

Measure	Male Mean (n = 58)	Female Mean (n=116)	95 percent confidence interval	t	p	Cohen's D
Pretest	6.652299	4.252874	(1.187751, 3.611100)	3.9321	0.0001615	0.656488
Posttest	7.120690	4.567529	(1.319262, 3.787060)	4.1107	8.685e-05	0.691123
Midterm	33.72414	32.68103	(-0.499486, 2.585693)	1.3367	0.1835	0.205716
Q	0.4683908	0.3146552	(-0.7122856, 1.0197569)	0.35068	0.7263	0.053029

REFERENCES

- Allen, E., and Seaman, J. (2017). Digital learning compass: Distance education enrollment report 2017
- Alles, M., and Riggs, E. M. (2011). Developing a process model for visual penetrative ability. *Geological Society of America Special Papers*, 474, 63-80.
- Atit, K. R., Uttal, D., and Stieff, M. (2020). Situating Space: Using a Discipline-Focused Lens to Examine Spatial Thinking Skills.
- Atit, K., Gagnier, K., and Shipley, T. F. (2015). Student gestures aid penetrative thinking. *Journal of Geoscience Education*, 63(1), 66-72.
- Atit, K., Shipley, T. F., & Tikoff, B. (2014). What do a geologist's hands tell you? A framework for classifying spatial gestures in science education. *Space in mind: Concepts for spatial learning and education*, 173.
- Atit, K., Weisberg, S. M., Newcombe, N. S., and Shipley, T. F. (2016). Learning to interpret topographic maps: Understanding layered spatial information. *Cognitive Research: Principles and Implications*, 1(1), 1-18.
- Baker, E. H. (2014). Socioeconomic status, definition. *The Wiley Blackwell Encyclopedia of health, illness, behavior, and society*, 2210-2214.
- Barak, M., and Dori, Y. J. (2011). Science education in primary schools: Is an animation worth a thousand pictures?. *Journal of Science Education and Technology*, 20(5), 608.
- Barak, M., and Hussein-Farraj, R. (2013). Integrating model-based learning and animations for enhancing students' understanding of proteins structure and function. *Research in Science Education*, 43(2), 619-636.
- Beede, D. N., Julian, T. A., Langdon, D., McKittrick, G., Khan, B., and Doms, M. E. (2011). Women in STEM: A gender gap to innovation. *Economics and Statistics Administration Issue Brief*, (04-11).
- Bennett, G. K., Seashore, H. G., and Wesman, A. G. (1947). Differential aptitude test. New York, Psychological Corporation
- Bernard, R. E., and Cooperdock, E. H. (2018). No progress on diversity in 40 years. *Nature Geoscience*, 11(5), 292-295.
- Bidwell, A. (2015). STEM workforce no more diverse than 14 years ago. *US News and World Report*.

- Burke, R. J., and Mattis, M. C. (Eds.). (2007). *Women and minorities in science, technology, engineering, and mathematics: Upping the numbers*. Edward Elgar Publishing.
- Campbell, L. A., and Kaufman, R. L. (2006). Racial differences in household wealth: Beyond black and white. *Research in Social Stratification and Mobility*, 24(2), 131-152.
- Casey, B. J., Getz, S., and Galvan, A. (2008). The adolescent brain. *Developmental review*, 28(1), 62-77.
- Casselman, M. D., Atit, K., Henbest, G., Guregyan, C., Mortezaei, K., and Eichler, J. F. (2019). Dissecting the Flipped Classroom: Using a Randomized Controlled Trial Experiment to Determine When Student Learning Occurs. *Journal of Chemical Education*, 97(1), 27-35.
- Catsambis, S., and Beveridge, A. A. (2001). Does neighborhood matter? Family, neighborhood, and school influences on eighth-grade mathematics achievement. *Sociological Focus*, 34(4), 435-457.
- Census Bureau. (2009). *Statistical abstract of the United States*. Government Printing Office.
- Chan, M. (2013). Why does diversity matter to GSA. *GSA Today*, 23(7), 11.
- Cherney, I. D., Bersted, K., and Smetter, J. (2014). Training spatial skills in men and women. *Perceptual and Motor Skills*, 119(1), 82-99.
- Constantinescu, M., Moore, D. S., Johnson, S. P., and Hines, M. (2018). Early contributions to infants' mental rotation abilities. *Developmental science*, 21(4), e12613.
- Ehrlich, S. B., Levine, S. C., and Goldin-Meadow, S. (2006). The importance of gesture in children's spatial reasoning. *Developmental psychology*, 42(6), 1259.
- Erginer, Ş. D. (2017). The predictive power of fifth graders' learning styles on their mathematical reasoning and spatial ability. *Cogent Education*.
- Faul, F., Erdfelder, E., Lang, A.-G., and Buchner, A. (2007). G*Power 3: A flexible statistical power analysis program for the social, behavioral, and biomedical sciences. *Behavior Research Methods*, 39, 175-191.
- Feig, A. D. (2010). An online introductory physical geology laboratory: From concept to outcome. *Geosphere*, 6(6), 942-951. <https://doi.org/10.1130/ges00511.1>

- Felder, R. M., and Spurlin, J. (2005). Applications, reliability and validity of the index of learning styles. *International journal of engineering education*, 21(1), 103-112.
- Fiscal Year 2017: First Look (Provisional Data). NCES 2019-021Rev. *National Center for Education Statistics*.
- Gagnier, K. M., and Shipley, T. F. (2016). Visual completion from 2D cross-sections: Implications for visual theory and STEM education and practice. *Cognitive Research: Principles and Implications*, 1(1), 9.
- Gardner, H. (2010). *Frames of mind: The theory of multiple intelligences*. New York, NY: Basic Books, A Member of the Perseus Books Group.
- Ginder, S. A., Kelly-Reid, J. E., and Mann, F. B. (2019). Enrollment and Employees in Postsecondary Institutions, Fall 2017; and Financial Statistics and Academic Libraries,
- Google Earth,. Retrieved from: [https://earth.google.com/.](https://earth.google.com/)
- Greenman, E., Bodovski, K., and Reed, K. (2011). Neighborhood characteristics, parental practices and children's math achievement in elementary school. *Social science research*, 40(5), 1434-1444.
- Guay, R. B. (1977). Purdue spatial visualization test-visualization of rotations. *W. Lafayette, IN. Purdue Research Foundation*.
- Guay, R. B., and McDaniel, E. D. (1977). The relationship between mathematics achievement and spatial abilities among elementary school children. *Journal for Research in Mathematics Education*, 211-215.
- Guay, R. B., and McDaniels, E. D. (1976). *The visualization of viewpoints*. West Lafayette, IN: The Purdue Research Foundation.
- Gutierrez, J. C., Chigerwe, M., Ilkiw, J. E., Youngblood, P., Holladay, S. D., and Srivastava, S. (2017). Spatial and Visual Reasoning: Do These Abilities Improve in First-Year Veterinary Medical Students Exposed to an Integrated Curriculum?. *Journal of veterinary medical education*, 44(4), 669-675.
- Güven, B., & Kosa, T. (2008). The effect of dynamic geometry software on student mathematics teachers' spatial visualization skills. *Turkish Online Journal of Educational Technology-TOJET*, 7(4), 100-107.
- Güven, B., and Kosa, T. (2008). The effect of dynamic geometry software on student mathematics teachers' spatial visualization skills. *Turkish Online Journal of Educational Technology-TOJET*, 7(4), 100-107.

- Hango, D. W. (2013). *Gender differences in science, technology, engineering, mathematics and computer science (STEM) programs at university*. Statistics Canada= Statistique Canada.
- Harding, D. J. (2003). Counterfactual models of neighborhood effects: The effect of neighborhood poverty on dropping out and teenage pregnancy. *American journal of Sociology*, 109(3), 676-719.
- Harris, J., Newcombe, N. S., and Hirsh-Pasek, K. (2013). A new twist on studying the development of dynamic spatial transformations: Mental paper folding in young children. *Mind, Brain, and Education*, 7(1), 49-55.
- Hawes, Z., Moss, J., Caswell, B., and Poliszczuk, D. (2015). Effects of mental rotation training on children's spatial and mathematics performance: A randomized controlled study. *Trends in Neuroscience and Education*, 4(3), 60-68.
- Heckman, J. J. (1990). Selection bias and self-selection. In *Econometrics* (pp. 201-224). Palgrave Macmillan, London.
- Hegarty, M., & Waller, D. (2004). A dissociation between mental rotation and perspective-taking spatial abilities. *Intelligence*, 32(2), 175-191.
- Hegarty, M., Canham, M. S., and Fabrikant, S. I. (2010). Thinking about the weather: How display salience and knowledge affect performance in a graphic inference task. *Journal of Experimental Psychology: Learning, Memory, and Cognition*, 36(1), 37-53.
- Hegarty, M., Carpenter, P. A., and Just, M. A. (1991). 23 DIAGRAMS IN THE COMPREHENSION OF SCIENTIFIC TEXTS. *synthesis*, 3, 293-336.
- Höffler, T. N., & Leutner, D. (2007). Instructional animation versus static pictures: A meta-analysis. *Learning and instruction*, 17(6), 722-738.
- Höffler, T. N., and Leutner, D. (2007). Instructional animation versus static pictures: A meta-analysis. *Learning and instruction*, 17(6), 722-738.
- Holmes, M. A., and O'Connell, S. (2003). Where are the women geoscientist professors?. *Eos, Transactions American Geophysical Union*, 84(50), 564-564.
- Holmes, M. A., O'Connell, S., Frey, C., and Ongley, L. (2008). Gender imbalance in US geoscience academia. *Nature Geoscience*, 1(2), 79-82.
- Hoskin, R. (2012). The dangers of self-report. *Science Brainwaves*.

- Huk, T. (2006). Who benefits from learning with 3D models? The case of spatial ability. *Journal of Computer Assisted Learning*, 22(6), 392–404. <https://doi.org/10.1111/j.1365-2729.2006.00180.x>
- Huntoon, J. E., Tanenbaum, C., and Hodges, J. (2015). Increasing diversity in the geosciences. *Eos*, 96(5), 13-15.
- IRIS Earthquake Browser, 2010. Retrieved from: www.iris.edu/ieb/.
- Jirout, J. J., and Newcombe, N. S. (2015). Building blocks for developing spatial skills: Evidence from a large, representative US sample. *Psychological science*, 26(3), 302-310.
- Kali, Y., and Orion, N. (1996). Spatial abilities of high-school students in the perception of geologic structures. *Journal of Research in Science Teaching: The Official Journal of the National Association for Research in Science Teaching*, 33(4), 369-391.
- Kali, Y., Orion, N., and Mazor, E. (1997). Software for assisting high-school students in the spatial perception of geological structures. *Journal of Geoscience Education*, 45(1), 10-21.
- Kastens, K. A., and Ishikawa, T. (2006). Spatial thinking in the geosciences and cognitive sciences: A cross-disciplinary look at the intersection of the two fields. *Special Paper 413: Earth and Mind: How Geologists Think and Learn about the Earth*, 53–76. [https://doi.org/10.1130/2006.2413\(05\)](https://doi.org/10.1130/2006.2413(05))
- Kastens, K. A., Shipley, T. F., Boone, A. P., and Straccia, F. (2016). What Geoscience Experts and Novices Look At, and What They See, When Viewing Data Visualizations. *Journal of Astronomy and Earth Sciences Education*, 3(1), 27-58.
- Keating, D. P., and Stanley, J. C. (1972). Extreme measures for the exceptionally gifted in mathematics and science. *Educational Researcher*, 1(9), 3-7.
- Keehner, M., Montello, D. R., Hegarty, M., and Cohen, C. (2004). Effects of interactivity and spatial ability on the comprehension of spatial relations in a 3D computer visualization. In *Proceedings of the Annual Meeting of the Cognitive Science Society* (Vol. 26, No. 26).
- Klippel, A., Zhao, J., Oprean, D., Wallgrün, J. O., and Chang, J. S. K. (2019, March). Research framework for immersive virtual field trips. In *2019 IEEE Conference on Virtual Reality and 3D User Interfaces (VR)* (pp. 1612-1617). IEEE.
- Koch, D. S. (2006). The effects of solid modeling and visualization on technical problem solving. Blacksburg: Virginia Polytechnic Institute and State University.

- Kolb, B., and Wishaw, I. Q. (2014). *An introduction to brain and behavior* (4th ed.). New York, NY: Worth publishers.
- Landivar, L. C. (2013). Disparities in STEM employment by sex, race, and Hispanic origin. *Education Review*, 29(6), 911-922.
- Lauer, J. E., and Lourenco, S. F. (2016). Spatial processing in infancy predicts both spatial and mathematical aptitude in childhood. *Psychological Science*, 27(10), 1291-1298.
- Lauer, J. E., Yhang, E., and Lourenco, S. F. (2019). The development of gender differences in spatial reasoning: A meta-analytic review. *Psychological bulletin*, 145(6), 537.
- Levine, S. C., Ratliff, K. R., Huttenlocher, J., and Cannon, J. (2012). Early puzzle play: a predictor of preschoolers' spatial transformation skill. *Developmental psychology*, 48(2), 530.
- Levine, S. C., Vasilyeva, M., Lourenco, S. F., Newcombe, N. S., and Huttenlocher, J. (2005). Socioeconomic status modifies the sex difference in spatial skill. *Psychological science*, 16(11), 841-845.
- Liben, L. S., and Titus, S. J. (2012). The importance of spatial thinking for geoscience education: Insights from the crossroads of geoscience and cognitive science. *Geological Society of America Special Papers*, 486, 51-70.
- Linn, M. C., and Petersen, A. C. (1985). Emergence and characterization of sex differences in spatial ability: A meta-analysis. *Child development*, 1479-1498.
- Linn, M.C. (2003). Technology and science education: starting points, research programs, and trends. *International journal of science education*, 25(6), 727-758.
- Lohman, D. F. (1994). Spatial ability. In R. J. Sternberg (Ed.), *Encyclopedia of intelligence* (Vol. 2, pp. 1000–1007). New York: Macmillan.
- Lowrie, T., Logan, T., and Hegarty, M. (2019). The influence of spatial visualization training on students' spatial reasoning and mathematics performance. *Journal of Cognition and Development*, 20(5), 729-751.
- Maccoby, E. E., and Jacklin, C. N. (1974). Myth, reality and shades of gray-what we know and dont know about sex differences. *Psychology Today*, 8(7), 109-112.
- Mayer, R. E., and Sims, V. K. (1994). For whom is a picture worth a thousand words? Extensions of a dual-coding theory of multimedia learning. *Journal of educational psychology*, 86(3), 389.

- Mayer, R. E., Bove, W., Bryman, A., Mars, R., and Tapangco, L. (1996). When less is more: Meaningful learning from visual and verbal summaries of science textbook lessons. *Journal of educational psychology*, 88(1), 64.
- McGee, M. G. (1979). Human spatial abilities: Psychometric studies and environmental, genetic, hormonal, and neurological influences. *Psychological bulletin*, 86(5), 889.
- Miller, D. I., and Halpern, D. F. (2013). Can spatial training improve long-term outcomes for gifted STEM undergraduates?. *Learning and individual differences*, 26, 141-152.
- Miller, D. I., and Halpern, D. F. (2014). The new science of cognitive sex differences. *Trends in cognitive sciences*, 18(1), 37-45.
- Miller, J. D., and Kimmel, L. G. (2012). Pathways to a STEMM profession. *Peabody Journal of Education*, 87(1), 26-45.
- National Research Council of the National Academies (NRC). 2013. Preparing the next generation of earth scientists: An examination of federal education and training programs. Report prepared by the Committee on Trends and Opportunities in Federal Earth Science Education and Workforce Development. Washington, DC: National Academies Press, p. 98.
- National Science Board, (2014). Science and Engineering Indicators for 2014. *Arlington VA*.
- National Science Foundation (NSF). 2013. National Science Foundation integrated science and engineering resources data system (WebCASPAR): Raw data from the National Center for Education Statistics (NCES), including IPEDS completion surveys
- Neuburger, S., Ruthsatz, V., Jansen, P., and Quaiser-Pohl, C. (2015). Can girls think spatially? Influence of implicit gender stereotype activation and rotational axis on fourth graders' mental-rotation performance. *Learning and Individual Differences*, 37, 169-175.
- Newcombe, N., Bandura, M. M., and Taylor, D. G. (1983). Sex differences in spatial ability and spatial activities. *Sex roles*, 9(3), 377-386.
- Ormand, C. J., Manduca, C., Shipley, T. F., Tikoff, B., Harwood, C. L., Atit, K., & Boone, A. P. (2014). Evaluating geoscience students' spatial thinking skills in a multi-institutional classroom study. *Journal of Geoscience Education*, 62(1), 146-154.

- Ormand, C. J., Shipley, T. F., Tikoff, B., Dutrow, B., Goodwin, L. B., Hickson, T., Atit, K., Gagnier, K., and Resnick, I. (2017). The Spatial Thinking Workbook: A Research-Validated Spatial Skills Curriculum for Geology Majors. *Journal of Geoscience Education*, 65(4), 423–434. <https://doi.org/http://dx.doi.org/10.5408/16-210.1>
- Piburn, M. D., Reynolds, S. J., Leedy, D. E., McAuliffe, C. M., Birk, J. P., and Johnson, J. K. (2002, April). The hidden earth: Visualization of geologic features and their subsurface geometry. In *annual meeting of the National Association for Research in Science Teaching, New Orleans, LA* (pp. 1-4).
- Piburn, M. D., Reynolds, S. J., McAuliffe, C., Leedy, D. E., Birk, J. P., and Johnson, J. K. (2005). The role of visualization in learning from computer-based images. *International Journal of Science Education*, 27(5), 513-527.
- Pruden, S. M., Levine, S. C., and Huttenlocher, J. (2011). Children's spatial thinking: Does talk about the spatial world matter?. *Developmental science*, 14(6), 1417-1430.
- Rapp, D. N. (2005). Mental models: Theoretical issues for visualizations in science education. In *Visualization in science education* (pp. 43-60). Springer, Dordrecht.
- Rapp, D. N., Culpepper, S. A., Kirkby, K., and Morin, P. (2007). Fostering students' comprehension of topographic maps. *Journal of Geoscience Education*, 55(1), 5-16.
- Reardon, S. F., and Bischoff, K. (2011). Income inequality and income segregation. *American Journal of Sociology*, 116(4), 1092-1153.
- Ritchie, H., and Roser, M. (2019). Gender Ratio. *Our World in Data*.
- Šafhalter, A., Vukman, K. B., and Glodež, S. (2016). The effect of 3D-modeling training on students' spatial reasoning relative to gender and grade. *Journal of Educational Computing Research*, 54(3), 395-406. <https://doi.org/10.1177/0735633115620430>
- Sastry, N., and Pebley, A. R. (2010). Family and neighborhood sources of socioeconomic inequality in children's achievement. *Demography*, 47(3), 777-800.
- Serbin, L. A., and Connor, J. M. (1979). Sex-typing of children's play preferences and patterns of cognitive performance. *The Journal of Genetic Psychology*, 134(2), 315-316.

- Sharkey, P., and Elwert, F. (2011). The legacy of disadvantage: Multigenerational neighborhood effects on cognitive ability. *American journal of sociology*, 116(6), 1934-81.
- Shiple, T. F., and Tikoff, B. (2016). Linking cognitive science and disciplinary geoscience practice: The importance of the conceptual model.
- Sorby, S. A. (2006). Developing 3D spatial skills for K-12 students. *Engineering design graphics journal*, 70(3), 1-11.
- Sorby, S. A. (2007). Developing 3D spatial skills for engineering students. *Australasian Journal of Engineering Education*, 13(1), 1-11.
- Sorby, S. A. (2009). Educational research in developing 3-D spatial skills for engineering students. *International Journal of Science Education*, 31(3), 459-480.
- Statistics Canada. (2011). National household survey. *Statistics Canada*.
- Stokes, P. J., Levine, R., and Flessa, K. W. (2015). Choosing the geoscience major: Important factors, race/ethnicity, and gender. *Journal of Geoscience Education*, 63(3), 250-263.
- Stumpf, H. (1993). Performance factors and gender-related differences in spatial ability: Another assessment. *Memory & cognition*, 21(6), 828-836.
- Subrahmanyam, K., and Greenfield, P. M. (1994). Effect of video game practice on spatial skills in girls and boys. *Journal of applied developmental psychology*, 15(1), 13-32.
- Super, D. E., and Bachrach, P. B. (1957). Scientific careers and vocational development theory: A review, a critique and some recommendations.
- Titus, S., and Horsman, E. (2009). Characterizing and improving spatial visualization skills. *Journal of Geoscience Education*, 57(4), 242-254.
- Titze, C., Heil, M., and Jansen, P. (2008). Gender differences in the mental rotations test (MRT) are not due to task complexity. *Journal of Individual Differences*, 29(3), 130-133.
- Tversky, B. (2000). Some ways that maps and diagrams communicate. In *Spatial Cognition II* (pp. 72-79). Springer, Berlin, Heidelberg.
- Uttal, D. H., and Cohen, C. A. (2012). Spatial thinking and STEM education: When, why, and how?. In *Psychology of learning and motivation* (Vol. 57, pp. 147-181). Academic Press.

- Uttal, D. H., Meadow, N. G., Tipton, E., Hand, L. L., Alden, A. R., Warren, C., and Newcombe, N. S. (2013). The malleability of spatial skills: A meta-analysis of training studies. *Psychological bulletin*, 139(2), 352.
- Visible Geology Beta,. Retrieved from: <http://app.visiblegeology.com/profile.html>
- Voyer, D. (2011). Time limits and gender differences on paper-and-pencil tests of mental rotation: a meta-analysis. *Psychonomic bulletin and review*, 18(2), 267-277.
- Voyer, D., Voyer, S., and Bryden, M. P. (1995). Magnitude of sex differences in spatial abilities: a meta-analysis and consideration of critical variables. *Psychological bulletin*, 117(2), 250.
- Wai, J., Lubinski, D., and Benbow, C. P. (2009). Spatial ability for STEM domains: Aligning over 50 years of cumulative psychological knowledge solidifies its importance. *Journal of educational Psychology*, 101(4), 817.
- West, R. M. (2021). Best practice in statistics: Use the Welch t-test when testing the difference between two groups. *Annals of Clinical Biochemistry*, 58(4), 267-269.
- Wise, L. L., McLaughlin, D. H., and Steel, L. (1979). The Project TALENT data handbook, revised. *Palo Alto, CA: American Institutes for Research*.
- Woods, T. L., Reed, S., Hsi, S., Woods, J. A., and Woods, M. R. (2016). Pilot Study Using the Augmented Reality Sandbox to Teach Topographic Maps and Surficial Processes in Introductory Geology Labs. *Journal of Geoscience Education*, 64(3), 199–214. <https://doi.org/10.5408/15-135.1>
- Xie, Y., Fang, M., and Shauman, K. (2015). STEM education. *Annual review of sociology*, 41, 331-357.
- Yang, E. M., Andre, T., Greenbowe, T. J., and Tibell, L. (2003). Spatial ability and the impact of visualization/animation on learning electrochemistry. *International Journal of Science Education*, 25(3), 329-349.
- Zancada-Menendez, C., Sampedro-Piquero, P., Lopez, L., & McNamara, T. P. (2016). Age and gender differences in spatial perspective taking. *Aging clinical and experimental research*, 28(2), 289-296.
- Zoom Video Conferencing Web, 2014. Retrieved from <https://www.zoom.us/-->

CONCLUSION

The findings from Chapter 1 highlight that while the earth is evolving, its past may be recorded in the seismic structure of the continents. In Chapter 1, we see traces of past structure in the form of a 15 km step in lithospheric thickness. This step is interpreted to be a relic structure associated with the formation of Pangea. We also find that the lithosphere is thinner than expected, suggesting the possibility that thermal erosion has occurred due to one or more dynamic processes. These findings suggest that inherited structure may be preserved in the present-day lithosphere despite recent dynamic processes thought to be associated with the Northern Appalachian Anomaly. In Chapter 2, we present for the first time the differential attenuation structure of the entire East Africa Rift. In our study, we use these differential attenuation estimates to model absolute attenuation (Q_P), thermal variations, and velocity anomalies in three regions of our study. We find that a modeled low Q_P layer, similar to values observed at mid-ocean ridges, is sufficient to reconcile previous estimates of temperature and observed velocity anomalies. Finally, our main conclusion from Chapter 3 is that a gender gap exists in spatial learning. By studying beginner-level geoscience education, we can improve teaching pedagogy and help innovate the field of geology.

APPENDIX A: Chapter 1 Data Repository

Evidence for a lithospheric step and pervasive lithospheric thinning beneath southern New England by G. Goldhagen et al. 2022

Sp receiver function analysis and common conversion point stacking methodology

Waveform data were downloaded from the IRIS Data Management Center (DMC). All data to be used in the study are open access, including SEISConn data. Sp waveforms were limited to events at epicentral distances of 55°-85°, magnitudes of 5.8 or greater and depths of less than 300 km. Waveform preprocessing included rotation into the radial and transverse components and bandpass filtering. Predicted S-wave arrival times were estimated by using the 1D velocity model, AK315 (Kennett et al., 1995), and the TauP ray tracing program (Crotwell et al., 1999). The predicted arrival times were compared to estimated arrival times based on signal to noise analysis (S2N). Our S2N analysis follows the methodology described in detail in Abt et al. (2010) (Section 3.1 Phase Picking). Briefly, we use the short-term-average to long-term-average moving window method of Earle and Shearer (1994), using a signal window length of 10 seconds and a noise window length of 40 seconds. The S2N ratio of the envelope function was then generated for a range of ± 25 seconds around the TauP predicted phase arrival. If the TauP predicted- and S2N estimated arrival times were greater than 5 seconds apart, the waveform was discarded all other data were used and no other metrics were used for culling. The number of events requested versus the number of events used in the final

analysis varied from network and network and station to station. For example, 210 waveforms were downloaded from the IRIS DMC for station L64A (N4), of which 74 were culled. 145 waveforms were downloaded for station CS08 (XP; SEISConn) and 65 were culled. 251 were downloaded for station LSCT (US), and 99 were culled. A full list of downloaded events and culled events are available per station in Table A.1. Waveforms were then rotated into the P-SV-SH reference frame using a best-fitting free-surface transform (Bostock, 1998). The parameters for the free-surface transform were determined through an automated procedure detailed in Abt et al. (2010). This involves the parent phase (SV) being windowed around its arrival time, and a search performed over a range of V_p and V_p/V_s to find the values that minimized the correlation of the parent phase with a corresponding window on the daughter component (P). For each station all cross-correlation surfaces with well-defined minima were stacked and the best free surface velocities for the individual station were defined as the minimum of this stack.

After waveform preprocessing, receiver functions were calculated using an extended time multitaper (ETMT) deconvolution technique (Helffrich, 2006) and bandpass filtered between 2-100 s. An additional filter of 2-33 s was initially tried but resulted in results with less coherence. Our preferred filter is similar to the one applied in Hopper and Fischer (2018) and tested in Mancinelli et al. (2017), both of which used the same receiver function code. The polarity of the S_p receiver functions was reversed to match the typical P_s convention. Receiver function time series were migrated to depth using the

crustal velocity model Crust1.0 (Laske et al., 2013) and the regional 3D seismic tomography model for mantle velocities (Schmandt & Lin 2014, Schmandt et al., 2015). We utilize the model of Schmandt and Lin (2014) for P-wave velocities at all mantle depths, and S-wave velocities below 120 km, and Schmandt et al. (2015) for S-wave velocities above 120 km. To incorporate 3D structure while avoiding numerically intensive ray tracing, a 1D model was generated for each point in latitude/longitude space, averaging the 3D model at each depth according to the size of the predicted Fresnel zone, similar to what has been done in previous Sp receiver function studies. This 1-D average is then applied to each station-event pair for a given station (Lekic et al., 2011; Ford et al., 2014; Hopper and Fischer, 2015; Hopper et al, 2017; Hopper and Fischer, 2018). Uncertainties associated with utilizing an incorrect migration model in our analysis are discussed in the supplementary materials of Lekic et al (2011). Using synthetics, Lekic et al (2011) argue that uncertainties do not exceed 5 km and are likely less than that.

The migrated Sp receiver functions were stacked in a 3D model discretized at 0.1° increments in latitude and longitude, and 0.5 km in depth. A weighted average of individual receiver functions was calculated, with weights given by cubic spline functions that approximate the Sp phase Fresnel zone (Lekic et al., 2011). In order to place constraints on the uncertainties in depth and amplitude, the finalized CCP migrated receiver functions were calculated using an iterative bootstrapping technique (Hopper and Fischer, 2018).

Negative phase interpretation

Side lobes are a demonstrated artifact of Sp receiver function analysis, and more specifically receiver functions calculated using the extended time multitaper technique used here (Lekic and Fischer, 2017). To minimize the appearance of side-lobes, we perform windowing in the time domain before deconvolution to exclude post-S arrivals and filter to sufficiently high frequencies (0.5 Hz), two techniques that have been documented to reduce the appearance of side lobes (Lekic and Fischer, 2017). Qualitatively, we observe that our interpreted phase does not consistently track with the positive phase energy at shallower depths (Moho), which would be indicative of a side lobe phase. For example, in cross section D-D' from a longitude of $\sim 75^{\circ}\text{W}$ to $\sim 73.2^{\circ}\text{W}$ the positive phase (i.e., Moho) shallows considerably while the negative phase remains flat. Conversely, in cross section B-B' the positive phase remains flat across the study region. A side lobe would track with the Moho phase, in contrast to what we see.

Demonstrating a difference in negative phase depth and amplitude across the terrane boundary

In order to facilitate an understanding of how robust the change in depth and amplitude of the selected negative phase is across the Taconic belt/Ganderia terrane boundary, we examined both the distribution of data using histograms and through the use of kmeans clustering analysis. Initial histograms plots were made with the raw depth and amplitude values in our study area, for regions west and east of the terrane boundary (Figures A.3 &

A.4). While a robust calculation of the mean and standard deviation is not possible given the multimodal distribution of depths, which appear to correlate with real changes in structure, we do calculate average values for both populations and find average values of depth west of the boundary to be 80 km, east of the boundary 66 km, and amplitudes west of the boundary to be 0.11 and east of the boundary 0.08. To better understand the relationship between amplitude, depth and terrane boundary we again divided our results into two groups according to whether they are west or east of the terrane boundary (Figure A.3), and then compared these results to data divided using kmeans clustering analysis, in which the only variables are depth and amplitude. In our comparison we find that 81% of the points divided into the terrane groupings agree with the groups determined by kmeans analysis, assuming that only two clusters are used. The remaining 19% of the points disagree, and primarily fall in a region of overlap at ~60 to ~75 km (Figure A.5).

Is the negative phase a mid-lithospheric discontinuity or the lithosphere-asthenosphere boundary?

The negative phases selected in our study are thought to represent a negative velocity gradient associated with the transition from high seismic velocity lithosphere to low seismic velocity asthenosphere. Using a framework developed previously (Abt et al., 2010; Ford et al., 2010; Birkey et al., 2021), we define the lithosphere as being the depth range in which a positive velocity gradient (increasing velocity with increasing depth) is present, starting beneath the crust and extending until a local maximum is reached. The

potential lithosphere-asthenosphere boundary depth range begins at this peak in absolute velocity and ends when a minimum in absolute velocity (thought to be indicative of the asthenosphere) is reached. The absolute velocities used in this study come from the ambient noise tomography model of Yang and Gao (2018).

To best illustrate the correspondence between our negative phase picks and the tomography model, we averaged the velocity model according to latitude into two groups (Figure 1.4 of chapter 1). The averaged models were then used to determine our potential LAB depth range (magenta lines). We plotted our negative phase picks within each averaged region, shading them according to their location in latitude. For the 42.1-43°N averaged region, where the lithospheric step is less pronounced according to receiver functions, the LAB phases fall almost entirely within or below the potential LAB depth range. For the 41.2-42°N averaged region, where the lithospheric step is more abrupt, the LAB phases typically fall within or below the potential LAB depth range. However, a few potential LAB phases in the local maximum (solid magenta line) step down at ~72°W, while our receiver functions imply that a flatter LAB is present.

Data Repository Figures and Tables

Table 1.1. Events with Data per Station and Events Culled

Stations	Events with Data*	Events Culled [†]
<i>LD</i>		
BRNJ	1106	484
BRNY	861	361
CONY	151	61
CPNY	1118	504
CUNY	320	138
FOR	1120	479
HCNY	768	330
KSCT	484	213
MSNJ	550	257
NPNY	758	202
ODNJ	799	368
PAL	1534	691
PANJ	424	76
TRNY	219	83
UCCT	211	94
<i>N4</i>		
K62A	215	83
L64A	210	74
M63A	236	70
N62A	231	84
<i>NE</i>		
BCX	475	210

BRYW	735	321
QUA2	690	299
TRY	782	360
WES	811	341
WSPT	411	174
YLE	729	307
<u>TA</u>		
K95A	118	50
K60A	118	45
K61A	140	51
K62A	143	50
K63A	129	44
L60A	118	39
L61A	115	44
L61B	345	127
L62A	117	42
L63A	134	50
L64A	142	43
L65A	137	43
M60A	119	41
M61A	137	51
M62A	115	43
M63A	116	49
M64A	132	46
M65A	459	187

M66A	138	45
N61A	113	42
N62A	106	47
N63A	116	44
O61A	131	56
<u>US</u>		
LSCT	251	99
<u>XA</u>		
MM01	68	52
MM02	98	73
MM03	100	76
<u>XO</u>		
KICK	5	2
SCCC	94	32
UCON	8	7
UHRT	7	6
VASR	94	35
WICK	103	38
WIND	94	38
<u>XP</u>		
CS01	88	47
CS02	75	24
CS03	209	92
CS04	73	31
CS05	199	81
CS06	140	61

CS07	145	59
CS08	145	65
CS09	62	34
CS10	41	16
CS11	0	0
CS12	109	49
CS11	126	59
CS12	218	85
CS15	96	46

Note:

*Events with Data includes only the events which contained all three components with full data and do not include any multiples which were discarded.

†Culled data includes all the Events with Data that were subsequently culled due to low signal-to-noise ratios.

Table A.1 Full table of station names, events with data per each station, and events culled due to low signal-to-noise ratios.

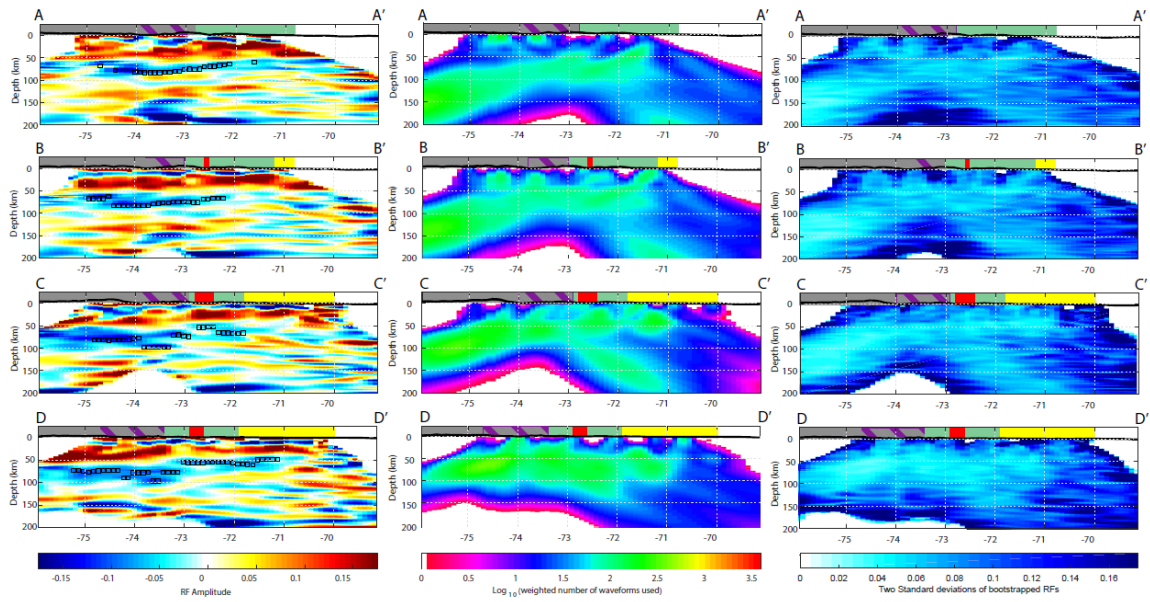


Figure A.1 (a) Original cross-sections shown in Figure 1.2 of chapter 1; alongside (b) the sampling density, which is determined by the number of weighted events using the Sp Fresnel zone approximation discussed in the data repository; and (c) two standard deviation of the bootstrapped receiver functions. Note the dearth of data at 150-200km from 75-72.5°W. Terrane boundaries are shown at the top of (b) profiles and correspond in color to the terranes in Figures 1.1 and 1.2 of chapter 1.

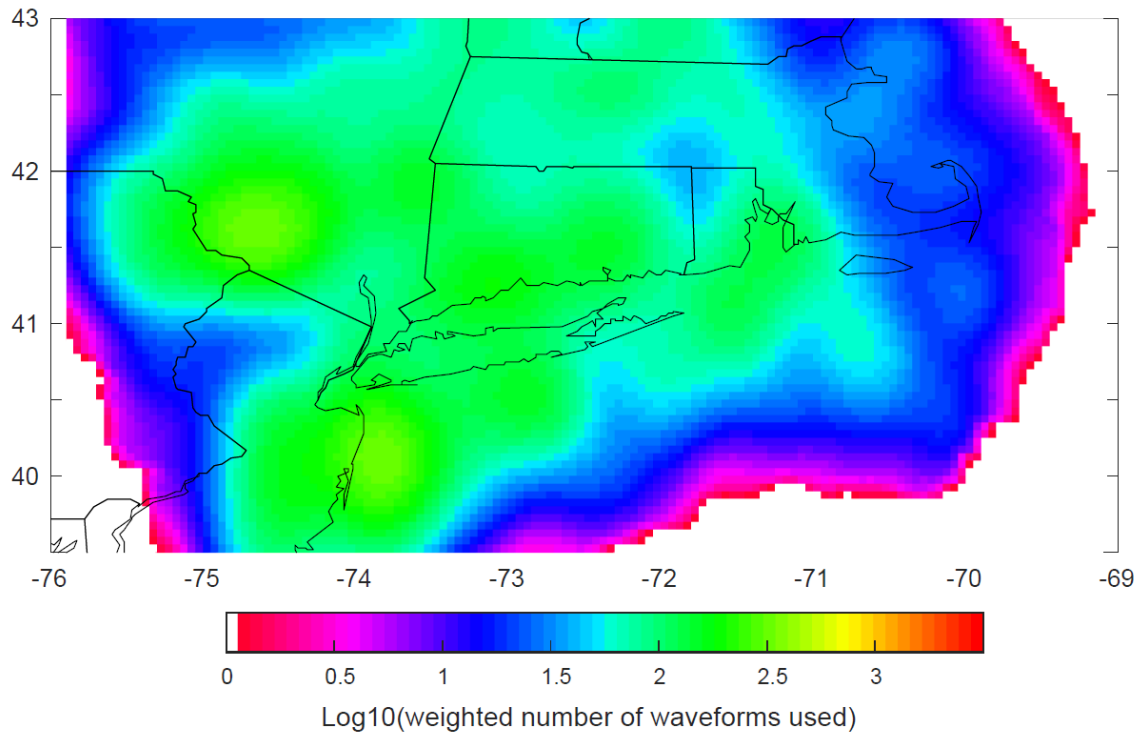


Figure A.2 Map view of sampling density, shown for a depth slice at 70km, which is determined by the number of weighted events using the Sp Fresnel zone approximation discussed in the data repository.

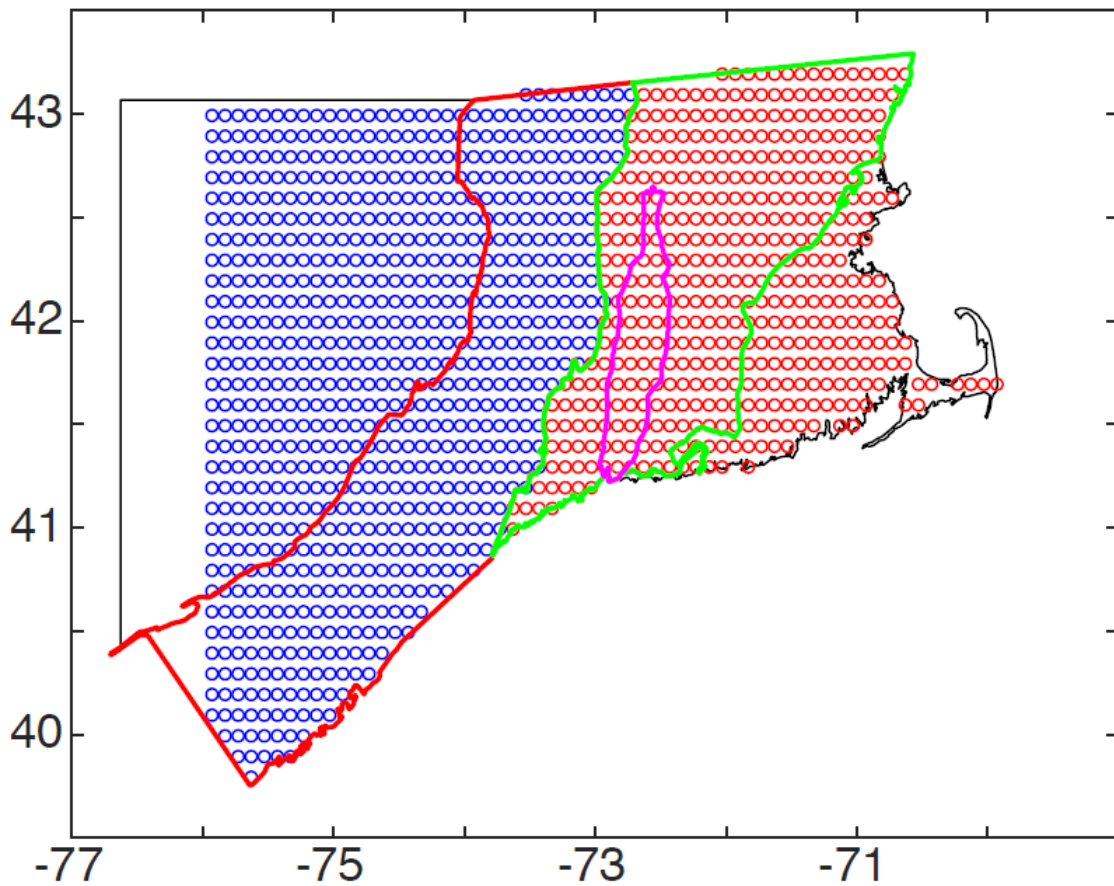


Figure A.3 Map illustrating how individual points within the receiver function model were subdivided in order to determine average depth and amplitude of the negative phase east and west of the Taconic-Ganderia Boundary, generate histograms (Figure A.4) and in the clustering comparison (Figure A.5)

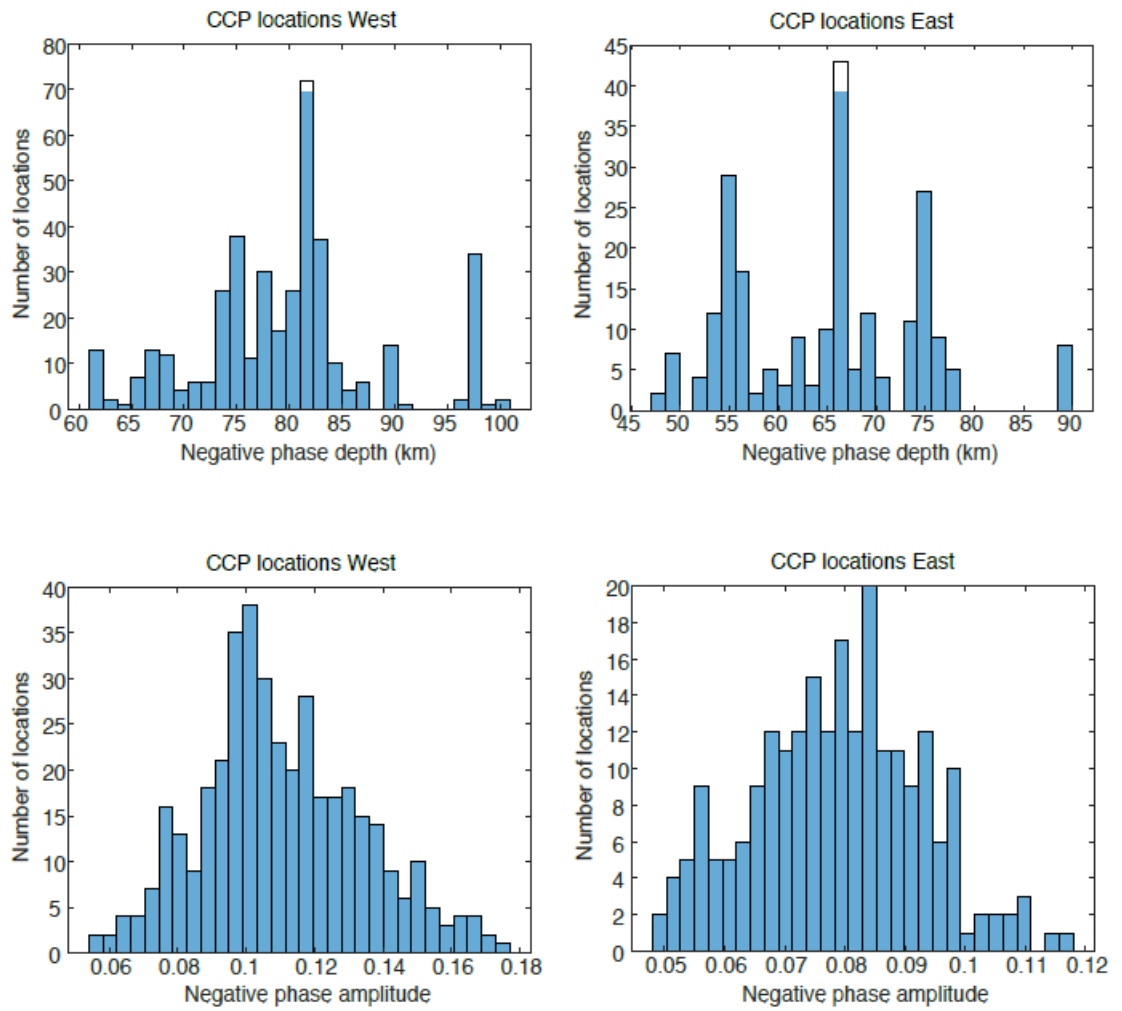


Figure A.4 Histograms of negative phase depth (top row) and amplitude (bottom row) for negative phases located west (left column) and east (right column) of the Taconic-Ganderia boundary.

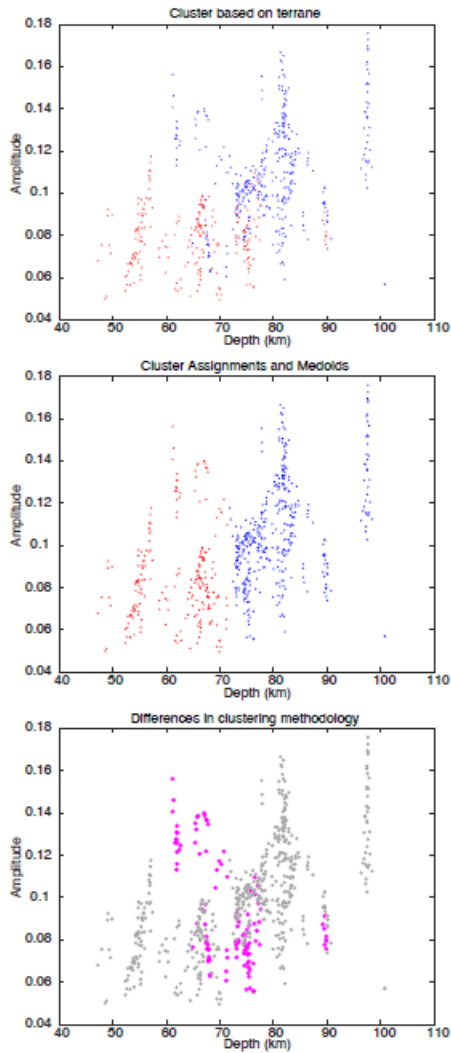



Figure A.5 (top) Negative phase picks grouped by terrane and plotted as a function of amplitude vs depth. Red points correspond to negative phases located east of the terrane boundary (Figure A.3) and blue points correspond to negative phases located to the west of the terrane boundary (Figure A.3). (middle) Negative phase picks clustered according to kmeans analysis, assuming that only two clusters are used. No prior knowledge of point locations are known during kmeans analysis and colors are randomly assigned and do not correspond to colors shown in the top panel. (bottom) Comparison of the kmeans clustering methodology relative to grouping based on location relative to the terrane boundary. Grey points mark points that agree between the two methods while pink points mark the 19% of points that disagree.

REFERENCES

- Abt, D. L., Fischer, K. M., French, S. W., Ford, H. A., Yuan, H., & Romanowicz, B. (2010). North American lithospheric discontinuity structure imaged by Ps and Sp receiver functions. *Journal of Geophysical Research: Solid Earth*, 115(B9).
- Birkey, A., Ford, H. A., Dabney, P., & Goldhagen, G. (2021). The lithospheric architecture of Australia from seismic receiver functions. *Journal of Geophysical Research: Solid Earth*, 126(4), e2020JB020999.
- Bostock, M. G. (1998). Mantle stratigraphy and evolution of the Slave province. *Journal of Geophysical Research: Solid Earth*, 103(B9), 21183-21200.
- Crotwell, H. P., Owens, T. J., & Ritsema, J. (1999). The TauP Toolkit: Flexible seismic travel-time and ray-path utilities. *Seismological Research Letters*, 70, 154-160.
- Ford, H. A., Fischer, K. M., Abt, D. L., Rychert, C. A., & Elkins-Tanton, L. T. (2010). The lithosphere–asthenosphere boundary and cratonic lithospheric layering beneath Australia from Sp wave imaging. *Earth and Planetary Science Letters*, 300(3-4), 299-310.
- Ford, H.A., Fischer, K.M., and Lekic, V., 2014, Localized shear in the deep lithosphere beneath the san andreas fault system: *Geology*, v. 42, p. 295–298, doi:10.1130/G35128.1.
- Helfrich, G. (2006). Extended-time multitaper frequency domain cross-correlation receiver-function estimation. *Bulletin of the Seismological Society of America*, 96(1), 344-347.
- Hopper, E., & Fischer, K. M. (2015). The meaning of midlithospheric discontinuities: A case study in the northern US craton. *Geochemistry, Geophysics, Geosystems*, 16(12), 4057-4083.
- Hopper, E., & Fischer, K. M. (2018). The changing face of the lithosphere-asthenosphere boundary: Imaging continental scale patterns in upper mantle structure across the contiguous US with Sp converted waves. *Geochemistry, Geophysics, Geosystems*, 19(8), 2593-2614.
- Hopper, E., Fischer, K.M., Wagner, L.S., and Hawman, R.B., (2017). Reconstructing the end of the Appalachian orogeny: *Geology*, v. 45, p. 15–18, doi:10.1130/G38453.1.
- Kennett, B. L. N., & Engdahl, E. R. (1991). Traveltimes for global earthquake location and phase identification. *Geophysical Journal International*, 105(2), 429-465.

- Laske, G., Masters, G., Ma, Z., & Pasyanos, M. (2013, April). Update on CRUST1. 0—A 1-degree global model of Earth's crust. In *Geophys. res. abstr* (Vol. 15, p. 2658)
- Chen, Y., Randerson, J. T., Morton, D. C., DeFries, R. S., Collatz, G. J., Kasibhatla, P. S., ... & Marlier, M. E. (2011). Forecasting fire season severity in South America using sea surface temperature anomalies. *Science*, *334*(6057), 787-791.
- Mancinelli, N. J., Fischer, K. M., & Dalton, C. A. (2017). How sharp is the cratonic lithosphere-asthenosphere transition?. *Geophysical Research Letters*, *44*(20), 10-189.
- Schmandt, B., & Lin, F. C. (2014). P and S wave tomography of the mantle beneath the United States. *Geophysical Research Letters*, *41*(18), 6342-6349.
- Schmandt, B., Lin, F. C., & Karlstrom, K. E. (2015). Distinct crustal isostasy trends east and west of the Rocky Mountain Front. *Geophysical Research Letters*, *42*(23), 10-290.
- Yang, X., & Gao, H. (2018). Full-wave seismic tomography in the northeastern United States: New insights into the uplift mechanism of the Adirondack Mountains. *Geophysical Research Letters*, *45*(12), 5992-6000.

APPENDIX B: Chapter 3 Student Demographic Survey

Student Demographic Survey	Student ID # _____
	
<p>What is your Major? _____</p> <p>What is your age? _____</p> <p>What is the highest educational level earned by your parents?</p> <p><input type="checkbox"/> Less than a High School Diploma</p> <p><input type="checkbox"/> High School Diploma</p> <p><input type="checkbox"/> Associates Degree</p> <p><input type="checkbox"/> Bachelor's Degree</p> <p><input type="checkbox"/> Graduate Degree or Higher</p> <p>Are you a first generation college student?</p> <p><input type="checkbox"/> Yes <input type="checkbox"/> No</p> <p>What are your parent or guardian's occupations?</p> <p>_____</p> <p>_____</p> <p>_____</p> <p>What year of school are you currently in?</p> <p><input type="checkbox"/> Freshman <input type="checkbox"/> Sophomore</p> <p><input type="checkbox"/> Junior <input type="checkbox"/> Senior</p> <p><input type="checkbox"/> Fifth Year Senior</p> <p><input type="checkbox"/> Other _____</p> <p>Please List any previous science courses you completed in either high school or college:</p> <p>_____</p> <p>_____</p> <p>_____</p> <p>_____</p> <p>What is your current GPA? _____/4.0</p>	
<p>What race or ethnicity do you identify as? _____</p> <p>[Please Check the Corresponding Box]</p> <p><input type="checkbox"/> White or Caucasian or Euro-American <input type="checkbox"/> Puerto Rican</p> <p><input type="checkbox"/> African American or Black or African <input type="checkbox"/> East Asian or Asian American</p> <p><input type="checkbox"/> American Indian or Alaska Native <input type="checkbox"/> Middle Eastern or Arab American</p> <p><input type="checkbox"/> Native Hawaiian or Pacific Islander <input type="checkbox"/> Other</p> <p><input type="checkbox"/> Mexican American or Chicano</p>	
<p>What gender do you identify as? _____</p> <p>[Please Check the Corresponding Box]</p> <p><input type="checkbox"/> Male <input type="checkbox"/> Transgender [Male to Female]</p> <p><input type="checkbox"/> Female <input type="checkbox"/> Transgender [Female to Male]</p> <p><input type="checkbox"/> Non-Binary <input type="checkbox"/> Other _____</p>	